TU Delft

Delft University of Technology

Tuning Magnetoelastic Transitions in Mn2Sb-based and Fe2Hf-based Magnetocaloric Materials

Shen, Q.

DOI
10.4233/uuid:3f379e63-9a3e-4755-974d-4d2099db43ea

Publication date
2023

Document Version
Final published version

Citation (APA)
Shen, Q. (2023). *Tuning Magnetoelastic Transitions in Mn2Sb-based and Fe2Hf-based Magnetocaloric Materials*. [Dissertation (TU Delft), Delft University of Technology]. https://doi.org/10.4233/uuid:3f379e63-9a3e-4755-974d-4d2099db43ea

Important note
To cite this publication, please use the final published version (if applicable).
Please check the document version above.

Copyright
Other than for strictly personal use, it is not permitted to download, forward or distribute the text or part of it, without the consent of the author(s) and/or copyright holder(s), unless the work is under an open content license such as Creative Commons.

Takedown policy
Please contact us and provide details if you believe this document breaches copyrights.
We will remove access to the work immediately and investigate your claim.

This work is downloaded from Delft University of Technology.
For technical reasons the number of authors shown on this cover page is limited to a maximum of 10.

Tuning Magnetoelastic Transitions in Mn_2Sb-based and Fe_2Hf-based Magnetocaloric Materials

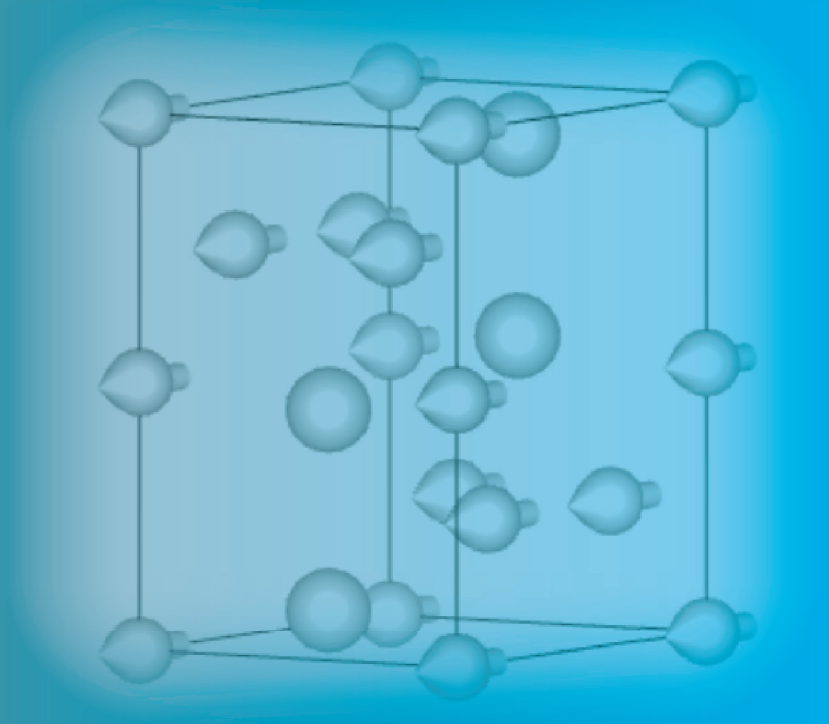

Qi SHEN

沈 琪

Tuning Magnetoelastic Transitions in Mn_2Sb-based and Fe_2Hf-based Magnetocaloric Materials

Dissertation

for the purpose of obtaining the degree of doctor

at Delft University of Technology

by the authority of the Rector Magnificus, Prof.dr.ir. T.H.J.J. van der Hagen,

chair of the Board for Doctorates

to be defended publicly on

Thursday 21 September 2023 at 10:00 o'clock

by

Qi SHEN

Master of Materials Physics and Chemistry

Chinese Academy of Sciences, China

Born in Jiangxi, China

This dissertation has been approved by the promotors.

Composition of the doctoral committee:

Rector Magnificus,	chairperson
Prof. dr. E.H. Brück	Delft University of Technology, promotor
Dr.ir. N.H. van Dijk	Delft University of Technology, promotor

……

Independent members:

Prof. dr. K. Hooman	Delft University of Technology
Prof. dr. J. Liu	Shanghai University, China
Dr. A. de Visser	University of Amsterdam
Prof. dr. H. Swagten	Eindhoven University of Technology
Prof. dr. O. Isnard	Université Grenoble Alps, France
Prof. dr.ir. J. L. Kloosterman	Delft University of Technology, reserve member

The work described in this thesis was carried out in the group of Fundamental Aspects of Materials and Energy (FAME), Faculty of Applied Sciences, Delft University of Technology. This work is part of the project funded by Dutch Research Council (NWO) and co-financed by Swiss Blue Energy and RSP Technology.

Keywords: Magnetocalroic effect, magnetoelastic transition, Laves phase, magnetic refrigeration.

ISBN 978-94-6366-728-9

Copyright © 2023 by Qi SHEN

Printed by Proefschrift specialist

An electronic version of this dissertation is available at https://repository.tudelft.nl/

Dedicated to my parents, my brother and Jian Yang

献给我的父母，弟弟和杨剑

Contents

Chapter 1 Introduction 1

1.1 History of magnetic refrigeration and potential applications of magnetocaloric materials 2

1.2 Development of magnetocaloric materials 4

1.3 Characterization of magnetocaloric materials 5

1.4 Typical magnetocaloric materials with an order-order magnetoelastic transition 6

1.4.1 Mn_2Sb-based intermetallic compounds 6

1.4.2 Fe_2Hf-based Laves phase compounds 7

1.5 Outline of this thesis 9

References 10

Chapter 2 Experimental techniques 17

2.1 Sample preparation techniques 18

2.1.1 Arc-melting 18

2.1.2 Melt-spinning 19

2.2 Crystal structure 20

2.2.1 X-ray Diffraction 20

2.2.2 Neutron Diffraction 20

2.2 Microstructure 21

2.2.1 Scanning Electron Microscopy 21

2.2.2 Electron Probe Micro Analysis 21

2.3 Calorimetry measurements 21

2.4 Magnetic measurements 22

2.5 Mössbauer spectroscopy 22

2.6 Thermodynamic calculations of the magnetocaloric effect 23

References 25

Chapter 3 Nonlinear influence of excess Mn on the magnetoelastic transition in $(Mn,Cr)_2Sb$ 27

Abstract 28

3.1 Introduction 29

3.2 Experimental methods 30

3.3 Results and discussion 31

3.4 Conclusions 39

References 40

Supplementary Material for Chapter 3 43

Chapter 4 The antiferromagnetic to ferrimagnetic phase transition in $Mn_2Sb_{1-x}Bi_x$ compounds 45

Abstract 46

4.1 Introduction 47

4.2 Experimental methods 48

4.3 Results and discussion 50

4.4 Conclusions 58

References 59

Supplementary Material for Chapter 4 62

Chapter 5 Magnetoelastic transition and negative thermal expansion of $Fe_2Hf_{0.83}Ta_{0.17}$ ribbons 65

Abstract 66

5.1 Introduction 67

5.2 Experimental methods 68

5.3 Results and discussion 69

5.4 Conclusions 76

References 77

Supplementary Material for Chapter 5 81

Chapter 6 Exploring the negative thermal expansion and magnetocaloric effect in Fe_2(Hf,Ti) Laves phase materials 85

Abstract 86

6.1 Introduction 87

6.2 Experimental methods 88

6.3 Results and discussion 90

6.4 Conclusions 105

References 106

Supplementary Material for Chapter 6 113

Summary 119

Samenvatting 122

总结 126

Acknowledgements 129

List of publications 137

Curriculum Vitae 141

Chapter 1 Introduction

'Scientific knowledge is a body of statements of varying degrees of certainty — some most unsure, some nearly sure, none absolutely certain.'

Richard Feynman

To deal with the challenge of natural resource energy shortage and global climate warming, magnetic refrigeration, one of the most promising solid-state refrigeration techniques, attracts much attention due to the theoretically higher efficiency, environmentally friendliness and quietness compared to vapor compression refrigeration. In this chapter, at first a brief introduction about the history of the magnetocaloric effect is given and the basic principles of three potential applications of magnetocaloric materials including the magnetic refrigeration, magnetic heat pump, and thermomagnetic generator are explained. Then the development of popular magnetocaloric materials and characterization parameters of the magnetocaloric effect are introduced. Afterwards, the two typical magnetocaloric materials studied in this thesis are introduced. Finally, an outline of this thesis is given at the end of this chapter.

1.1 History of magnetic refrigeration and potential applications of magnetocaloric materials

The rapid development of human civilization leads to an enormous consumption of natural energy sources and detrimental impacts on the environment. According to a research study, "The world has not been investing enough in energy in recent years, a fact that left the energy system much more vulnerable to the sort of shocks seen in 2022. A smooth and secure energy transition will require a major uptick in clean energy investment flows. Getting on track for the near zero energy scenario will require a tripling in spending on clean energy and infrastructure to 2030, alongside a shift towards much higher investment in emerging market and developing economies." [1]. Refrigeration accounts for 15% of the global energy consumption and is expected to increase this share in the future [2]. It was demonstrated that a refrigerator using a magnetic material such as Gd metal can achieve an efficiency up to 60% of the theoretical limit, compared to only 40% for devices based on vapor compression [3]. In addition to the advantage of a higher potential cooling efficiency, magnetic refrigerators are quieter due to the absence of a compressor and less harmful to the environment since the devices are water-based and do not contain ozone-depleting or greenhouse gasses. Magnetic refrigeration is based on the magnetocaloric effect (MCE), which is the caloric response of MCE materials, characterized by an adiabatic temperature change or an isothermal entropy change when a magnetic field is applied or removed. The MCE dates back to 1917 when Weiss and Piccard reported a reversible temperature change of 0.7 K in nickel in response to a magnetic field change of 1.5 T around its Curie temperature of 627 K [4]. The concept of magnetic cooling at low temperatures by adiabatic demagnetization of paramagnetic salts was first proposed independently by Debye [5] and Giauque [6], respectively. The first experimental demonstration of magnetic cooling was reported by Giauque and MacDougall [7] in 1933. In 1949, Giauque was awarded the Nobel Prize in Chemistry for his great achievement in the field of magnetic refrigeration.

The standard magnetic refrigeration cycle is shown in Fig. 1.1. Initially, the magnetic moments are randomly distributed. When a magnetic field is applied adiabatically, the magnetic entropy decreases and thus the lattice vibration entropy increases. As a result, the temperature of the MCE material increases. The heat can be removed using an environmentally friendly medium such as water, and the temperature of the material returns to ambient temperature. When the magnetic field is removed, the magnetic moments randomize again and the temperature of the material decreases. To close the cycle heat can be absorbed by the magnetic material via water from e.g. foodstuff that needs to be refrigerated [8]. On the other hand, the application of a magnetic heat pump is based on the same cycle, but it utilizes the expelled heat [9].

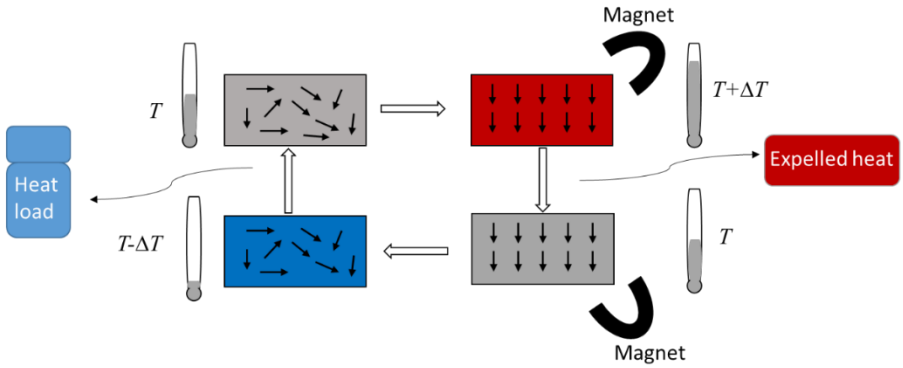

Fig. 1.1. Schematic drawing of the magnetic refrigeration cycle.

In addition to magnetic refrigeration and heat pumping, power generation is also a potential application based on the MCE [10]. A device based on the temperature dependence of the magnetization is called a thermomagnetic generator, the basic mechanism of which is shown in Fig. 1.2. A ferromagnetic shunt is connected to a heat source and a heat sink. When the ferromagnetic shunt is heated, its magnetization decreases and vice versa. The change in magnetization results in a change in magnetic flux. This induces a voltage in the coil and by repeating this process an AC current can be generated. MCE materials for a thermomagnetic

generator require a large and fast magnetization change with temperature, a small thermal hysteresis and a limited latent heat.

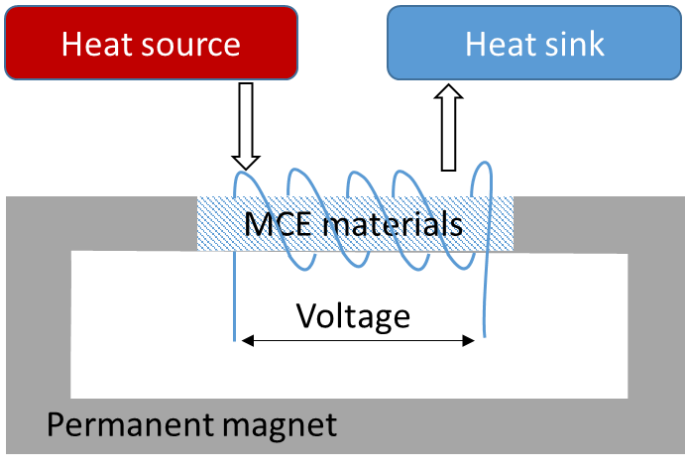

Fig. 1.2. Schematic diagram of a thermomagnetic generator.

1.2 Development of magnetocaloric materials

In the past, the main interest in MCE materials focused on materials that contained rare-earth elements, considering their large magnetic moments, and showed a second-order phase transition. However, the MCE of these materials is generally low at room temperature. A good MCE candidate is pure Gd, which shows a second-order phase transition with a $|\Delta S_m|$ of 3.2 (6.1) J/kgK at T_C = 294 K for a magnetic field change of 1 (2) T [11]. In 1976, Brown first demonstrated the feasibility of room-temperature magnetic refrigeration using the MCE material Gd [12]. Interest in room-temperature MCE refrigeration has increased greatly since 1997 when a large $|\Delta S_m|$ of 18.5 J/kgK ($\Delta\mu_0 H$ = 5 T) was obtained near T_C = 270 K in $Gd_5Si_2Ge_2$ compounds with a first-order phase transition. The last 25 years testify to an exponential growth of MCE research [13]. First-order and second-order phase transitions are distinguished by the presence or absence of latent heat, respectively. In contrast to the gradual change in magnetization versus temperature in MCE materials with a second-order phase transition, MCE materials with a first-order phase transition exhibit a sharp transition and a giant magnetocaloric effect due to the

strong coupling of lattice and spin degrees of freedom. Depending on the change in crystal symmetry, MCE materials with a first-order phase transition can be further classified into two categories: a magnetostructural transition (crystal symmetry changes), as observed in Mn(As,Sb) [14], MnCoGe [15], Ni_2Mn-based [16, 17]; a magnetoelastic transition (the crystal symmetry remains the same), as observed in FeRh [18], $La(Fe,Si)_{13}$ [19, 20], $(Mn,Fe)_2(P,Si)$ [21, 22], Mn_2Sb-based [23], and $Fe_2(Hf,Ta)$ [24]. The values of $|\Delta S_m|$ and $|\Delta T_{ad}|$ for some typical giant MCE materials can be seen in Fig. 1.3 [25].

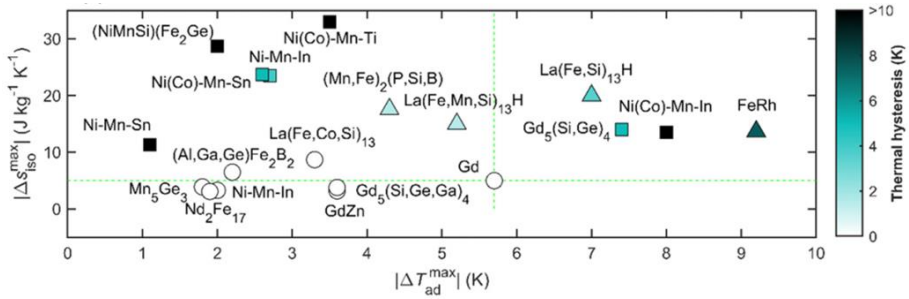

Fig. 1.3. $|\Delta S_m|$ and $|\Delta T_{ad}|$ at the magnetic field change of 2 T for representative magnetocaloric materials at room temperature [25].

1.3 Characterization of magnetocaloric materials

MCE materials with the same ΔS_m, but with a different thermal hysteresis, may have a different cyclic behavior. Therefore, the reversible adiabatic temperature change is considered to evaluate the efficiency of magnetic refrigeration. The coefficient of MCE refrigeration is proposed by Brück and co-workers [26]:

$$CRP\ (B_{\max}) = \frac{\text{refrigerant capacity}}{\text{positive work on refrigerant}} = \frac{\Delta S \Delta T_{rev}}{\int_0^{B max} M(T_C,B)dB} \qquad (1)$$

To achieve a high *CRP*, ideal MCE materials require a large magnetic entropy change, a large adiabatic temperature change, a tunable transition temperature and a small thermal hysteresis. Compared to MCE materials with a magnetostructural transition, most MCE materials with a magnetoelastic transition have the advantage of a low thermal hysteresis. To further optimize MCE materials for practical

applications, insights into the magnetoelastic coupling are important, which can be gained by comparing and analyzing the phase transition in different magnetoelastic MCE materials. In this thesis, two magnetoelastic MCE systems are chosen with phase transitions that show an opposite influence of the applied magnetic field on the phase transition temperature: the Mn_2Sb-based system with an antiferromagnetic-to-ferrimagnetic transition and the Fe_2Hf-based system with a ferromagnetic-to-antiferromagnetic transition. Both material systems have in common that the magnetic moments originate from abundant 3*d* metals.

1.4 Typical magnetocaloric materials with an order-order magnetoelastic transition

1.4.1 Mn_2Sb-based intermetallic compounds

Mn_2Sb has a Cu_2Sb-type tetragonal structure (space group P4/*nmm*) with a Curie temperature of 550 K [27]. The schematic unit-cell structure is shown in Fig. 1.4(a). The Mn atoms have two different crystallographic positions: Mn-I (2*a* site) and Mn-II (2*c* site). Neutron diffraction showed that the Mn-I and Mn-II atoms possess magnetic moments of 2.1 and −3.9 μ_B, respectively [27]. At temperatures below 550 K, Mn-I and Mn-II are antiparallel to each other, resulting in a ferrimagnetic (FIM) structure. Upon cooling, the moments of Mn-I and Mn-II both reorient from being antiparallel to the *c* axis in the tetragonal lattice into the *a*-*b* basal plane at the spin reorientation temperature (T_{SR}) of about 240 K [28]. $(Mn,X)_2Sb$ (*X* = V [29], Cr [23], Co [28], Cu [30], Zn [31]) and $Mn_2(Sb,Y)$ (*Y* = Sn [32], As [33], Bi [34], Ge [35]) exhibit a first-order magnetoelastic transition from the FIM to the AFM transition with decreasing temperature due to exchange inversion, which is caused by the shrinkage of the lattice or the change in the coefficient of thermal expansion by element substitution [36]. Taking $Mn_{1.8}Co_{0.2}Sb$ as an example, the magnetic structures at different temperatures derived from neutron diffraction [28] are shown in Fig. 1.4(b-d). At the magnetoelastic transition temperature lattice parameter *c* decreases, which is compensated by an increase in lattice parameter *a*, resulting in a small increase of 0.02–0.1% in the unit-cell volume [23]. A table-like giant inverse

MCE of $\Delta S_m \approx 5$ J/kg K ($\Delta\mu_0 H = 2$ T) in the temperature range of 200–350 K is reported in $(Mn,Cr)_2Sb$ alloys with different Cr substitutions [23]. A value of $\Delta T \approx 2$ K ($\Delta\mu_0 H = 5$ T) around room temperature for a nearly hysteresis-free transition [37] in $Mn_{2-x}Cr_xSb_{0.95}Ga_{0.05}$ suggests the good potential for MCE applications of Mn_2Sb-based intermetallic compounds.

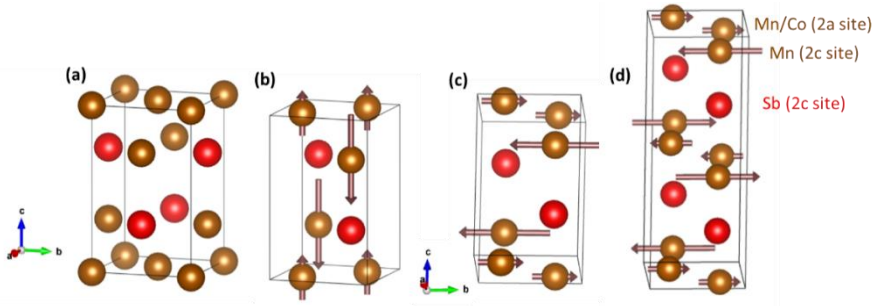

Fig. 1.4. (a) Unit-cell structure of the Mn_2Sb crystal. Magnetic structures of $Mn_{1.8}Co_{0.2}Sb$: (b) ferrimagnetic structure below the spin reorientation temperature, (c) ferrimagnetic structure above the spin reorientation temperature, (d) antiferromagnetic structure.

1.4.2 Fe_2Hf-based Laves phase compounds

Laves phases (AB_2) are topologically close-packed, intermetallic compounds, named after the German mineralogist and crystallographer Fritz Laves (1906–1978). Most Laves phases crystallize in one of the following three structures: cubic $MgCu_2$, hexagonal $MgZn_2$ and hexagonal $MgNi_2$. They have a wide range of applications in hydrogen storage, superconductivity and magnetostriction [38]. MCE liquefaction of hydrogen has been extensively studied in Laves phase compounds with A = rare earths such as ACo_2 and AAl_2 (A = Er, Ho, Dy) [39, 40]. The MCE near room temperature has been reported in the Fe-based Laves phases without rare earths. One example is the $Hf_{1-x}Ta_xFe_2$ system that crystallizes in the hexagonal Mg_2Zn-type structure with space group $P6_3/mmc$, as shown in Fig. 1.5(a). The Fe atoms occupy the 2*a* and 6*h* sites and the Hf/Ta atoms the 4*f* site. In contrast to the Mn_2Sb-based alloys, the $Hf_{1-x}Ta_xFe_2$ compounds undergo a FM-to-AFM transition with increasing

temperature and further transform into the PM phase at the Néel temperature (T_N). The value of T_N ranges from 334–338 K and is not sensitive to the Ta content. A detailed phase diagram can be found in [41]. It is found that x = 0.13 is the critical composition for the convergence of the FM, AFM and PM phases. In the FM state the Fe magnetic moments at the 2*a* and 6*h* sites are within the *a*-*b* plane. In the AFM state, the Fe magnetic moments at the 2*a* site are frustrated because they lie in the middle of the two antiferromagnetic planes [42]. The magnetic structures of $Hf_{1-x}Ta_xFe_2$ are derived from neutron diffraction [42] and are shown in Fig. 1.5(c, d). With the FM-AFM transition, the lattice parameter *a* decreases, while the lattice parameter *c* remains constant, leading to a 1% shrinkage of the unit-cell volume [43]. This also makes the Fe_2(Hf,Ta) compounds promising candidates as negative thermal expansion (NTE) materials [41]. The magnetic entropy change for a field change of $\Delta\mu_0 H$ = 1 T varies from 5 to 18 J/kgK for the Fe_2(Hf,Ta) system with various Ta substitution contents [44]. A large adiabatic temperature change of 3.5 K ($\Delta\mu_0 H$ = 2 T) is reported for $Fe_2Hf_{0.84}Ta_{0.16}$ [24]. This first-order FM-AFM phase transition is also reported in other Fe-based Laves phase compounds, such as the Fe_2(Hf,Nb) [45, 46] and Fe_2(Sc,Ti) systems [47-49].

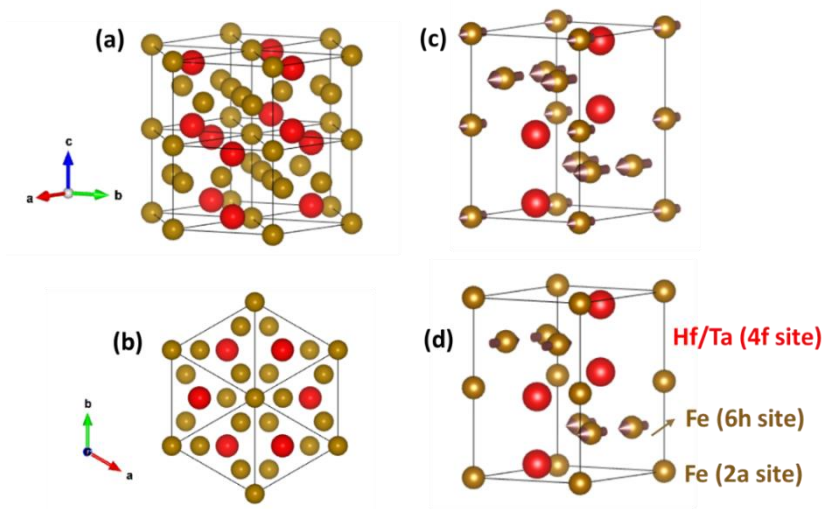

Fig. 1.5. (a-b) Unit-cell structure of the Fe_2Hf crystal structure. Magnetic structure of Fe_2(Hf,Ta): (c) ferromagnetic structure and (d) antiferromagnetic structure.

1.5 Outline of this thesis

The aim of this thesis is to provide new insights into the coupling between the spin and the lattice degrees of freedom and to reveal the relation between the microstructure and the macroscopic magnetic performance in different magnetoelastic MCE materials. In this thesis the fundamental physical properties including the crystal structure, the microstructure, the magnetic structure, the negative thermal expansion behaviour and the magnetocaloric effect are studied in Mn_2Sb-based intermetallic compounds with an antiferromagnetic-ferrimagnetic transition and Fe_2Hf-based Laves phase compounds with a ferromagnetic-antiferromangetic transition. Thus in the former system when traversing from low to high temperature we observe a sudden increase in magnetization and in the latter a sudden decrease in magnetization.

In Chapter 2, the sample preparation techniques, experimental methods and thermodynamic calculations of magnetocaloric materials are presented.

In Chapter 3, the influence of excess Mn on the ferromagnetic-to-antiferromagnetic transition and the influence on the formation of the MnSb secondary phase is studied in the magnetocaloric compound $(Mn,Cr)_2Sb$. A compositional diagram of the *c/a* ratio was constructed to assist in the selection of $(Mn,Cr)_2Sb$ alloys with a desired transition temperature.

In Chapter 4, the influence of partial substitution of Bi for Sb on the microstructure, magnetic properties and magnetocaloric effect is studied for $Mn_2Sb_{1-x}Bi_x$ (x = 0, 0.02, 0.04, 0.05, 0.07, 0.09, 0.15, 0.20) compounds. The origin of the antiferro-to-ferrimagnetic transition in $Mn_2Sb_{1-x}Bi_x$ is also discussed.

In Chapter 5, the magnetocaloric effect and negative thermal expansion are discussed for arc-melted and melt-spun $Fe_2Hf_{0.83}Ta_{0.17}$ Laves phase compounds. The origin of second-order phase transition of the melt-spun alloy is attributed to the partially suppressed frustration effect, which is due to the atomic disorder introduced by the rapid solidification.

In Chapter 6, the negative thermal expansion and magnetocaloric effect are investigated in arc-melted and melt-spun $Fe_2Hf_{1-x}Ti_x$ (x = 0.15, 0.27, 0.30, 0.33, 0.36, 0.40) alloys. It is found that melt spinning can supress the phase segregation in high-Ti content compounds and improve the magnetocaloric effect. The correlation between the magnetocaloric effect and the negative thermal expansion is analysed by neutron powder diffraction and Mössbauer spectroscopy.

A summary, acknowledgments, a list of publications and a short curriculum vitae can be found at the end of this thesis.

References

[1] World Energy Outlook 2022. https://www.iea.org/reports/world-energy-outlook-2022/key-findings (accessed May 2023).

[2] 2nd International Conference on Magnetic Refrigeration at Room Temperature, Slovenia (2007).

[3] C. Zimm, Description and performance of a near-room temperature magnetic refrigerator, 43 (1998) 1759-1766.

[4] P. Weiss, A. Piccard, Le phénomène magnétocalorique, Journal de Physique Théorique et Appliquée 7 (1917) 103-109.

[5] P. Debye, Einige Bemerkungen zur Magnetisierung bei tiefer Temperatur, Annalen der Physik 386 (1926) 1154-1160.

[6] W.F. Giauque, A thermodynamic treatment of centain magentic effects. a proposed method of producing temperature considerably below 1◦ absolute, Am. Chem. Soc. 49 (1927) 1864.

[7] W.F. Giauque, D. P. MacDougall, Attainment of Temperatures Below 1° Absolute by Demagnetization of $Gd_2(SO_4)_3 \cdot 8H_2O$, Phys. Rev. 43 (1933) 768-768.

[8] E. Brück, Developments in magnetocaloric refrigeration, J. Phys. D: Appl. Phys. 38 (2005) R381-R391.

[9] H. Johra, K. Filonenko, P. Heiselberg, C. Veje, S. Dall'Olio, K. Engelbrecht, C. Bahl, Integration of a magnetocaloric heat pump in an energy flexible residential building, Renew. Energy 136 (2019) 115-126.

[10] R.A. Kishore, S. Priya, A review on design and performance of thermomagnetic devices, Renew. Sustain. Energy Rev. 81 (2018) 33-44.

[11] J. Lyubina, Magnetocaloric materials for energy efficient cooling, J. Phys. D: Appl. Phys. 50 (2017) 053002 .

[12] G.V. Brown, Magnetic heat pumping near room temperature, J. Appl. Phys. 47 (1976) 3673-3680.

[13] F. Zhang, Tuning Giant Magnetocaloric Materials: A Study of $(Mn,Fe)_2(P,Si)$ and NiCoMnTi Heusler Compounds, TU Delft thesis (2022).

[14] H. Wada, Y. Tanabe, Giant magnetocaloric effect of $MnAs_{1-x}Sb_x$, Appl. Phys. Lett. 79 (2001) 3302-3304.

[15] N.T. Trung, L. Zhang, L. Caron, K.H.J. Buschow, E. Brück, Giant magnetocaloric effects by tailoring the phase transitions, Appl. Phys. Lett. 96 (2010) 172504.

[16] T. Krenke, E. Duman, M. Acet, E.F. Wassermann, X. Moya, L. Manosa, A. Planes, Inverse magnetocaloric effect in ferromagnetic Ni-Mn-Sn alloys, Nat. Mater. 4 (2005) 450-4.

[17] J. Liu, T. Gottschall, K.P. Skokov, J.D. Moore, O. Gutfleisch, Giant magnetocaloric effect driven by structural transitions, Nat. Mater. 11 (2012) 620-6.

[18] A. Chirkova, K.P. Skokov, L. Schultz, N.V. Baranov, O. Gutfleisch, T.G. Woodcock, Giant adiabatic temperature change in FeRh alloys evidenced by direct measurements under cyclic conditions, Acta Mater. 106 (2016) 15-21.

[19] A. Fujita, S. Fujieda, Y. Hasegawa, K. Fukamichi, Itinerant-electron metamagnetic transition and large magnetocaloric effects in $La(Fe_xSi_{1-x})_{13}$ compounds and their hydrides, Phys. Rev. B 67 (2003) 104416.

[20] L. Miao, X. Lu, Z. Wei, Y. Zhang, Y. Zhang, J. Liu, Enhanced mechanical strength in hot-rolled La-Fe-Si/Fe magnetocaloric composites by microstructure manipulation, Acta Mater. 245 (2023).

[21] O. Tegus, E. Bruck, K. H. J. Buschow, F. R. de Boer, Transition-metal-based magnetic refrigerants for room-temperature applications, Nature 415 (2002) 150-151.

[22] N.H. Dung, Z.Q. Ou, L. Caron, L. Zhang, D.T.C. Thanh, G.A. de Wijs, R.A. de Groot, K.H.J. Buschow, E. Brück, Mixed magnetism for refrigeration and energy conversion, Adv. Energy Mater. 1 (2011) 1215-1219.

[23] L. Caron, X.F. Miao, J.C.P. Klaasse, S. Gama, E. Brück, Tuning the giant inverse magnetocaloric effect in $Mn_{2-x}Cr_xSb$ compounds, Appl. Phys. Lett. 103 (2013) 112404.

[24] Z. Song, Z. Li, B. Yang, H. Yan, C. Esling, X. Zhao, L. Zuo, Large Low-Field Reversible Magnetocaloric Effect in Itinerant-Electron $Hf_{1-x}Ta_xFe_2$ Alloys, Materials 14 (2021) 1-11.

[25] L.M. Moreno-Ramírez, J.Y. Law, Á. Díaz-García, V. Franco, Advanced Magnetocaloric Materials, in: A.S.M.A. Haseeb (Ed.), Encyclopedia of Materials: Electronics (2023) 616-632.

[26] E. Brück, H. Yibole, L. Zhang, A universal metric for ferroic energy materials, Philos. Trans. R. Soc. A 374 (2016) 20150303.

[27] M.K. Wilkinson, N.S. Gingrich, C.G. Shull, The magnetic structure of Mn_2Sb, J. Phys. Chem. Solids 2 (1957) 289-300.

[28] J. Wilden, A. Hoser, M. Chikovani, J. Perßon, J. Voigt, K. Friese, A. Grzechnik, Magnetic Transitions in the Co-Modified Mn_2Sb System, Inorganics 6 (2018) 113.

[29] W. Cui, W.J. Ren, Z.D. Zhang, X. Zhou, H. Zhong, Q. Wang, Lattice distortion tuning of the metamagnetic phase transition in tetragonal Cu_2Sb-type $Mn_{1.95}V_{0.05}Sb$ alloy, Scr. Mater. 143 (2018) 59-62.

[30] X. Zhou, H. Zhong, D. Yu, W. Cui, T. Liu, Q. Wang, Interstitial effects of B addition on the metamagnetic transition and magnetocaloric effect in tetragonal Cu_2Sb-type $Mn_{1.95}Cu_{0.05}Sb$ alloys, Intermetallics 90 (2017) 50-53.

[31] V.I. Val'kov, A.V. Golovchan, I.F. Bribanov, V.I. Kamenev, O.O. Iesenchuk, A.P. Sivachenko, N.N. Kabdin, Stability characteristics of the low temperature ferrimagnetism in the $Mn_{2-x}Zn_xSb$ system, Low Temp. Phys. 33 (2007) 70-78.

[32] Y.q. Zhang, Z.d. Zhang, Metamagnetic-transition-induced giant magnetoresistance in $Mn_2Sb_{1-x}Sn_x$ ($0 < x \leqslant 0.4$) compounds, Phys. Rev. B 67 (2003).

[33] T. Kakimoto, J. Goto, S. Fujii, K. Koyama, S. Ishida, Electronic and Magnetic Properties of $Mn_2Sb_{1-x}As_x$ (x = 0, 0.5, 1), Mater. Trans. 55 (2014) 1878-1884.

[34] Z. Zhang, Y. Zhang, X. Luo, S. Ma, H. Zeng, G. Yu, X. Zheng, C. Chen, Y. Hu, F. Xu, S.U. Rehman, Z. Zhong, Self-organized Bi-rich grain boundary precipitates for realizing steep magnetic-field-driven metamagnetic transition in Bi-doped Mn_2Sb, Acta Mater. 200 (2020) 835-847.

[35] J. Zhang, G. Yao, S. Chen, F. Wei, X. Fan, X. Yin, Z. Chen, W. Cui, Q. Wang, The effects of Ge occupation and hydrostatic pressure on the metamagnetic phase transition and magnetocaloric effect, AIP Advances 9 (2019) 035106.

[36] C. Kittel, Model of Exchange-Inversion Magnetization, Phys. Rev. 120 (1960) 335-342.

[37] A. Tekgül, M. Acet, F. Scheibel, M. Farle, N. Ünal, The reversibility of the inverse magnetocaloric effect in $Mn_{2-x}Cr_xSb_{0.95}Ga_{0.05}$, Acta Mater. 124 (2017) 93-99.

[38] F. Stein, A. Leineweber, Review of their functional and structural applications and an improved fundamental understanding of stability and properties, J. Mater. Sci. 56 (2020) 5321-5427.

[39] V.B. Chzhan, I.S. Tereshina, A.Y. Karpenkov, E.A. Tereshina-Chitrova, Persistent values of magnetocaloric effect in the multicomponent Laves phase compounds with varied composition, Acta Mater. 154 (2018) 303-310.

[40] W. Liu, E. Bykov, S. Taskaev, M. Bogush, V. Khovaylo, N. Fortunato, A. Aubert, H. Zhang, T. Gottschall, J. Wosnitza, F. Scheibel, K. Skokov, O. Gutfleisch, A study on rare-earth Laves phases for magnetocaloric liquefaction of hydrogen, Appl. Mater. Today 29 (2022) 101624.

[41] L.F. Li, P. Tong, Y.M. Zou, W. Tong, W.B. Jiang, Y. Jiang, X.K. Zhang, J.C. Lin, M. Wang, C. Yang, X.B. Zhu, W.H. Song, Y.P. Sun, Good comprehensive performance of Laves phase $Hf_{1-x}Ta_xFe_2$ as negative thermal expansion materials, Acta Mater. 161 (2018) 258-265.

[42] L.V.B. Diop, O. Isnard, E. Suard, D. Benea, Neutron diffraction study of the itinerant-electron metamagnetic $Hf_{0.825}Ta_{0.175}Fe_2$ compound, Solid State Commun. 229 (2016) 16-21.

[43] B. Li, X.H. Luo, H. Wang, W.J. Ren, S. Yano, C.W. Wang, J.S. Gardner, K.D. Liss, P. Miao, S.H. Lee, T. Kamiyama, R.Q. Wu, Y. Kawakita, Z.D. Zhang, Colossal negative thermal expansion induced by magnetic phase competition on frustrated lattices in Laves phase compound $(Hf,Ta)Fe_2$, Phys. Rev. B 93 (2016) 224405.

[44] S. Huang, D. Wang, Z. Han, Z. Su, S. Tang, Y. Du, Magnetic and magnetocaloric properties of quenched $Hf_{1-x}Ta_xFe_2$ materials, J. Alloys Compd. 394 (2005) 80-82.

[45] H. Yibole, A.K. Pathak, Y. Mudryk, F. Guillou, N. Zarkevich, S. Gupta, V. Balema, V.K. Pecharsky, Manipulating the stability of crystallographic and magnetic sub-lattices: A first-order magnetoelastic transformation in transition metal based Laves phase, Acta Mater. 154 (2018) 365-374.

[46] Y. Song, J. Chen, X. Liu, C. Wang, Q. Gao, Q. Li, L. Hu, J. Zhang, S. Zhang, X. Xing, Structure, Magnetism, and Tunable Negative Thermal Expansion in $(Hf,Nb)Fe_2$ Alloys, Chem. Mater. 29 (2017) 7078-7082.

[47] Y. Song, Q. Sun, M. Xu, J. Zhang, Y. Hao, Y. Qiao, S. Zhang, Q. Huang, X. Xing, J. Chen, Negative thermal expansion in $(Sc,Ti)Fe_2$ induced by an unconventional magnetovolume effect, Mater. Horiz. 7 (2020) 275-281.

[48] L. Sun, H. Yibole, O. Tegus, F. Guillou, Magnetocaloric Effect, Magnetoresistance of $Sc_{0.28}Ti_{0.72}Fe_2$, and Phase Diagrams of $Sc_{0.28}Ti_{0.72}Fe_{2-x}T_x$ Alloys with T = Mn or Co, Crystals 10 (2020) 410.

[49] Y. Song, M. Xu, X. Zheng, C. Zhou, N. Shi, Q. Huang, S. Wang, Y. Jiang, X. Xing, J. Chen, A new method to enhance the magnetocaloric effect in (Sc,Ti)Fe_2 via magnetic phase separation, J. Mater. Sci. Technol. 147 (2023) 102-111.

Chapter 2 Experimental techniques

'The exploration and research in science, in its essence, hold intrinsic beauty, and the pleasure it brings is its own reward. Therefore, in my work, I have found happiness.'

Marie Curie

The crystal structure, microstructure, magnetic structure, negative thermal expansion behavior and magnetocaloric effect are studied in two magnetoelastic magnetocaloric materials in this thesis. In this chapter, the sample preparation methods, sample characterization techniques and thermodynamic calculations of magnetocaloric effect are presented.

Arc-melting and melt-spinning techniques are used to synthesize button and ribbon shaped samples for different microstructures. The crystal structure and phase fraction are analyzed by X-ray diffraction. The phase homogeneity and elemental distribution are determined by scanning electron microscopy and electron probe microstructure analysis. The transition temperatures, phase-transition latent heat and adiabatic temperature change are derived from calorimetric measurements. A superconducting quantum interference device and a vibrating sample magnetometer are used to measure the isothermal and isofield magnetization curves, which provide the magnetic transition temperature and magnetic entropy change. Neutron diffraction and Mössbauer spectroscopy are employed to provide the microscopic magnetic properties. At the end of this chapter, the relevant equations for the characterization of the magnetocaloric effect are derived from thermodynamic calculations.

2.1 Sample preparation techniques

2.1.1 Arc-melting

An arc-melting furnace is a low-cost, easy-to-use and compact device for melting metals and alloys. Components with high purity can be rapidly heated to a temperature of about 3300 K where molten reactants can be formed [1]. The arc-melting device used in this thesis is a home-made design consisting of a main chamber, a copper crucible and a tungsten needle torch with a high-vacuum system and a water cooling system. Details on this arc-melting furnace can be found in [2]. A schematic drawing of the setup is shown in Fig. 2.1. The vacuum can be pumped down to 1×10^{-7} mbar and then the chamber is filled with 500 mbar high purity argon (99.999%), which serves as the ionization gas for the arc discharge. The starting materials in the argon atmosphere are melted by the hot plasma generated by the discharge process from a tungsten electrode (cathode) onto the conductive starting materials on a copper crucible (anode). The molten sample in the form of a button is turned over by a wobble stick and is melted 4–5 times to avoid possible inhomogeneity caused by the difference in cooling rate for the upper and lower parts of the sample within the copper crucible. The typical mass for an arc-melted sample is about 5 g.

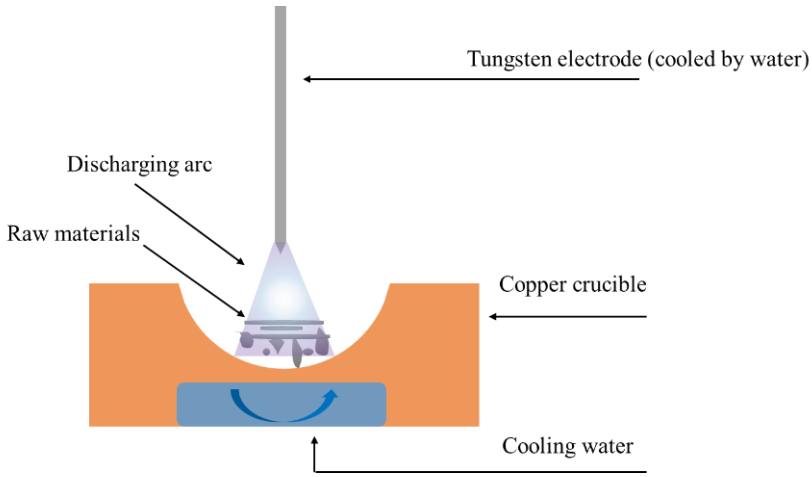

Fig. 2.1. Schematic drawing of the arc-melting furnace.

2.1.2 Melt-spinning

Melt spinning is a sample manufacturing process that is used to produce metals or alloys in the form of metallic glasses, ribbons and foils with a specific microstructure and atomic structure. The cooling rate achieved during melt spinning is of the order of 10^4-10^7 K/s [3]. The melt-spinning device used in this thesis is produced by Edmund Buhler Gmbh company and it consists of a main chamber, a radiofrequency RF generator, an inert gas connection system, a high-vacuum system and a water cooling system. A schematic drawing of the device can be seen in Fig. 2.2. Starting materials in a quartz tube are mounted in the middle of an induction coil. After the vacuum is pumped below 10^{-5} mbar, the chamber will be filled with 700 mbar argon. The molten material is propelled by argon pressure through a nozzle to the surface of a rotating copper wheel in the form of a jet. Due to the low viscosity of the molten alloy, the jet extends only a few micrometres into the puddle and the bottom of the puddle on the copper wheel solidifies into ribbons leaving the wheel in response to the centrifugal force. The microstructure and grain size can be tuned by varying the wheel speed, gas ejection pressure, nozzle-wheel gap and nozzle diameter [4].

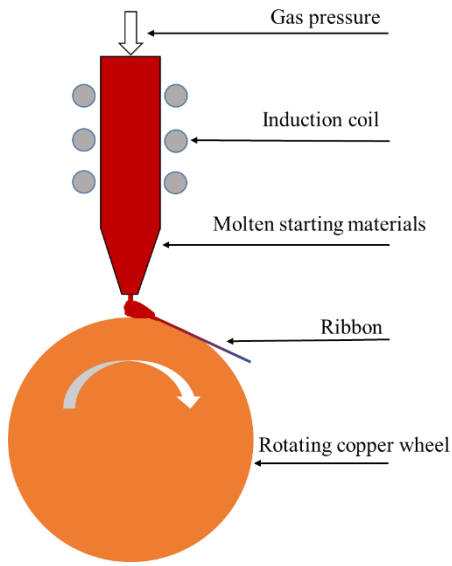

Fig. 2.2. Schematic drawing of the melt-spinning device.

2.2 Crystal structure

2.2.1 X-ray Diffraction

X-ray diffraction (XRD) is a characterisation method to determine the crystal structure of a solid material. The diffraction pattern indicates constructive interference when the Bragg's condition: $2d \sin\theta = n\lambda$ is met, where θ is the angle between the incident beam and the reflected beam, λ is the wavelength of the X-ray, n is the diffraction order and d is the distance between two crystal planes. From the XRD measurements information on the crystal structure, grain size and atom occupation can be derived by refining the measurement patterns with a crystal lattice model. The XRD data in this thesis were acquired with a Panalytical X-Pert PRO using Cu K_α radiation and an Anton Paar TTK 450 temperature chamber. The lattice constants and atom occupation were analysed by Rietveld refinement using the Fullprof software [5].

2.2.2 Neutron Diffraction

Neutron diffraction (ND) is a form of elastic scattering in which a solid material is exposed to a neutron beam. ND is a complementary method to XRD, where neutrons and X-rays have a different sensitivity for the elements that are present in the lattice structure. In contrast to X-rays which are scattered by the electrons and are therefore more sensitive for the heavier elements, neutrons interact with the atomic nuclei and the unpaired electrons. Therefore, ND can not only provide information about the crystal structure, such as the occupation of light elements or neighbouring elements, but can also provide information about the magnetic structure and the size of the magnetic moments in the lattice structure. Unlike X-rays or electrons, neutrons have no charge and their interactions with the nuclei are short-range, so that they can in most cases penetrate the material more easily than charged particles. In this thesis, ND data were collected at a neutron wavelength of 1.6672 Å using the ND instrument PEARL [6] at the research reactor of the Delft University of Technology. The crystal symmetry, the atomic occupancies, and magnetic structure were obtained using the Rietveld refinement method implemented in the Fullprof software package [7-9].

2.2 Microstructure

2.2.1 Scanning Electron Microscopy

Scanning electron microscopy (SEM) is a method that provides information about the sample's surface (or near-surface) composition and defect structure in the submicron and nanometre level from images produced by a high-energy electron beam on the sample surface. The electron beam penetrates up to a few microns into the sample surface and interacts with atoms in the sample to generate signals from secondary electrons and backscattered electrons. In this way, images and chemical information can be obtained. Since the electron beam can interact with the electrons of the sample, X-rays with specific energies can be emitted so that the composition of the sample surface can be analysed. In this thesis the microstructure was analysed by SEM using a FEI Quanta FEG 450 equipped with energy dispersive X-Rays spectroscopy (EDS).

2.2.2 Electron Probe Micro Analysis

Similar to SEM, Electron probe micro-analysis (EPMA) is also a non-destructive method for determining the chemical composition of solid materials. Unlike EDS using a semiconductor to accumulate the X-ray signals produced by the interactions with the sample at all wavelengths, resulting in relatively short counting times, Wavelength-dispersive spectrometry (WDS) uses Bragg' law to collect the X-rays of interest leading to an improved accuracy, which however requires longer count times. For the detection of light elements such as Li, Be and B, WDS is a better choice compared to EDS. In Chapter 3, the microstructure was also analysed using the EPMA instrument model JEOL JXA 8900R, which is equipped with WDS.

2.3 Calorimetry measurements

Differential scanning calorimetry (DSC) is a thermal analysis technique that involves monitoring both heat flux and temperature of a sample and a reference, allowing for the measurement of difference in heat flow between the two as a function of temperature. Zero-magnetic-field DSC measurements were performed in a

commercial TA-Q2000 DSC calorimeter (at a sweep rate of 10 K/min), and in-field DSC characterization was performed in a home-built Peltier cell-based device to derive the calorimetric ΔS_m and ΔT_{ad}. The working principle of the in-field DSC is similar to that of the zero-field DSC, but the goal of the former is to accurately measure the heat capacity in different fields to calculate the magnetic entropy change or the adiabatic temperature change [10, 11]. The specific heat of the sample as a function of temperature and magnetic field are both measured at a slow thermal ramp rate (1 K/min) to minimize the radiative heat loss.

2.4 Magnetic measurements

A superconducting quantum interference device (SQUID) is used to measure subtle magnetic fields generated by a magnetised sample. The operation of the SQUID is based on a superconducting loop with two Josephson junctions, which consist of two superconducting electrodes separated by an insulting layer. When a magnetic sample travels through a series of magnetic coils, a current is induced in the pickup coils, which is by a secondary coil transferred to a magnetic field that penetrates the superconducting loop. The magnetic field causes a modulation of the critical supercurrent through the junctions. A feedback loop is used to keep the current constant, which provides a signal proportional to the magnetization. The magnetic properties at low temperatures (4–370 K) were measured using the SQUID model MPMS-XL magnetometer, which is equipped with the option of a reciprocating sample. Magnetisation measurements at high temperatures (315–650 K) were made using a vibrating sample magnetometer (VSM) model LakeShore 7307 equipped with a high-temperature furnace (model 73034).

2.5 Mössbauer spectroscopy

The Mössbauer effect (recoil-free emission and absorption of gamma rays from a nuclear transition) was first discovered by Rudolf Mössbauer in 1957. Mössbauer spectroscopy is a high-resolution spectroscopic technique that can provide information about the chemical environment and the local magnetic field of specific atoms (often iron). Three types of nuclear interactions are probed: (a) the isomer shift,

which is related to the difference in electron density; (b) the quadrupole splitting, which is related to the atomic electric field gradient; and (c) the magnetic Zeeman splitting, which is related to the local hyperfine magnetic field [12]. Transmission ^{57}Fe Mössbauer spectra were collected at various temperatures with a conventional constant-acceleration or sinusoidal velocity spectrometer using a ^{57}Co(Rh) source. The velocity calibration was performed using an α-Fe foil at room temperature. The source and the absorbing sample were kept at the same temperature during the cryogenic measurements. The Mössbauer spectra were fitted using the Mosswinn 4.0 program [13].

2.6 Thermodynamic calculations of the magnetocaloric effect

One of the popular methods to calculate magnetic entropy change is using one of the Maxwell relations and apply it on a series of *M-T* curves at various magnetic fields [14]. The relation between the magnetic entropy change, the magnetic field, temperature and magnetization can be derived from basic thermodynamic relations. In the following the relevant equations in terms of these four parameters are derived.

Based on the first law of thermodynamics (law of energy conservation), the total differential of the internal energy of a system corresponds to:

$$dU = dQ - dW \tag{2.1}$$

where Q is the thermal energy and W is the work done by an external force. According to the second law of thermodynamics, the entropy change in a reversible process corresponds to:

$$dS = \frac{dQ}{T} \tag{2.2}$$

If the work is provided only by a volume change then one finds

$$dW = pdV \tag{2.3}$$

Implementing equations (2.2) and (2.3) into (2.1), one obtains:

$$dU = TdS - pdV \tag{2.4}$$

When a magnetic field is applied to the system, the differential of the work is:

$$dW_{mag} = \mu_0 H dM \tag{2.5}$$

where H is the applied magnetic field and M is the magnetization. In this case equation (2.4) can be rewritten as:

$$dU = TdS - pdV + \mu_0 H dM \tag{2.6}$$

According to the second law of thermodynamics, the decrease in free energy is the largest work that can be isothermally extracted from the system. If the work from the volume change and the magnetic field is involved, then the Gibbs free energy G can be defined as:

$$G = U - TS + pV - \mu_0 H dM \tag{2.7}$$

Correspondingly, we can obtain the differential dG from equation (2.7). By introducing equation (2.6) into the differential dG, we can obtain:

$$d\mathrm{G} = -SdT - Md\mu_0 H + Vdp \tag{2.8}$$

Based on the above relations, the total differential of G at constant pressure can be written as:

$$dG(T,H) = \left(\frac{\partial G}{\partial T}\right)_H dT + \left(\frac{\partial G}{\partial H}\right)_T dH \tag{2.9}$$

Due to the symmetry properties for second derivatives, the crossed second derivatives of dG are equal:

$$\left(\frac{\partial}{\partial H}\left(\frac{\partial G}{\partial T}\right)_H\right)_T = \left(\frac{\partial}{\partial T}\left(\frac{\partial G}{\partial H}\right)_T\right)_H \tag{2.10}$$

As a result, the following relations can be obtained in terms of the partial derivatives of G:

$$S(T,H) = -\left(\frac{\partial G}{\partial T}\right)_H \tag{2.11}$$

$$M(T,H) = -\left(\frac{\partial G}{\partial H}\right)_T \tag{2.12}$$

By implementing equation (2.11) and (2.12) into (2.10), one obtains the following Maxwell relation:

$$\left(\frac{\partial S}{\partial H}\right)_T = \left(\frac{\partial M}{\partial T}\right)_H \tag{2.13}$$

Therefore, the isothermal magnetic entropy change ΔS_m between the initial applied magnetic field $\mu_0 H_0$ and the final applied magnetic field $\mu_0 H_1$ can be determined as:

$$\Delta S_m(T, \Delta H) = \int_{\mu_0 H_0}^{\mu_0 H_1} \left(\frac{\partial M}{\partial T}\right)_H dH \tag{2.14}$$

If the field is applied adiabatically, by combining equation (2.14) with the corresponding TdS equation, the adiabatic temperature ΔT_{ad} is equal to:

$$\Delta T_{ad}(T, \Delta H) = -\int_{\mu_0 H_0}^{\mu_0 H_1} \frac{T}{C_p\,(T,H)} \left(\frac{\partial M}{\partial T}\right)_H dH \tag{2.15}$$

where C_p is the heat capacity.

References

[1] A. K. Tyagi, Handbook on Synthesis Strategies for Advanced Materials (R. S. Ningthoujam, Ed.), Indian Institute of Metals Series 1 (2021).

[2] M. Boeije, Electron density studies on magnetic systems, TU Delft thesis (2017).

[3] L.A. Reza Abbaschian, Robert E. Reed-Hill, Physical Metallurgy, Elsevier 4 (2009).

[4] R.C. Budhani, T.C. Goel, K.L. Chopra. Melt-spinning technique for preparation of metallic glasses, Bull. Mater. Sci 4 (1982) 549-561.

[5] B.H. Toby, R factors in Rietveld analysis: How good is good enough?, Powder Diffr. 21 (2012) 67-70.

[6] L. van Eijck, L.D. Cussen, G.J. Sykora, E.M. Schooneveld, N.J. Rhodes, A.A. van Well, C. Pappas, Design and performance of a novel neutron powder diffractometer: PEARL at TU Delft, J. Appl. Crystallogr. 49 (2016) 1398-1401.

[7] H.M. Rietveld, Line profiles of neutron powder-diffraction peaks for structure refinement, Acta cryst. 22 (1967) 151-152.

[8] T.M. Sabine, Powder Neutron Diffraction-Refinement of the Total Pattern, J. Appl. Cryst. 10 (1977) 277-280.

[9] J. Rodriguez-Carvajal, Recent advances in magnetic structure determination by neutron powder diffraction, Physica B 192 (1993) 55-69.

[10] G. Porcari, S. Fabbrici, C. Pernechele, F. Albertini, M. Buzzi, A. Paoluzi, J. Kamarad, Z. Arnold, M. Solzi, Reverse magnetostructural transformation and adiabatic temperature change in Co- and In-substituted Ni-Mn-Ga alloys, Phys. Rev. B 85 (2012) 024414.

[11] G. Porcari, M. Buzzi, F. Cugini, R. Pellicelli, C. Pernechele, L. Caron, E. Bruck, M. Solzi, Direct magnetocaloric characterization and simulation of thermomagnetic cycles, Rev. Sci. Instrum. 84 (2013) 073907.

[12] O. Eriksson, A. Svanet, Isomer shifts and hyperfine fields in iron compounds, J. Phys.: Condens. Matter l (1989) 1589-1599.

[13] Z. Klencsar, Mössbauer spectrum analysis by evolution algorithm, Nucl. Instrum. Meth. B 129 (1997) 527-533.

[14] L. Caron, Z.Q. Ou, T.T. Nguyen, D.T. Cam Thanh, O. Tegus, E. Brück, magnetic entropy change in materials with first-order transitions, J. Magn. Magn. Mater. 321 (2009) 3559-3566.

Chapter 3 Nonlinear influence of excess Mn on the magnetoelastic transition in (Mn,Cr)$_2$Sb

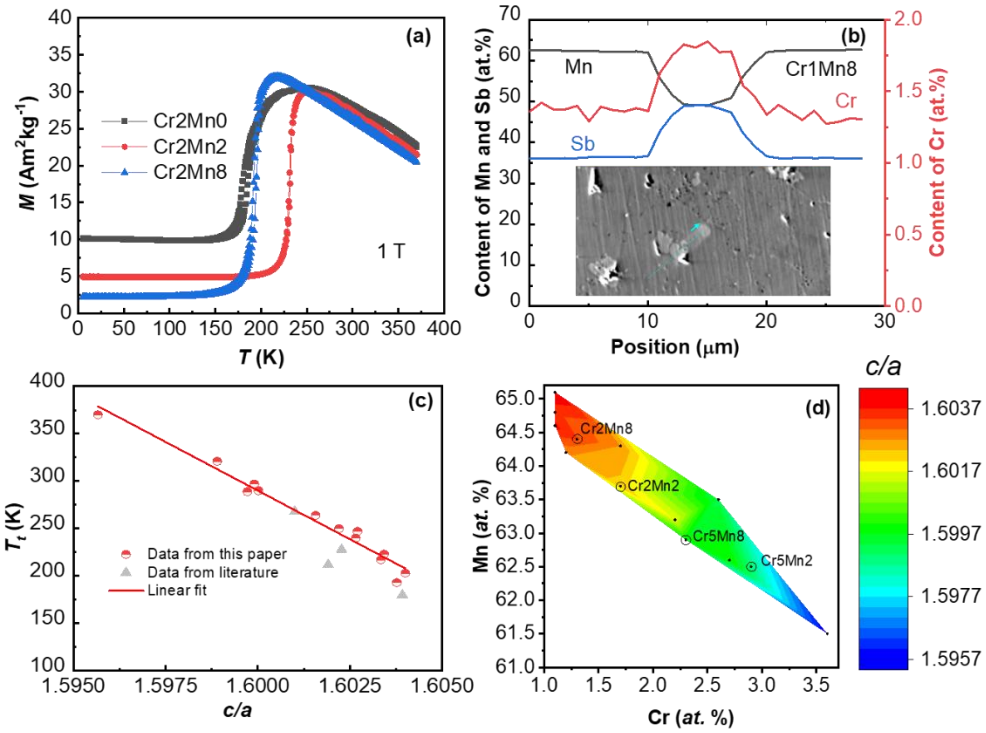

This chapter is based on:

Q. Shen, I. Batashev, H. Ojiyed, F. Zhang, N. van Dijk, E. Brück, Nonlinear influence of excess Mn on the magnetoelastic transition in (Mn,Cr)$_2$Sb, J. Alloys Compd. 903 (2022) 164011.

Abstract

The influence of excess Mn on the magnetoelastic ferromagnetic-to-antiferromagnetic transition in the magnetocaloric compound $(Mn,Cr)_2Sb$ has been studied. With increasing excess Mn the magnetoelastic transition temperature T_t for $(Mn,Cr)_2Sb$ initially increases and then decreases. This trend is accompanied by a strong reduction of the (Mn,Cr)Sb secondary phase. With increasing excess Mn a higher Cr content was found in the (Mn,Cr)Sb secondary phase in comparison to the matrix phase. This competition for Cr leads to a nonlinear dependence of T_t with increasing excess Mn at a fixed nominal Cr content. However, we observed that T_t depends linearly on the *c/a* ratio for a wide range of temperatures from 170 to 350 K. A compositional diagram of the *c/a* ratio was constructed to assist the selection of $(Mn,Cr)_2Sb$ alloys with a desired transition temperature.

3.1 Introduction

The magnetocaloric effect (MCE), associated with either an isothermal entropy change or an adiabatic temperature change in the presence of a change in magnetic field, can be used for magnetic refrigeration and waste heat recovery [1, 2]. A tuneable transition temperature and a narrow thermal hysteresis are two basic requirements of promising magnetocaloric materials for these two environmentally friendly applications [3, 4]. In recent years Mn_2Sb-based alloys undergoing a first-order magnetoelastic transition (FOMT) from a ferrimagnetic state to an antiferromagnetic state (FIM-AFM) at critical temperature T_t attract increasing attention [5-7]. The FOMT has been studied in many Mn_2Sb-based compounds with elemental substitution such as V [8], Cr [5], Zn [9], Co [10] on the Mn sites or Sn [11], As [12], Ge[13], Bi [14, 15] on the Sb site. Among these compounds, Cr-doped Mn_2Sb is one of the most promising magnetocaloric candidate materials with a wide range of FOMT temperatures ranging from 220 to 340 K, a narrow thermal hysteresis (less than 2 K), a large inverse magnetocaloric entropy change of 7.5 J/kgK [5] and an adiabatic temperature change of 2 K under a field change of 5 T [7]. The $(Mn,Cr)_2Sb$ compounds have a tetragonal Cu_2Sb-type crystal structure and order ferrimagnetically below a transition temperature (T_C) of 550 K. The Mn atoms occupy two different crystallographic sites: Mn-I (2*a*) with a magnetic moment of 2.1 μ_B and Mn-II (2*c*) with a magnetic moment of 3.9 μ_B [16]. Along the *c* axis the Mn-I and Mn-II moments align parallel or antiparallel to each other between layers corresponding to the ferrimagnetic or the antiferromagnetic structure, respectively. The FIM-AFM transition finds its origin in the chemical compression introduced by smaller atom substitutions for Mn or Sb in the typical case of $(Mn,Cr)_2Sb$ [5, 17] or by enhanced thermal expansion in the case of $Mn_2(Sb,Bi)$ [14, 18]. Upon cooling, the lattice parameter *c* of the $(Mn,Cr)_2Sb$ compounds decreases below a critical value, resulting in an exchange inversion for adjacent Mn-II moments, accompanied by a large magnetization jump at the FIM-AFM transition [17].

In the $(Mn,Cr)_2Sb$ compounds the FIM-AFM magnetization jump is generally reduced by the presence of a MnSb-type impurity phase. MnSb is a ferromagnet with

a Curie temperature of T_C = 588 K. The unavoidable MnSb impurity is related to an instability of the Mn_2Sb main phase below 900 K [19]. The evaporation of Mn enhances the tendency towards the non-stoichiometric Mn-deficient side. Therefore, a small amount of excess Mn is added during the arc-melting process to compensate for the evaporation of Mn [15, 20, 21]. However, some residual Mn (beyond the amount of compensating for evaporation) easily remains in the samples [21], which may influence the chemical composition and the FOMT transition of the main phase due to the large magnetic moment of Mn atoms in Mn_2Sb-based alloys. We find from our study adding different amount of excess Mn, that in order to obtain the desired $(Mn,Cr)_2Sb$ alloys with large step in magnetization for magnetocaloric applications, it is very important to study the properties of nonstoichiometric $(Mn,Cr)_2Sb$ alloys. Therefore, we investigated in this paper the influence of excess Mn on the magnetoelastic transition and magnetocaloric effect in $(Mn,Cr)_2Sb$ compounds with an excess 0, 2 and 8 *wt.*% Mn.

3.2 Experimental methods

Thirteen polycrystalline $(Mn,Cr)_2Sb$ compounds with an excess 0, 2 and 8 *wt.*% Mn were prepared from high-purity elements (Mn 99.9%, Cr 99.995%, Sb 99.5%) by arc melting. The starting compositions are indicated as Cr*x*Mn*y*, where *x* and *y* correspond to the nominal Cr content and excess Mn in *wt.*%, respectively. The arc-melted samples were annealed for homogenization under argon atmosphere at 1073 K for 5 days. The compositions of the resulting alloys given in Table 1 were determined by the Energy Dispersive X-ray Spectroscopy (EDS). X-ray diffraction (XRD) data were collected with a Panalytical X-Pert PRO using Cu-K_α radiation. The lattice constants were analysed by Rietveld refinement using Fullprof [22]. The microstructure was analysed by Electron Probe Micro Analysis (EPMA) model JEOL JXA 8900R equipped with the Wavelength Dispersive Spectrometry (WDS) and the Scanning Electron Microscopy (SEM) model FEI Quanta FEG 450 equipped with the EDS. The magnetic properties in the temperature range of 5-370 K were measured on a superconducting quantum interference device (SQUID) magnetometer model MPMS-XL, equipped with the reciprocating sample option. The high-temperature

magnetic measurements in the range 315-600 K were carried out using a vibrating sample magnetometer (VSM) model LakeShore 7307 equipped with a high-temperature oven (Model 73034). T_C is obtained from the maximum absolute temperature derivative of the magnetisation $|dM/dT|$ in the heating curve under a magnetic field of 0.01 T. The transition temperature T_t is determined from the corresponding temperature of maximal value of dM/dT under a magnetic field of 1 T, to avoid interference with the spin reorientation effect that is present in low magnetic fields.

3.3 Results and discussion

Fig. 3.1(a) and (b) show the XRD data at room temperature for the Cr2Mn*y* (*y* = 0, 2, 8 *wt.*%) samples (nominal 2.7 *wt.*% Cr) and the Cr*x*Mn2 (*x* = 1, 2, 3, 4, 5, 6 *wt.*%) samples (nominal excess 2 *wt.*% Mn), respectively. The main phase is identified as the tetragonal CuSb-type $(Mn,Cr)_2Sb$. The XRD patterns show a preferred orientation signalled by the enhanced (00*l*) reflections in all samples, which have also be observed in Cr-modified Mn_2Sb [5] and in Co-modified Mn_2Sb [10]. Besides the main phase, the peaks around 29° and 40° indicate the hexagonal impurity phase (Mn,Cr)Sb. The fraction of secondary phase is given by SEM images instead of XRD refinement because of the preferred orientation. The (Mn,Cr)Sb peaks show a strong decrease in intensity with increasing excess Mn in Fig. 3.1(a), whereas an increase is observed with increasing Cr substitution in Fig. 1(b). Excess Mn is found to suppress the Mn-deficient tendency [20], but increasing Cr enhances this tendency since Cr occupies the Mn-I site, as determined by neutron diffraction [23]. As shown in Fig. S3.1 in the Supplementary Material, adding excess Mn reduces the fraction of secondary phase in low-Cr content samples, but has limited contribution to reducing the fraction of secondary phase in high-Cr content samples. The lattice parameters *c* (6.5369 Å for Cr2Mn0, 6.5364 Å for Cr2Mn2, 6.5377 Å for Cr2Mn8) and the *c/a* ratio (1.6027 for Cr2Mn0, 1.6022 for Cr2Mn2, 1.6033 for Cr2Mn8) initially decrease with 2 *wt.*% excess Mn and then increase with 8 *wt.*% excess Mn, displaying the opposite trend with the unit-cell volume of the main phase, as shown in Fig. 3.1(c). With the increase in excess Mn, the enhanced unit-cell volume of the main phase

indicates that 2 *wt.*% of excess Mn enters Mn voids caused by the Mn-deficient tendency of Mn_2Sb phase [20]. When the excess Mn increases up to 4 *wt.*%, the unit-cell volume of the main phase starts to decrease, suggesting that the additional Mn (beyond 2 *wt.*%) replaces Sb due to the smaller atom size of Mn compared to Sb. Meanwhile, due to the smaller atom size of Cr compared to Mn, the trend of a decreasing unit-cell volume for (Mn,Cr)Sb in Fig. 3.1(d) implies an increase in Cr content in the (Mn,Cr)Sb secondary phase.

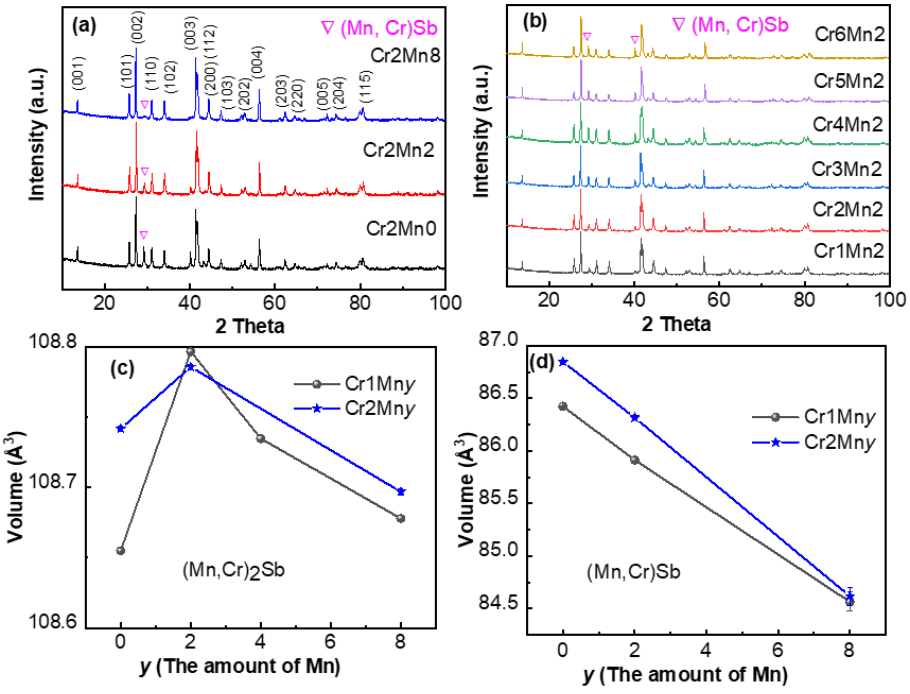

Fig. 3.1. XRD patterns for (a) Cr2Mn*y* samples (*y* = 0, 2, 8) (b) Cr*x*Mn2 samples (*x* = 1, 2, 3, 4, 5, 6). Excess Mn content dependence of the unit-cell volume (c) for the $(Mn,Cr)_2Sb$ main phase and (d) for the (Mn,Cr)Sb secondary phase.

The back-scattered SEM images of the Cr2Mn0, Cr2Mn2 and Cr2Mn8 samples are shown in Fig. 3.2(a-c). The white area and the black spots are determined by EDS to be secondary (Mn,Cr)Sb and Mn phases, respectively. The volume fraction of the secondary phases shows a sharp decrease with increasing excess Mn: 10% for Cr2Mn0, 4% for Cr2Mn2 and 1% for Cr2Mn8 (obtained by image analysis

with the software package ImageJ). The absence of the Mn phase in the XRD patterns can be attributed to the fact that the amount is too small to be detected. The cracks observed for the Cr2Mn0 and Cr2Mn2 samples are probably caused by the difference in thermal expansion for the $(Mn,Cr)_2Sb$ and (Mn,Cr)Sb phases. Table 3.1 gives the chemical compositions of the $(Mn,Cr)_2Sb$ alloys determined by EDS. Generally, the content of Cr in $(Mn,Cr)_2Sb$ increases with the increasing nominal Cr content and the increasing nominal excess Mn content. The content of Cr fluctuates for the different amounts of excess Mn, except for Cr1Mn*y* (y = 0, 2, 8) samples, which have ultra-low Cr contents. The same Cr content in the main phase for Cr2Mn2 and Cr3Mn2 can be ascribed to the fact that the latter has more (Mn,Cr)Sb secondary phase, as indicated in XRD patterns in Fig.3.1 (b). Compared with the Cr*x*Mn2 samples (x = 2, 5), the Cr*x*Mn8 samples (x = 2, 5) tend to have lower Cr contents, which indicates that too much excess Mn expels Cr from the main phase to the secondary phases. The chemical composition of the Cr1Mn2 sample was also confirmed by WDS to be $Mn_{62.7}Sb_{35.9}Cr_{1.4}$ obtained from the average of 19 points, which is slightly different from $Mn_{64.8}Sb_{34.1}Cr_{1.1}$ determined by EDS. The elemental composition variation for (Mn,Cr)Sb and $(Mn,Cr)_2Sb$ can be compared from the line scans by WDS for the Cr1Mn2 sample in Fig. 3.2(d). We found 1.8 *at.*% Cr in the (Mn,Cr)Sb secondary phase and 1.4% *at.*% Cr in the main phase, which indicates the preference of Cr for the (Mn,Cr)Sb secondary phase.

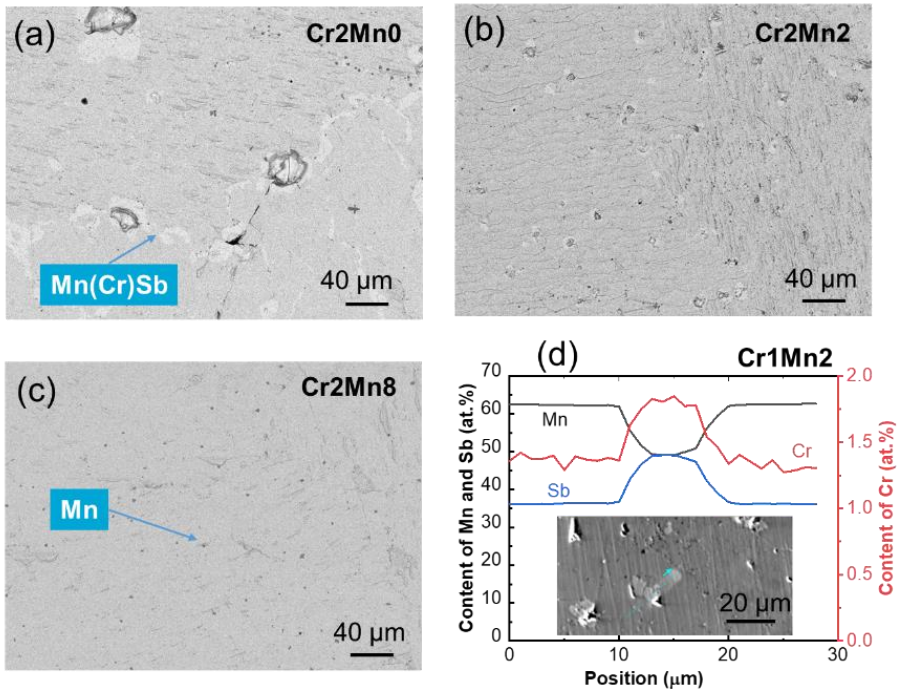

Fig. 3.2. (a-c) Back-scattered SEM images for the Cr2Mn*y* (*y* = 0, 2, 8) samples. (d) Line scans through the white secondary phase in the inserted EPMA images for the Cr1Mn2 sample.

Table 3.1 Main-phase composition (in *at.*%) determined by EDS for the (Mn,Cr)$_2$Sb alloys.

	Cr1 Mn0	Cr1 Mn2	Cr1 Mn8	Cr2 Mn0	Cr2 Mn2	Cr2 Mn8	Cr3 Mn0	Cr3 Mn2	Cr4 Mn0	Cr4 Mn2	Cr5 Mn2	Cr5 Mn8	Cr6 Mn2
Cr	1.1	1.1	1.1	1.2	1.7	1.3	2.2	1.7	2.6	2.7	2.9	2.3	3.6
Mn	64.6	64.8	65.1	64.2	63.7	64.4	63.2	64.3	63.5	62.6	62.5	62.9	61.5
Sb	34.3	34.1	33.7	34.6	34.6	34.3	34.6	34.0	33.9	34.7	34.6	34.8	35.0

Fig. 3.3(a-b) display the *M*-*T* curves for the Cr2Mn*y* (*y* = 0, 2, 8). Upon cooling, a sharp magnetization jump at T_t in Fig. 3.3(a) almost free of hysteresis reflects the magnetoelastic FIM-AFM transition. For the Cr2Mn0 sample, the broad transition

and the high residual magnetization below T_t can be accounted by the large fraction of about 10% (Mn,Cr)Sb secondary phase obtained from the SEM image. Compared with the Cr2Mn8 sample, the Cr2Mn2 sample shows a 30 K higher T_t. Similarly, the Cr1Mn2 sample shows a 20 K higher T_t than the Cr1Mn0 and Cr1Mn8 samples (see Fig. S3.2 in the Supplementary Material). Although Cr1Mn4 has a higher T_t than Cr1Mn2, the larger fraction of (Mn,Cr)Sb, indicated from the higher residual magnetization below T_t, makes the magnetization jump smaller for the former than for the latter. The T_C presented in Fig. 3.3(b) shows a slight decrease with the increase in excess Mn: T_C = 535 K for Cr2Mn0; T_C = 528 K for Cr2Mn2 and T_C = 527 K for Cr2Mn8.

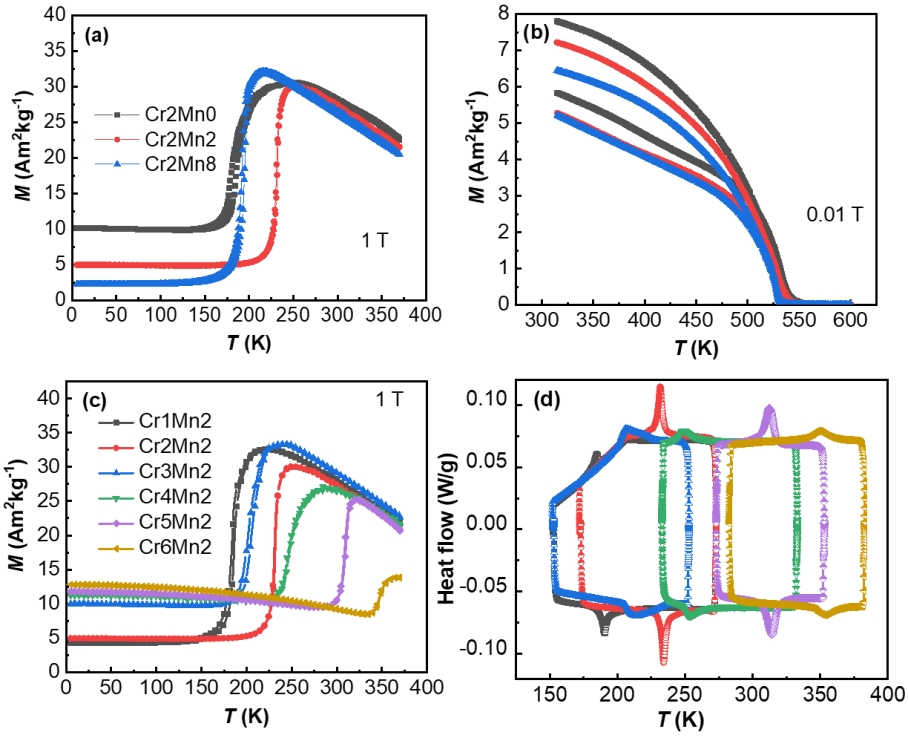

Fig. 3.3. *M-T* curves of Cr2Mn*y* (*y* = 0, 2, 8) in a temperature range of (a) 5–370 K and (b) 315–600 K. (c) *M-T* curves (d) DSC curves for Cr*x*Mn2 (*x* = 1, 2, 3, 4, 5, 6) samples.

Consequently, using 2 *wt*.% excess Mn can help to obtain more pure sample with a higher transition temperature. Fig. 3.3(c) shows the *M-T* curves for the Cr*x*Mn2 (x = 1, 2, 3, 4, 5, 6) samples. Substitution with the smaller element Cr for Mn causes the contraction of the unit cell and thus strengthens the antiferromagnetic interaction between the Mn-II and Mn-II moments [24]. Therefore, the transition temperature T_t shifts to higher temperature with increasing nominal Cr contents except for the Cr3Mn2 sample. The reduction in the magnetization jump with increasing Cr addition corresponds to the increased fraction of (Mn,Cr)Sb. A higher Cr addition supports the tendency towards the Mn-deficient side and inevitably induces more (Mn,Cr)Sb secondary phase. The large exothermal and endothermal peaks depicted in the DSC curves in Fig. 3.3(c) reflect the nature of the FOMT for Cr*x*Mn2 (x = 1, 2, 3, 4, 5, 6) samples. A similar increasing tendency of the transition temperature with increasing Cr addition (except for the abnormal T_t for the Cr3Mn2 sample) are also observed from the DSC curves, in agreement with the *M-T* curves. The latent heat determined from the heating curve for the Cr2Mn2 sample amounts to 1.2 J/g, and the estimated entropy change of about 5.3 J/kg K in the absence of an external magnetic field is close to the value of 5.1 J/kg K reported for $Mn_{1.94}Cr_{0.06}Sb$ [5].

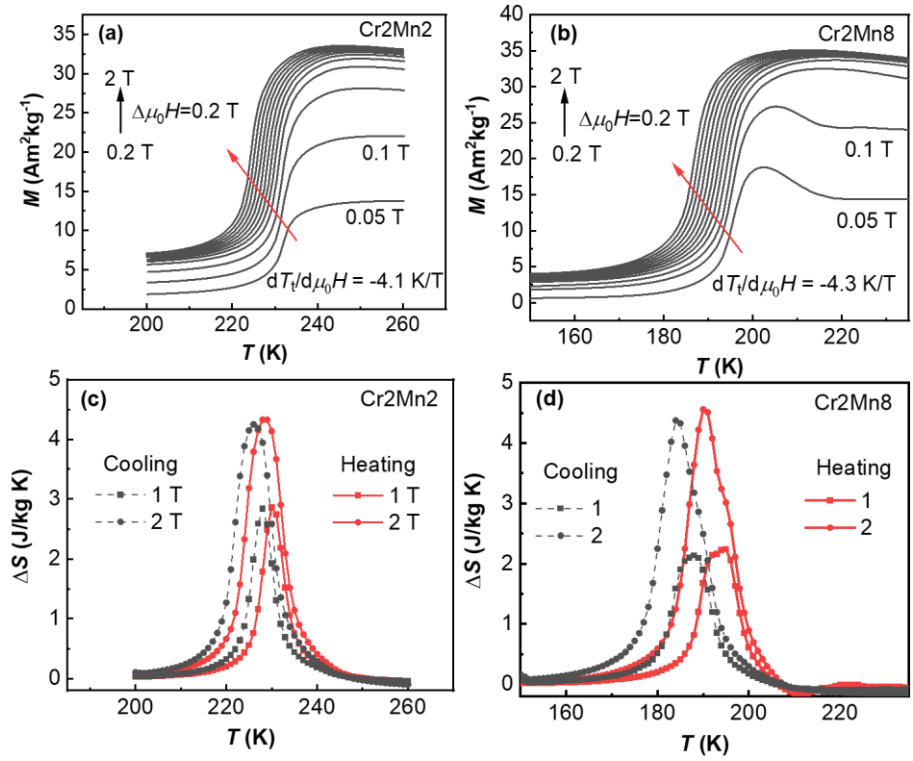

Fig. 3.4. *M-T* curves upon heating in different magnetic fields for (a) Cr2Mn2 and (b) Cr2Mn8. The magnetic entropy change calculated from heating and cooling curves for (c) Cr2Mn2 and (d) Cr2Mn8.

The magnetic entropy changes for the Cr2Mn2 and Cr2Mn8 samples have also been calculated from temperature-dependent magnetization at variable fields as shown in Fig. 3.4. A higher magnetic field stabilizes the FIM state and shifts the transition temperature to a lower temperature. The magnetic field dependence of the transition temperature for Cr2Mn2 and Cr2Mn8 is -4.1 K/T and -4.3 K/T, respectively. For Cr2Mn8, the decrease of magnetization under low magnetic fields around 200 K is due to the spin reorientation effect [21], which is also observed in our previous work on $Mn_2Sb_{1-x}Bi_x$ [14]. The critical magnetic field for this spin-flipping transition is 0.2 T. The entropy change in Fig. 3.4(c) and (d) is calculated based on the integrated Maxwell relation: $\Delta S(\Delta H, T) = \int_{H_0}^{H} \left(\frac{\partial M(T,H)}{\partial T}\right)_H \mathrm{d}\mu_0 H$, where we choose $\mu_0 H_0 = 0$ T. Due to the narrow transitional hysteresis, the magnetic entropy

change derived from cooling curves is essentially the same as that derived from heating curves for both samples. Under a magnetic field change of 2 T, the maximal entropy change in the heating curves is 4.3 J/kg K at 228 K for Cr2Mn2 and 4.6 J/kg K at 190 K for Cr2Mn8 sample, which are similar values as those reported in the literature [5, 7]. Therefore, the amount of excess Mn can shift the working temperature to a lower temperature without sacrificing the magnetic entropy change.

The evolution of T_t with increasing Cr and excess Mn contents can be explained by the linear relation between T_t and *c/a*, as displayed in Fig. 3.5(a-c). Compared with T_C, the transition temperature T_t is much more sensitive to the *c/a* ratio. In Fig. 3.5(a), the grey data points obtained from literature [5, 21, 25] are approximately in line with the linear trend. Furthermore, the *c/a* ratio shows a linear dependence on the Cr concentration in the main phase as depicted in Fig. 3.5(b). A larger *c/a* ratio for Cr3Mn2 (1.6027) than Cr2Mn2 (1.6022) results in a lower T_t for Cr3Mn2, which can be ascribed to the competition for Cr between the secondary phase and the main phase, as indicated by the same amount of Cr 1.7 *at.*% determined by the EDS for Cr3Mn2 and Cr2Mn2 main phases. In order to further illustrate the relation between chemical composition and T_t, the relation between chemical composition and *c/a* is displayed in Fig. 3.5(c). The smallest *c/a* ratio corresponds to the highest T_t in the high-Cr and low-Mn region, as seen from the higher T_t in Cr*x*Mn2 samples (x = 2, 5) than Cr*x*Mn8 samples (x =2, 5). Since too much excess Mn expels Cr from the main phase to the secondary phases, one should be cautious to add excess Mn when preparing arc-melted $(Mn,Cr)_2Sb$ samples. With the linear relation between T_t and *c/a,* and the chemical composition diagram, we can now easily tune the desired transition temperature for the Cr-doped Mn_2Sb compounds.

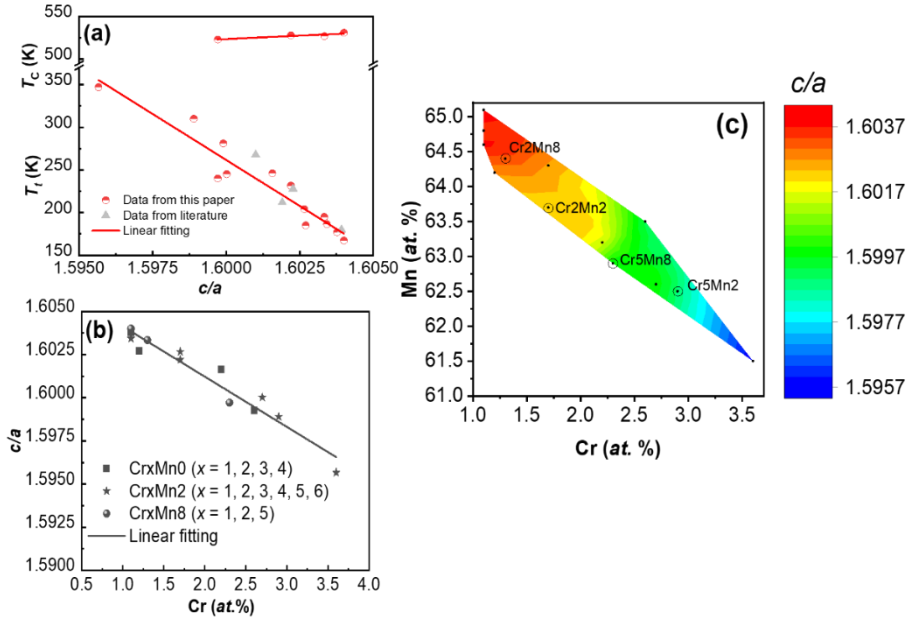

Fig. 3.5. (a) T_t and T_C as a function of the *c/a* lattice parameter ratio. Grey data points are from literature [5, 21, 25]. (b) The ratio of *c/a* lattice parameter dependence of Cr concentration determined by EDS. (c) Composition for the $(Mn,Cr)_2Sb$ compounds as a function of the *c/a* lattice parameter ratio. The black points correspond to the experimental data. All data are measured in the ferrimagnetic state.

3.4 Conclusions

The influence of excess Mn on the magnetoelastic transition of $(Mn,Cr)_2Sb$ has been investigated in this work. The fraction of the (Mn,Cr)Sb secondary phase strongly reduces with increasing excess Mn, while the magnetoelastic transition temperature initially increases and then decreases with excess Mn. By Electron Probe Micro Analysis we find that with increasing excess Mn a higher Cr content is found in the (Mn,Cr)Sb secondary phase in comparison to the matrix. This competition for Cr leads to the nonlinear influence of excess Mn on the magnetoelastic transition temperature. However, we observed that T_t scales linearly with the *c/a* lattice parameter ratio for a wide temperature range of 170–350 K. A large magnetic entropy change of 4.6 J/kg K under 2 T is obtained and a composition diagram for the *c/a*

ratio is established to give guidance in the preparation of $(Mn,Cr)_2Sb$ alloys with a desired transition temperature for magnetocaloric applications.

References

[1] O. Gutfleisch, M.A. Willard, E. Bruck, C.H. Chen, S.G. Sankar, J.P. Liu, Magnetic materials and devices for the 21st century: stronger, lighter, and more energy efficient, Adv. Mater. 23 (2011) 821-842.

[2] S.M. Sandoval, K.P. Wetzlar, G.P. Carman, Thermomagnetic conversion efficiencies for ferromagnetic materials, J Appl. Phys. 110 (2011) 123923.

[3] N.H. Dung, Z.Q. Ou, L. Caron, L. Zhang, D.T.C. Thanh, G.A. de Wijs, R.A. de Groot, K.H.J. Buschow, E. Brück, Mixed Magnetism for Refrigeration and Energy Conversion, Adv. Energy Mater. 1 (2011) 1215-1219.

[4] F. Guillou, G. Porcari, H. Yibole, N. van Dijk, E. Bruck, Taming the first-order transition in giant magnetocaloric materials, Adv. Mater. 26 (2014) 2671-2675.

[5] L. Caron, X.F. Miao, J.C.P. Klaasse, S. Gama, E. Brück, Tuning the giant inverse magnetocaloric effect in $Mn_{2-x}Cr_xSb$ compounds, Appl. Phys. Lett. 103 (2013) 112404.

[6] F. Cheng, S. Ma, Y. Wang, X. Ke, J. Wang, S. Yang, Tuning Magnetocaloric Effect of a Mn-Cr-Sb-Ga alloy by the Nonvolatile Residual Strain of a Ti-Ni Shape Memory Alloy, Acta Mater. 210 (2021) 116849.

[7] A. Tekgül, M. Acet, F. Scheibel, M. Farle, N. Ünal, The reversibility of the inverse magnetocaloric effect in $Mn_{2-x}Cr_xSb_{0.95}Ga_{0.05}$, Acta Mater. 124 (2017) 93-99.

[8] W. Cui, W.J. Ren, Z.D. Zhang, X. Zhou, H. Zhong, Q. Wang, Lattice distortion tuning of the metamagnetic phase transition in tetragonal Cu_2Sb-type $Mn_{1.95}V_{0.05}Sb$ alloy, Scripta Mater. 143 (2018) 59-62.

[9] V.I. Val'kov, A.V. Golovchan, I.F. Bribanov, V.I. Kamenev, O.O. Iesenchuk, A.P. Sivachenko, N.N. Kabdin, Stability characteristics of the low temperature

ferrimagnetism in the $Mn_{2-x}Zn_xSb$ system system, Low Temp. Phys. 33 (2007) 70-78.

[10] J. Wilden, A. Hoser, M. Chikovani, J. Perßon, J. Voigt, K. Friese, A. Grzechnik, Co- Magnetic Transitions in the Co-Modified Mn_2Sb System, Inorganics, 6 (2018) 113.

[11] V.M. Ryzhkovskii, V. P. Dymont, Z.L. Erofeen, Ferromagnetic-Antiferromagnetic Phase Transition in $Mn_2Sb(Sn)$ Solid Solutions, Phys. Stat. Sol. A 130 (1992) 163-168.

[12] T. Kakimoto, J. Goto, S. Fujii, K. Koyama, S. Ishida, Electronic and Magnetic Properties of $Mn_2Sb_{1-x}As_x$ (x = 0, 0.5, 1), Mater. Trans. 55 (2014) 1878-1884.

[13] J. Zhang, G. Yao, S. Chen, F. Wei, X. Fan, X. Yin, Z. Chen, W. Cui, Q. Wang, The effects of Ge occupation and hydrostatic pressure on the metamagnetic phase transition and magnetocaloric effect in Mn_2Sb alloy, AIP Adv. 9 (2019) 035106.

[14] Q. Shen, I. Batashev, F. Zhang, H. Ojiyed, N. van Dijk, E. Brück, The antiferromagnetic to ferrimagnetic phase transition in $Mn_2Sb_{1-x}Bi_x$ compounds, J Alloys Comp. 866 (2021) 158963.

[15] Z. Zhang, Y. Zhang, X. Luo, S. Ma, H. Zeng, G. Yu, X. Zheng, C. Chen, Y. Hu, F. Xu, S.U. Rehman, Z. Zhong, Self-organized Bi-rich grain boundary precipitates for realizing steep magnetic-field-driven metamagnetic transition in Bi-doped Mn_2Sb, Acta Mater. 200 (2020) 835-847.

[16] M. K. Wilkinson, N. S. Gingrich, C. G. Shull, The magnetic structure of Mn_2Sb, J. Phys. Chem. Solids 2 (1957) 289-300.

[17] C. Kittel, Model of Exchange-Inversion Magnetization, Phys. Rev. 120 (1960) 335-342.

[18] K. Shirakawa, H. Ido, Magnetic transition of intermetallic compounds $Mn_2Sb_{(1-x)}Bi_x$ ($0 \leqslant x \leqslant 0.175$) with Cu_2Sb type structure, J Jpn. Inst. Met. 43 (1979) 636-639.

[19] N. Erick, G. Fredrik, The Mn_2Sb phase composition and thermodynamic properties in the range 298 to 1000 K, J Chem. Therm. 1 (1969) 153-167.

[20] T.J. Swoboda, W.H. Cloud, T.A. Bither, M.S. Sadler, H.S. Jarrett, Evidence for an antiferromagnetic-ferrimagnetic transition in Cr-modified Mn_2Sb, Phys. Rev. Lett. 4 (1960) 509-511.

[21] Y. Cao, K. Xu, Z. Li, Y. Zhang, X. He, Y. Kang, W. Sun, T. Gao, Z. Qian, C. Liu, M. Ye, C. Jing, Interplay between spin reorientation and magnetoelastic transitions, and anisotropic magnetostriction in the $Mn_{1.95}Cr_{0.05}Sb$ single crystal, J. Mag. Magn. Mater. 487 (2019) 165315.

[22] B.H. Toby, Rfactors in Rietveld analysis: how good is good enough, Powder Diffr. 21 (2006) 67-70.

[23] W.H. Cloud, H.S. Jarrett, A.E. Austin, E. Adelson, Neutron diffraction studies of chromium-modified Mn_2Sb, Phys. Rev. 120 (1960) 1969-1970.

[24] Y. Zhang, Z. Zhang, Metamagnetic-transition-induced giant magnetoresistance in $Mn_2Sb_{1-x}Sn_x$ ($0<x\leqslant 0.4$) compounds, Phys. Rev. B, 67 (2003) 132405.

[25] A. Tekgül, Ö. Çakır, M. Acet, M. Farle, N. Ünal, The structural, magnetic, and magnetocaloric properties of In-doped $Mn_{2-x}Cr_xSb$, J. Appl. Phys. 118 (2015) 153903.

Supplementary Material for Chapter 3

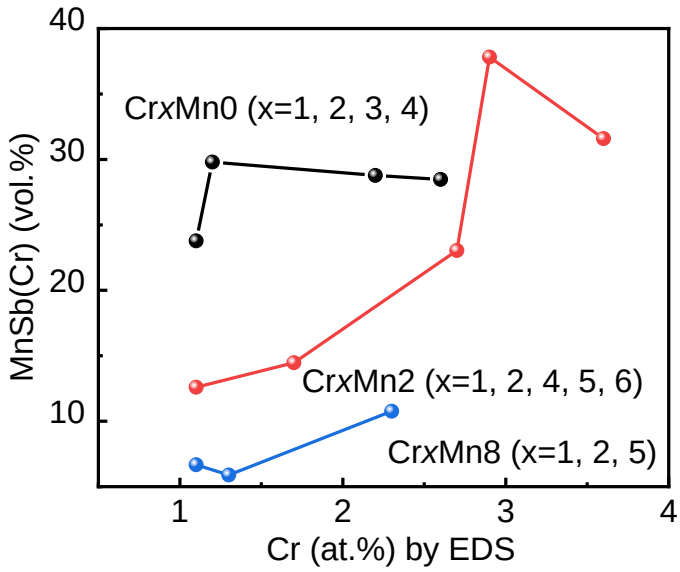

Fig. S3.1. The fraction of secondary phase derived from XRD refinement as a function of Cr concentration by EDS

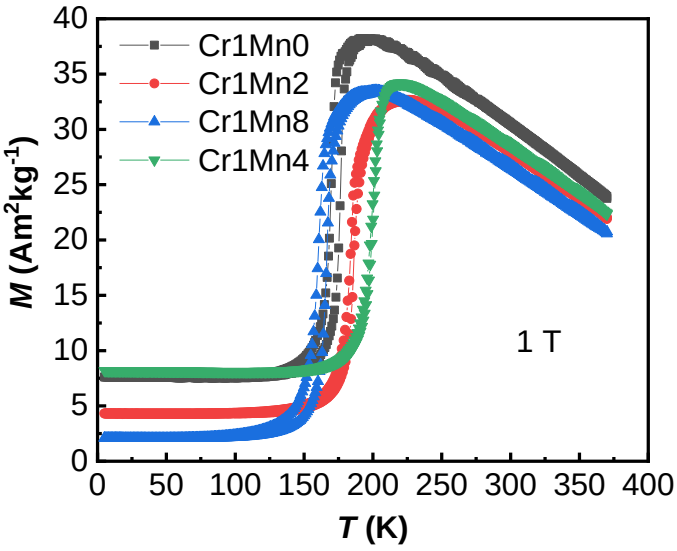

Fig. S3.2. *M-T* curves under a magnetic field of 1 T for a series of Cr1Mn*y* samples with different excess Mn contents.

Chapter 4 The antiferromagnetic to ferrimagnetic phase transition in $Mn_2Sb_{1-x}Bi_x$ compounds

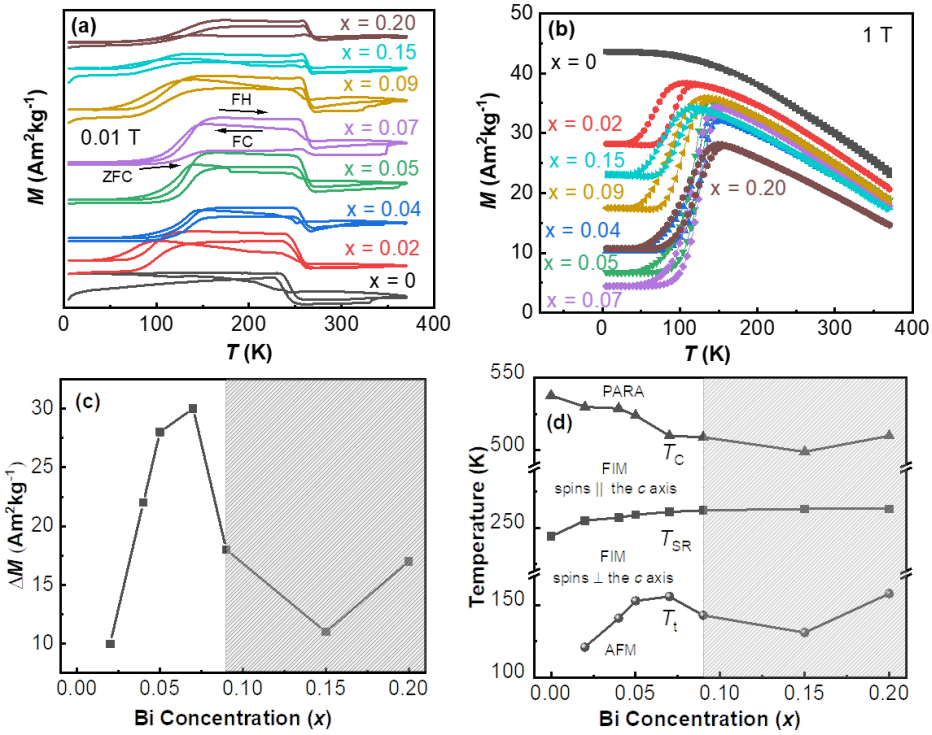

This chapter is based on:

Q. Shen, I. Batashev, F. Zhang, H. Ojiyed, N. van Dijk, E. Brück, The antiferromagnetic to ferrimagnetic phase transition in $Mn_2Sb_{1-x}Bi_x$ compounds, J. Alloys Compd. 866 (2021) 158963.

Abstract

The influence of partial substitution of Bi for Sb on the structure, magnetic properties and magnetocaloric effect of $Mn_2Sb_{1-x}Bi_x$ (x = 0, 0.02, 0.04, 0.05, 0.07, 0.09, 0.15, 0.20) compounds has been investigated. The transition temperature of the antiferro-to-ferrimagnetic (AFM-FIM) transition initially increases with increasing Bi and decreases above 7%. Density functional theory calculations indicate that the Bi atoms prefer to occupy only the Sb site, which accounts for the large magnetization jump in $Mn_2Sb_{0.93}Bi_{0.07}$. As large lattice parameters are found for Bi substituted Mn_2Sb, the origin of the AFM-FIM transition in $Mn_2Sb_{(1-x)}Bi_x$ compounds is ascribed to an enhanced coefficient of thermal expansion along the c axis, resulting from the Bi substitution. The moderate entropy change of 1.17 J/kgK under 2 T originating from the inverse magnetocaloric effect and the strong magnetic field dependence of the transition temperature of $dT_t/d\mu_0H$ = -5.4 K/T in $Mn_2Sb_{0.95}Bi_{0.05}$ indicate that this alloy is a promising candidate material for magnetocaloric applications.

4.1 Introduction

Magnetic refrigeration and waste heat recovery are environmentally-friendly technological applications based on the magnetocaloric effect (MCE) [1, 2]. MCE can be characterized by an isothermal entropy change or an adiabatic temperature change when the material is exposed to a change in external magnetic field. Most giant MCE materials present a large MCE at an order-disorder transition accompanied with a change in symmetry (with a large volume change), as found in Gd-Si-Ge [3], MnAs [4] and Ni-Mn-based Heusler alloys [5], or an order-disorder transition without a change in symmetry, as found in La-Fe-Si [6] and Mn-Fe-P [7], which show a discontinuous change in lattice constants (with a small volume change). For MCE materials with an order-disorder transition, a large thermal or magnetic hysteresis can occur, which is detrimental for cyclic magnetocaloric applications. On the other hand, order-order transitions, such as an antiferro-to-ferromagnetic [5] or antiferro-to-ferrimagnetic (AFM-FIM) transition [8] can also present large magnetic entropy change with discontinuous lattice constants. These materials are easier to achieve almost free of hysteresis and a high sensitivity of the magnetization with temperature [3, 8].

In Mn_2Sb-based alloys an AFM-FIM order-order transition has been reported. The Mn_2Sb-based compound is an intermetallic compound, which is low cost, easy to prepare and nontoxic. The binary Mn_2Sb compound crystallizes in a tetragonal Cu_2Sb-type structure (space group *P4/nmm*) with a Curie temperature (T_C) of 550 K [9]. The magnetic moments are mainly attributed to the Mn atoms, which are positioned at two different crystallographic sites, Mn-I (2*a*) and Mn-II (2*c*), stacked antiparallel in triple layers. Neutron diffraction indicated that the Mn-I and Mn-II atoms possess magnetic moments of 2.1 and -3.9 μ_B, respectively [9]. The repeated stacking of Mn-II /Mn-I /Mn-II leads to the ferrimagnetic ordering below 550 K [10]. Upon cooling, the moments of Mn-I and Mn-II both reorient from being parallel to the *c* axis of tetragonal lattice into the *a-b* basal plane at a temperature of about 240 K, which has been identified as the spin reorientation temperature (T_{SR}). Upon further

cooling, a FIM-AFM transition has been reported in ternary compounds for substitution of Mn with Cu [11], Cr [8], Zn [12], Co [13] or for substitution of Sb with Ge [14], Sn [15], and As [16]. An overview of different substitutions in Mn_2Sb can be found in a recent review of Caron [17]. The reported AFM ordering shows an anti-parallel arrangement of adjacent Mn-II moments along the *a* axis [13]. The basic mechanism behind the AFM-FIM transition is based on the exchange inversion initially proposed by Kittel [18]. The reduced lattice constant *c* by the introduction of smaller atoms decreases the distance of adjacent Mn-II atoms, which triggers exchange inversion by the normal thermal contraction.

Interestingly, this AFM-FIM transition was also reported in larger atom Bi doped Mn_2Sb [19, 20]. Ohshima *et al.* [19] found a large magnetization jump around 100–140 K in $(Mn_2Sb)_{0.89}Bi_{0.11}$ and Zhang el al. [20] discussed the role of Bi-rich grain boundary precipitates (that were found to coat the main phase) on the magnetic transition. However, few studies focused on how Bi substitution for Sb influences the magnetic properties. Therefore, this paper aims to study the structure, magnetic properties and MCE in arc-melted $Mn_2Sb_{1-x}Bi_x$ (x = 0, 0.02, 0.04, 0.05, 0.07, 0.09, 0.15, 0.20) compounds.

4.2 Experimental methods

Polycrystalline $Mn_2Sb_{1-x}Bi_x$ (x = 0, 0.02, 0.04, 0.05, 0.07, 0.09, 0.15, 0.20) compounds were prepared from high purity elements (Mn 99.9%, Bi 99.99%, Sb 99.5%) by arc melting. Then the arc-melted samples were annealed for homogenization under argon atmosphere at 1073 K for 16 h followed by quenching into water. X-ray diffraction (XRD) data were collected with a Panalytical X-Pert PRO using Cu-Kα radiation and an Anton Paar TTK 450 temperature chamber. Lattice constants were analysed by Rietveld refinement using Fullprof (see Fig. S4.1 in the Supplementary Material) [21]. The microstructure was analysed by the Scanning Electron Microscopy (SEM, JEOL JSM IT100LA) equipped with the Energy Dispersive X-ray Spectroscopy (EDS). The low-temperature magnetic properties were measured on a superconducting quantum interference device

(SQUID) magnetometer model MPMS-XL, equipped with the reciprocating sample option. High-temperature magnetic measurements were carried out using a vibrating sample magnetometer (VSM) model LakeShore 7307 equipped with a high-temperature oven (model 73034). Magnetization-temperature (*M-T*) curves were conducted with zero-field cooled (ZFC), field heated (FH) and field cooled (FC) protocols. Due to the mixed magnetic states at low temperature, T_t is defined as the critical temperature with the maximal magnetization on the heating curve under a magnetic field of 1 T. T_{SR} and T_C are both obtained from the extremum positions on the temperature derivative of the heating curves under a magnetic field of 0.01 T. The magnetic entropy change was calculated from the *M-T* curves using the Maxwell relations.

First-principles electronic structure calculations were performed in the framework of the density functional theory (DFT). The Vienna ab initio simulation package (VASP) [22, 23] in the projector augmented wave (PAW) method [24, 25] was employed to perform the DFT calculations using the generalized gradient approximation of Perdew-Burke-Ernzerhof (PBE) [26] for the exchange correlation functional. The valence electron configuration was $3p^6 3d^5 4s^2$ for Mn, $5s^2 5p^3$ for Sb and $5d^{10} 6s^2 6p^3$ for Bi. All calculations were performed for a $1 \times 2 \times 1$ supercell. The structural degrees of freedom were fully relaxed on a gamma centered k-grid of $7 \times 7 \times 7$. The k-space integrations were performed with the Methfessel-Paxton method [27] of second order with a smearing width of 0.05 eV. The lattice parameters and atomic positions were relaxed for a force convergence of 0.1 meV/Å, while the energies were converged to 1 μeV. The kinetic energy cutoff was set at 520 eV.

To investigate the site preference two Bi atoms were placed on various possible combinations of the crystallographic sites. The energy cost of forming each structure is calculated as the difference between energies of Bi-doped (E_{doped}) and pure (E_{pure}) compounds minus chemical potential of two Bi atoms ($2\ \mu_{Bi}$) plus the chemical potential of the first atom *s1* and second atom *s2* that Bi substitutes for (μ_{s1} and μ_{s2}):

$$E_f = E_{doped} + \mu_{s1} + \mu_{s2} - \left(E_{pure} + 2\mu_{Bi}\right) \quad (1)$$

The chemical potentials are obtained by first optimizing the structure for each element (rhombohedral for Sb and Bi, cubic for Mn) and then taking the value of total energy per atom.

4.3 Results and discussion

The XRD data at room temperature in $Mn_2Sb_{1-x}Bi_x$ and the derived lattice parameters of the tetragonal lattice structure are shown in Fig. 4.1. The lattice parameters for the Mn_2Sb-based compound with $x = 0$ (a = 4.077 Å and c = 6.543 Å) are slightly lower than the ones reported in an earlier study (a = 4.078 Å and c = 6.557 Å) [28]. This small discrepancy can be due to deviations in the chemical composition caused by the occurrence of the typical impurity phase MnSb. As shown in Fig. 4.1(a), with the increase of the amount of Bi doping, additional secondary phases are detected besides the main phase of Cu_2Sb-type tetragonal Mn_2Sb. A minor impurity phase MnSb (about 5%) appears in samples with $x < 0.09$. The refined parameters and the fraction of the main impurity phase MnSb can be found in Tables S4.1 and S4.2 in the Supplementary Material. The chemical compositions of the main phase in the x = 0.05 and 0.07 samples are determined to be $Mn_{68.0}Sb_{29.6}Bi_{2.4}$ and $Mn_{66.5}Sb_{31.0}Bi_{2.5}$ by EDS, which are both close to their nominal compositions $Mn_{66.7}Sb_{31.7}Bi_{1.7}$ and $Mn_{66.7}Sb_{31.0}Bi_{2.3}$, respectively. The increasing values for the lattice parameters a and c and the unit-cell volume V with increasing Bi concentration in Fig. 4.1(b) and Fig. 4.1(c) confirm the inclusion of Bi in the Mn_2Sb matrix. This trend is opposite to the reduced unit-cell volume observed in Mn_2Sb-based compounds with smaller atom substitutions such as Cr replacing Mn [8] or Sn replacing Sb [15]. The opposite trend of lattice parameters between our results and Zhang *et al.* [20] could be attributed to the different fractions of MnSb and occupation of Bi in Mn_2Sb. Further Bi doping ($x >$ 0.09) induces multiple secondary phases: hexagonal (*P63/mmc* symmetry) MnBi, rhombohedral (*R-3m* symmetry) Bi and cubic (*I-43m* symmetry) Mn. The insignificant evolution of the main-phase lattice parameters and unit-cell volume beyond 9% Bi concentration and the appearance of the secondary phase Bi in $x = 0.09$ suggest a solid solubility limit 7%~ 9% of Bi in the Mn_2Sb matrix phase. The

proposed solubility limit of Bi in Mn_2Sb has been indicated in Fig. 4.2(d) as the turning point in c/a at x = 0.09. The decrease in lattice parameters a and c and unit-cell volume V for x = 0.20 is attributed to deviations in the chemical composition caused by the formation of Bi-rich impurity phases.

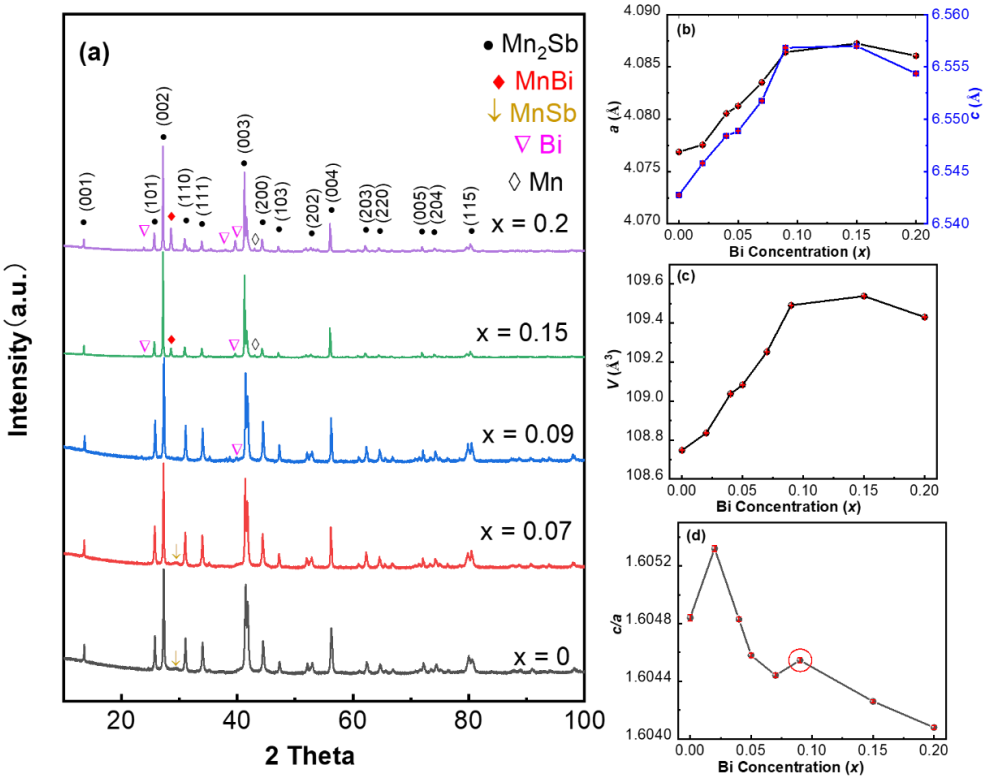

Fig. 4.1. (a) XRD patterns. for clarity of presentation, the patterns for x = 0.02, 0.04 and 0.05 are omitted because of their close similarity to the patterns for x = 0 and 0.07. (b) Lattice parameters a and c, (c) unit-cell volume V, (d) the ratio of c/a derived from XRD as a function of the Bi concentration for $Mn_2Sb_{1-x}Bi_x$ (x = 0, 0.02, 0.04, 0.05, 0.07, 0.09, 0.15, 0.20). The red circle marks the turning point of c/a at x = 0.09.

The temperature dependent magnetization curves are shown in Fig. 4.2(a, b) for x = 0.05. The weak splitting of the ZFC and FC curves under a field of 0.01 T in Fig. 4.2(a) is expected to be due to the presence of the ferromagnetic (FM) impurity phase MnSb [29], which is in agreement with the XRD results. Starting at the lowest

temperature with increasing temperature, the ZFC curve runs from a low value in the AFM state with spins in the *a-b* plane up to a temperature of about 150 K, where the magnetic transition temperature T_t of AFM-FIM is approached and a high spin alignment is observed. Then the magnetization drops dramatically at about 260 K, where the spins flip parallel along the *c* axis. This phenomenon has been reported for $(Mn_2Sb)_{0.89}Bi_{0.11}$ [19, 20], and has been attributed to the spin-reorientation effect. The spin-flip transition process in the FC curve is fuzzier than in the FH and ZFC curves, which indicates that thermal history affects the spin orientation [13]. This feature smears out under stronger magnetic field, suggesting that the magneto-crystalline anisotropy is overcome by the Zeeman energy provided by the magnetic field of 1 T [30]. The spin-orientation effect could be responsible for the larger thermal hysteresis of *M-T* curves for a field of 0.01 T compared to 1T in Fig. 4.2(b).

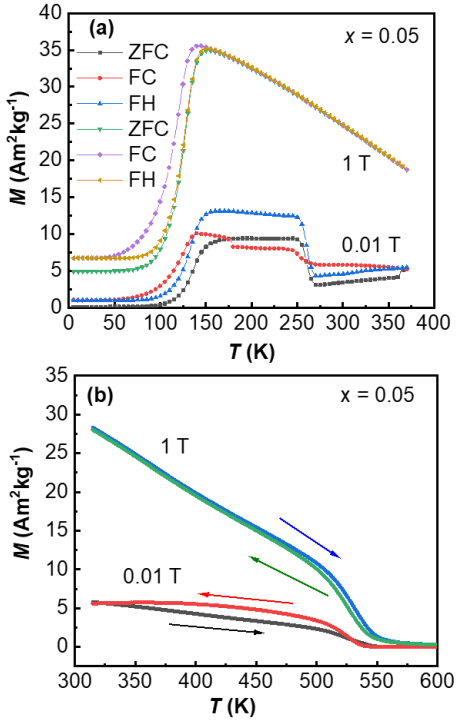

Fig. 4.2. (a) *M-T* curves for $Mn_2Sb_{1-x}Bi_x$ with $x = 0.05$ under magnetic fields of 0.01 and 1 T for a temperature range of 5 - 370 K and (b) for a temperature range of 315 - 600 K.

Fig. 4.3(a) and 4.3(b) display the *M-T* curves of $Mn_2Sb_{1-x}Bi_x$ (x = 0, 0.02, 0.04, 0.05, 0.07, 0.09, 0.15, 0.20) under magnetic fields of 0.01 T and 1 T, respectively. Compared with other Bi substituted Mn_2Sb compounds, the larger splitting of ZFC and FC curves in x =0.02 is ascribed to the combined effects of the FM impurity phase MnSb and the incomplete FIM-AFM transition [20]. In Fig. 4.3(b), the magnetization of pure Mn_2Sb monotonically increases with decreasing temperature, while the magnetization of Bi-containing samples initially increases, then abruptly drops at a certain temperature, reaches a minimum and finally increases slowly with decreasing temperature. The saturation magnetization of pure Mn_2Sb is 40 Am^2/kg excluding 5 Am^2/kg from the MnSb impurity phase (estimated from the XRD data), which is in agreement with earlier studies [29, 31]. It is evident that partial substitution of Sb by Bi causes the AFM-FIM transition at T_t.

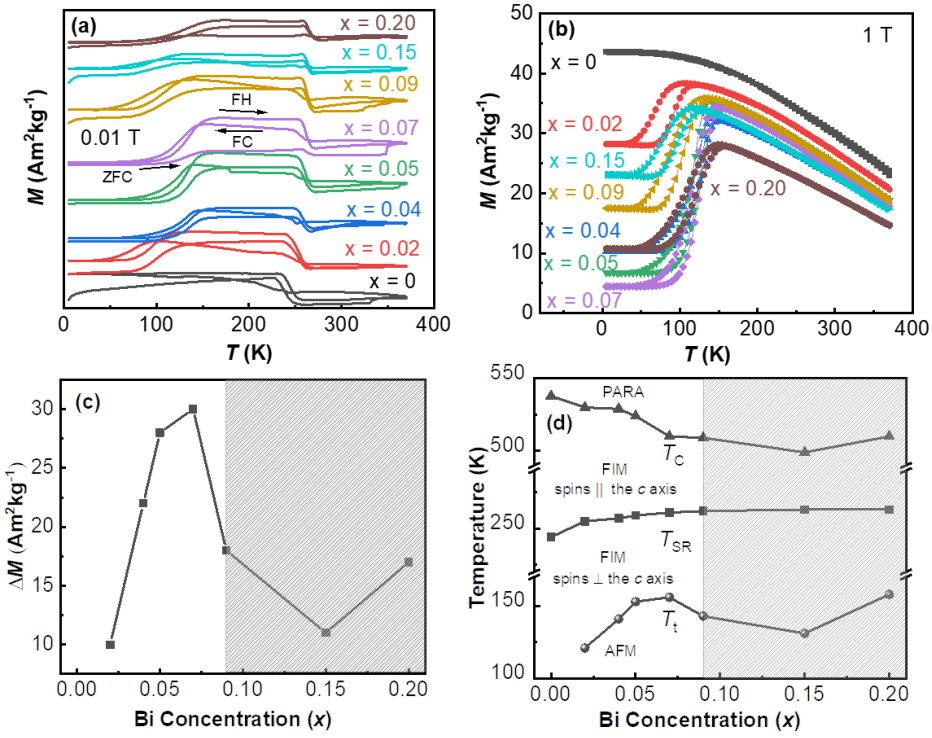

Fig. 4.3. (a) The temperature dependence of magnetization for $Mn_2Sb_{1-x}Bi_x$ (x = 0, 0.02, 0.04, 0.05, 0.07, 0.09, 0.15, 0.20) under a magnetic field of 0.01 T and (b) under

a magnetic field of 1 T. (c) The maximal magnetization jump ΔM at the AFM-FIM transition obtained from heating curves under 1 T as the function of the Bi concentration. (d) Magnetic phase diagram of $Mn_2Sb_{1-x}Bi_x$. The hatched area refers to the range beyond the solubility limit for Bi.

Fig. 4.3(c) and 3(d) summarize the magnetization jump ΔM at the AFM-FIM transition, together with T_t, T_{SR} and T_C derived from the *M-T* curves (the definitions of these critical temperatures are given in the experimental section 4.2). The hatched area refers to the concentration range beyond Bi solubility limit. ΔM first increases with increasing Bi concentration when $x \leq 0.09$ because a large amount of Bi triggers a larger fraction of the FIM-AFM transition, which decreases the residual FIM at the AFM region. Then ΔM decreases with further Bi addition because the fraction of secondary phases increases and as the main secondary phase MnBi is ferromagnetic below 633 K, this increases the magnetization in the AFM region. The maximal ΔM (30 Am^2/kg) and the highest T_t (156 K) are both found for $x = 0.07$, beyond which Bi as one of the secondary phases appears.

According to the magnetic phase diagram for $Mn_2Sb_{(1-x)}Bi_x$ in Fig. 4.3(d), T_{SR} rises slowly for increasing Bi concentration (starting from 255 K for $x = 0.02$ and saturating at 262 K for $x = 0.09$). This trend is in line with Co substitution in Mn_2Sb [13]. T_t as the function of Bi concentration shows a comparable trend as ΔM. For increasing Bi concentration, the AFM exchange interaction between the Mn-II and Mn-II moments becomes stronger as a result of the decrease in the *c/a* ratio in Fig. 4.1(d), which shifts the transition to higher temperatures [32]. T_C decreases linearly with Bi concentration. The slope of the fitting curve is about -2.66 K/T within the Bi solubility limit. The T_C of pure Mn_2Sb is 538 K, which is somewhat below the 550 K reported by Wilkinson et al. [9], and this is probably associated with slightly lower lattice parameters. The deviation observed for T_t and T_C at $x = 0.20$ is attributed to the abnormal lattice parameters of main phase, caused by excess secondary phases (about 20% MnBi and about 10% Bi). Compared with $(Mn,Cr)_2Sb$ [8], a narrower

temperature window for T_t (121–156 K) and T_C (538 - 509 K) is presented by Bi substitution, which is probably due to larger atom size of Bi.

The magnetocaloric effect of the $Mn_2Sb_{1-x}Bi_x$ compounds has been studied by measuring isofield magnetization and subsequent application of Maxwell relations [33]. In Fig. 4.4(a) the *M-T* curves are shown for x = 0.05 upon heating in magnetic fields ranging from 0.2 to 5 T. The magnetization shows a clear jump at T_t under all magnetic fields. T_t shifts to lower temperature with increasing field as the magnetic field favours the high-temperature high-magnetization FIM state. The size of the shift in transition temperature with magnetic field is estimated to be $dT_t/d\mu_0 H$ = -5.4 K/T from the data in Fig. 4.4(b). This value is higher than the reported value of -4.3 K/T for $Mn_{1.92}Cr_{0.08}Sb$ [8]. Since the magnetic field shifts the transition temperature to a lower temperature, which is different from the conventional MCE, the magnetocaloric effect for $Mn_2Sb_{1-x}Bi_x$ corresponds to the inverse MCE. The magnetic entropy change for the compound with x = 0.05 is shown in Fig. 4.4(c) and 4.4(d) for the heating and cooling curves, respectively. The magnetic entropy change is calculated based on the integrated Maxwell relation: $\Delta S(\Delta H, T) = \int_{H_0}^{H} \left(\frac{\partial M(T,H)}{\partial T}\right)_H d\mu_0 H$, where we choose $\mu_0 H_0$ = 0 T. The maximum entropy change under a field change of 5 T in the heating curves is 2.44 J/kgK at 116 K whereas in the cooling curves it is 1.91 J/kgK at 105 K. The maximum entropy change (2.44 J/kgK) is similar to the reported value of 1.97 J/kgK for $(Mn_2Sb)_{0.93}Bi_{0.07}$ by measuring isothermal field-up magnetization [20]. The temperature window for the latter (74 K) is wider than for the former (53 K). The difference in magnetic entropy change between heating and cooling is attributed to large thermal hysteresis of about 10 K, as shown in Fig. 4.2(a).

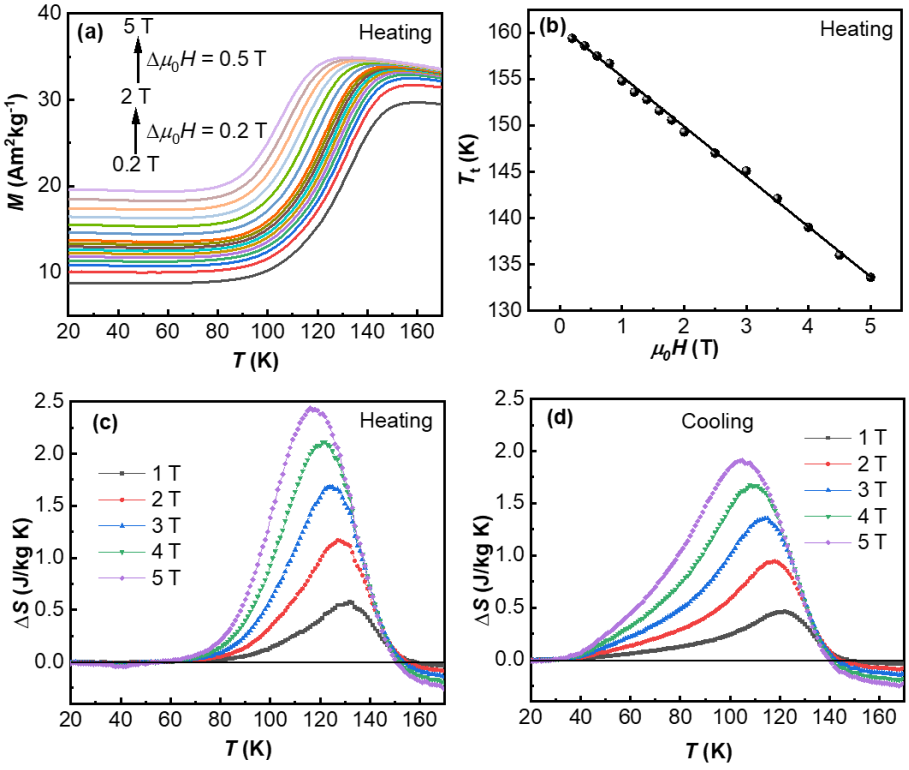

Fig. 4.4. (a) *M-T* curves for $Mn_2Sb_{(1-x)}Bi_x$ with $x = 0.05$ for heating in different applied magnetic fields. (b) T_t as a function of magnetic field. The magnetic entropy change ΔS calculated from the (c) heating curves and (d) cooling curves.

In order to know what position the Bi atoms prefer to occupy in the Mn_2Sb lattice, we employed spin-polarized DFT calculations for the formation energy, magnetic moment, lattice constants a and c and unit-cell volume V for a Bi concentration of $x = 0.04$. The results are summarized in Table 4.1. The calculated magnetic moments (2.3 μ_B for Mn-I and -3.4μ_B for Mn-II) for pure Mn_2Sb are in agreement with published data (2.13 μ_B for Mn-I and -3.87μ_B for Mn-II) measured by neutron diffraction [9]. The calculated lattice constants (a = 3.94 Å and c = 6.44 Å) are comparable with those derived from XRD. Among all studied configurations we find the lowest formation energy (also the closest cell volume and lattice constants to pure Mn_2Sb) when the Bi atoms solely occupy the Sb site. Given the low Bi concentrations involved, this result for $x = 0.04$ is expected to be representative for

all the studied samples up to the solubility limit ($x < 0.09$). The substitution of the non-magnetic Sb atoms by Bi atoms leads to a decrease in the atomic magnetic moment for Mn-I and an increase for Mn-II. A comparable magnetization is expected when Bi preferentially replaces non-magnetic Sb. This agrees with the following experimental results: the magnetization jump at the AFM-FIM is according to Fig. 4.2(a) equal to 12 Am^2/kg under a field of 0.01 T, which is larger than the 4 Am^2/kg for $Mn_{2-x}Cr_xSb$ compounds under a field of 0.02 T [8], where the Cr atoms occupy the Mn-I site [34].

Table 4.1 Volume V, lattice constants a and c, formation energy E_f, magnetic moment on the constituent atoms Mn-I and Mn-II per formula unit of $Mn_2Sb_{0.96}Bi_{0.04}$.

Occ (Bi)	E_f (eV)	Mn-I (μ_B)	Mn-II (μ_B)	V (Å^3)	a (Å)	c (Å)
Mn-I	0.69	3.0	-3.5	113.7	3.90	7.15
Mn-I Mn-II	0.51	2.8	-3.4	116.8	4.16	6.55
Mn-I Sb	0.54	2.7	-3.5	109.6	4.01	6.81
Mn-II	0.26	2.9	-3.8	118.0	4.26	6.51
Mn-II Sb	-0.21	2.4	-3.6	108.2	4.08	6.51
Sb	-0.47	1.9	-3.5	101.7	4.00	6.37
None	-1.38	2.3	-3.4	99.9	3.94	6.44

The exchange inversion proposed by Kittel [18] was initially used to describe the AFM-FIM transition in $Mn_{2-x}Cr_xSb$. The sign of the exchange interaction will

change when the lattice parameters go across a critical value at the critical temperature. This can occur as a result of the normal expansion or contraction of the materials with temperature. For pure Mn_2Sb, the normal thermal contraction is not sufficient to trigger the exchange inversion, but the exchange inversion becomes accessible with the help of chemical compression [15] by substitution with smaller atoms such as Cr replacing Mn [8], Sn replacing Sb [15]. Besides, the critical temperature could be reached by the enhanced coefficient of thermal expansion along the *c* axis, which affects the temperature dependent interatomic distances. As a larger Mn-Mn interatomic distance for Bi substituted Mn_2Sb is inferred from the larger lattice parameters at room temperature, the origin of the AFM-FIM transition in $Mn_2Sb_{1-x}Bi_x$ is ascribed to an enhancement of the coefficient of thermal expansion along the *c* axis by Bi substitution [35]. To verify this assumption, the thermal expansion coefficient was investigated in $x = 0.07$ by variable temperature XRD in the temperature range of 298–698 K. The coefficient for $x = 0.07$ ($x = 0.05$) are 2.0×10^{-5} K^{-1} (1.9×10^{-5} K^{-1}) along the *c* axis at room temperature, which is higher than the value (1.4×10^{-5} K^{-1}) in Mn_2Sb reported by Heaton et al. [28]. The counterpart along the *a* axis is 2.3×10^{-5} K^{-1} (2.2×10^{-5} K^{-1}), which is lower than the values (4.0×10^{-5} K^{-1}) reported by Heaton et al. [28]. Bi substitution thus affects the environment around the Mn atoms and stabilizes antiferromagnetism [16].

4.4 Conclusions

In summary, the structure and magnetic properties of $Mn_2Sb_{1-x}Bi_x$ ($x = 0$, 0.02, 0.04, 0.05, 0.07, 0.09, 0.15, 0.20) have been investigated. It is observed that Bi substitution for Sb causes an increase in lattice parameters, a large magnetization jump identified as the AFM-FIM transition and an impressive magnetic field dependence of transition temperature of $dT_t/d\mu_0H = -5.4$ K/T. The transition temperature and magnetization jump both increase with increasing Bi concentration up to a value of $x = 0.07$, which is found to be the solubility limit of Bi. The exchange inversion in $Mn_2Sb_{1-x}Bi_x$ caused by the substitution with a larger atom is ascribed to the enhanced coefficient of

thermal expansion along the *c* axis, the stacking direction of the Mn-I and Mn-II layers.

References

[1] O. Gutfleisch, M.A. Willard, E. Brück, C.H. Chen, S.G. Sankar, J.P. Liu, Magnetic materials and devices for the 21st century: stronger, lighter, and more energy efficient, Adv. Mater. 23 (2011) 821.

[2] S.M. Sandoval, K.P. Wetzlar, G.P. Carman, Thermomagnetic conversion efficiencies for ferromagnetic materials, J. Appl. Phys. 110 (2011) 123923.

[3] V. K. Pecharsky, K. A. Gschneidner, Giant Magnetocaloric Effect in $Gd_5Si_2Ge_2$, Phys. Rev. Lett. 78 (1997) 4494.

[4] H. Wada, Y. Tanabe, Giant magnetocaloric effect of $MnAs_{1-x}Sb_x$, Appl. Phys. Lett. 79 (2001) 3302-3304.

[5] T. Krenke, E. Duman, M. Acet, E.F. Wassermann, X. Moya, L. Manosa, A. Planes, Inverse magnetocaloric effect in ferromagnetic Ni-Mn-Sn alloys, Nat. Mater. 4 (2005) 450.

[6] F. Hu, B. Shen, J. Sun, Z. Cheng, G. Rao, X. Zhang, Influence of negative lattice expansion and metamagnetic transition on magnetic entropy change in the compound $LaFe_{11.4}Si_{1.6}$, Appl. Phys. Lett. 78 (2001) 3675-3677.

[7] O. Tegus, E. Brück, K.H.J. Buschow, F.R. Boer, Transition-metal-based magnetic refrigerants for room-temperature applications, Nature, 415 (2002) 150-152.

[8] L. Caron, X. Miao, J.C.P. Klaasse, S. Gama, E. Brück, Tuning the giant inverse magnetocaloric effect in $Mn_{2-x}Cr_xSb$ compounds, Appl. Phys. Lett. 103 (2013) 112404.

[9] M. K. Wilkinson, N. S. Gingrich, C. G. Shull, The magnetic structure of Mn_2Sb, J. Phys. Chem. Solids 2 (1957) 289-300.

[10] W.H. Cloud, H.S. Jarrett, A.E. Austin, E. Adelson, Neutron diffraction studies of chromium-modified Mn_2Sb, Phys. Rev. 120 (1960) 1969-1970.

[11] W. Cui, W. Ren, Z. Zhang, X. Zhou, H. Zhong, Q. Wang, Lattice distortion tuning of the metamagnetic phase transition in tetragonal Cu_2Sb-type $Mn_{1.95}V_{0.05}Sb$ alloy, Scr. Mater. 143 (2018) 59-62.

[12] S. Ohta, Y. Hasebe, T. Kanomata, T. Kanek, Thermal expansion and magnetic properties of $Mn_{2-x}Zn_xSb$, J. Magn. Magn. Mater. 104 (1992) 1979-1980.

[13] J. Wilden, A. Hoser, M. Chikovani, J. Perßon, J. Voigt, K. Friese, A. Grzechnik, Magnetic Transitions in the Co-Modified Mn_2Sb System, Inorganics 6 (2018) 113.

[14] J. Zhang, G. Yao, S. Chen, F. Wei, X. Fan, X. Yin, Z. Chen, W. Cui, Q. Wang, The effects of Ge occupation and hydrostatic pressure on the metamagnetic phase transition and magnetocaloric effect, AIP Adv. 9 (2019) 035106.

[15] V.M. Ryzhkovskii, V. P. Dymont, Z.L. Erofeen, Effect of high-pressure high-temperature processing on the phase composition and magnetic state of $Mn_{1+x}Sb$ ($0 \leq x \leq 1.0$) alloys, Phys. Stat. Sol. A 130 (1992) 163-168.

[16] T. Kakimoto, J. Goto, S. Fujii, K. Koyama, S. Ishida, Electronic and Magnetic Properties of $Mn_2Sb_{1-x}As_x$ (x = 0, 0.5, 1), Mater. Trans. 55 (2014) 1878-1884.

[17] L. Caron, Chapter 3, Handbook of Magnetic Materials, vol. 29, first ed., Elsevier (2020).

[18] C. Kittel, Model of Exchange-Inversion Magnetization, Phys. Rev. 120 (1960) 335-342.

[19] S. Ohshima, K. Fukamichi, T. Wakiyama, T. Anayama, Magnetic First-Order Phase Transition in Bi Modified Mn_2Sb, Jpn. J. Appl. Phys. 18 (1979) 707.

[20] Z. Zhang, Y. Zhang, X. Luo, S. Ma, H. Zeng, G. Yu, X. Zheng, C. Chen, Y. Hu, F. Xu, S.U. Rehman, Z. Zhong, Self-organized Bi-rich grain boundary precipitates for realizing steep magnetic-field-driven metamagnetic transition in Bi-doped Mn_2Sb, Acta Mater. 200 (2020) 835-847.

[21] B. H. Toby, R factors in Rietveld analysis: How good is good enough? Powder Diffr. 21 (2006) 67-70.

[22] G. Kresse, J. Hafner, Ab initio molecular dynamics for liquid metals, Phys. Rev. B 47 (1993) 558.

[23] G. Kresse, J. Furthmüller, Efficiency of ab-initio total energy calculations for metals and semiconductors using a plane-wave basis set, Comput. Mater. Sci. 6 (1996) 15-50.

[24] P.E. Blöchl, Phys. Rev. B 50 (1994) 17953.

[25] G. Kresse, D. Joubert, Projector augmented-wave method, Phys. Rev. B 59 (1999) 1758.

[26] J.P. Perdew, K. Burke, M. Ernzerhof, Generalized Gradient Approximation Made Simple, Phys. Rev. Lett. 77 (1996) 3865.

[27] M. Methfessel, A.T. Paxton, High-precision sampling for Brillouin-zone integration in metals, Phys. Rev. B 40 (1989) 3616.

[28] L. Heaton, N.S. Gingrich, The Crystal Structure of Mn_2Sb, Acta Cryst. 8 (1955) 207-210.

[29] A. Tekgül, Ö. Çakır, M. Acet, M. Farle, N. Ünal, J. Appl. Phys. 118 (2015) 153903.

[30] Y. Cao, K. Xu, Z. Li, Y. Zhang, X. He, Y. Kang, W. Sun, T. Gao, Z. Qian, C. Liu, M. Ye, C. Jing, Interplay between spin reorientation and magnetoelastic transitions, and anisotropic magnetostriction in the $Mn_{1.95}Cr_{0.05}Sb$ single crystal, J. Magn. Magn. Mater. 487 (2019) 165315.

[31] F.J. Darnell, W.H. Cloud, H.S. Jarrett, X-Ray and Magnetization Studies of Cr-Modified Mn_2Sb, Phys. Rev. 130 (1963) 647-655.

[32] Y. Zhang, Z. Zhang, Metamagnetic-transition-induced giant magnetoresistance in $Mn_2Sb_{1-x}Sn_x$ ($0 < x \leq 0.4$) compounds, Phys. Rev. B 67 (2003) 132405.

[33] L. Caron, Z. Ou, T.T. Nguyen, D.T. Cam Thanh, O. Tegus, E. Brück, magnetic entropy change in materials with first-order transitions, J. Magn. Magn. Mater. 321 (2009) 3559-3566.

[34] A.E. Austin, E. Adelson, W.H. Cloud, Magnetic Structures of Chromium-Modified Mn_2Sb, Phys. Rev. 131 (1963) 1511-1517.

[35] K. Shirakawa, H. Ido, magnetic transition of intermetallic compounds $Mn_2Sb_{1-x}Bix$ ($0 \leq x \leq 0.175$) with Cu_2Sb type structure, J. Japan Inst. Metals 43 (1979) 636.

Supplementary Material for Chapter 4

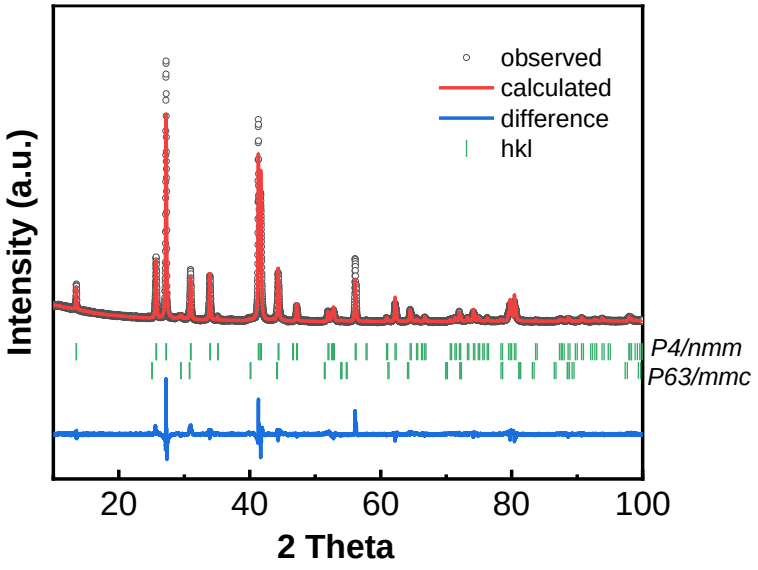

Fig. S4.1. Rietveld refinement of the XRD pattern of $Mn_2Sb_{1-x}Bi_x$ for $x = 0.07$ at room temperature (*Rp*: 3.81%, *Rwp*: 5.99%). The bottom blue line shows the difference between the observed and calculated intensities and the green vertical short lines from top to bottom denote the Bragg peak positions for the Mn_2Sb (*P4/nmm*) and MnSb (*P63/mmc*) structures.

Table S4.1. Rietveld refinement of the XRD data for the in $Mn_2Sb_{1-x}Bi_x$ (x = 0, 0.02, 0.04, 0.05, 0.07). The Mn_2Sb-type main phase has a *P4/nmm* tetragonal symmetry with two formula units per unit cell (Z = 2) and three occupied crystallographic positions at sites *2a* (3/4, 1/4, 0), *2c*$_1$ (1/4, 1/4, z_1) and *2c*$_2$ (1/4, 1/4, z_2). Listed are the parameters *a* and *c*, the internal coordinates for the *2c* sites (z_1 and z_2), the site occupations of Sb, Bi (at *2c*$_2$ site) and the quality of fit (R_p/R_{wp} and χ^2).

x	0	0.02	0.04	0.05	0.07
a	4.07689(4)	4.07756(4)	4.08056(3)	4.08127(3)	4.08352(3)
c	6.54276(7)	6.54579(5)	6.54840(5)	6.54889(5)	6.55177(5)
z_1	0.29881(39)	0.30060(38)	0.29921(32)	0.29833(15)	0.29936(33)
z_2	0.71669(17)	0.71669(16)	0.71595(14)	0.71564(12)	0.71561(15)
Occ(Sb)	0.125	0.124	0.124	0.119	0.116
Occ(Bi)	--	0.001	0.001	0.004	0.007
R_p/R_{wp}	4.33/6.88	4.50/7.18	5.30/7.91	4.44/6.57	3.81/5.99
χ^2	10.20	12.40	9.87	10.10	7.73

Table S4.2. Lattice parameters *a* and *c*, *c/a* ratio and the unit-cell volume *V* for the Mn_2Sb type main phase together with the fraction of the MnSb secondary phase based on Rietveld refinement of the XRD data for $Mn_2Sb_{1-x}Bi_x$ (x = 0, 0.02, 0.04, 0.05, 0.07, 0.09, 0.15, 0.20).

x	*a* (Å)	*c* (Å)	*c/a*	*V* (Å^3)	Fraction of MnSb (*wt.*%)
0.00	4.07689(4)	6.54276(7)	1.60484(2)	108.747(2)	5.4
0.02	4.07756(4)	6.54579(5)	1.60532(2)	108.836(2)	6.8
0.04	4.08056(3)	6.54840(5)	1.60483(2)	109.037(2)	4.6
0.05	4.08127(3)	6.54889(5)	1.60458(2)	109.083(1)	4.2
0.07	4.08352(3)	6.55177(5)	1.60444(2)	109.252(1)	5.2
0.09	4.08641(3)	6.55683(5)	1.60455(2)	109.491(1)	--
0.15	4.08724(2)	6.55700(2)	1.60426(1)	109.538(1)	--
0.20	4.08606(2)	6.55437(5)	1.60408(1)	109.43(2)	--

Chapter 5 Magnetoelastic transition and negative thermal expansion of $Fe_2Hf_{0.83}Ta_{0.17}$ ribbons

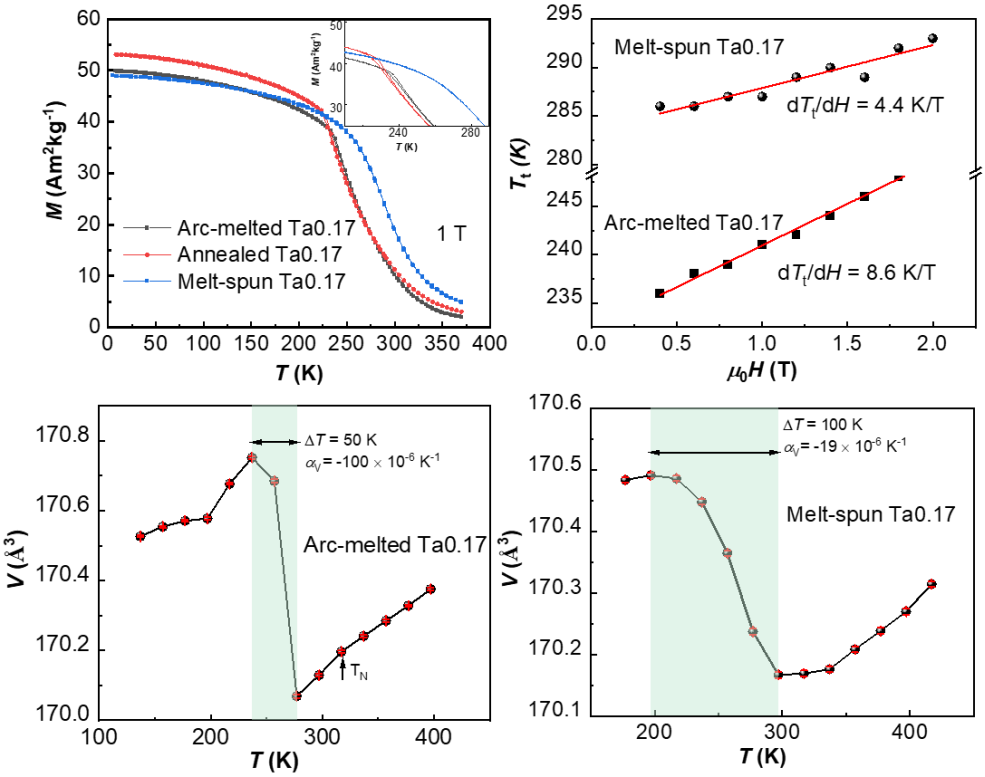

This chapter is based on:

Q. Shen, F. Zhang, I. Dugulan, N. van Dijk, E. Brück, Magnetoelastic transition and negative thermal expansion of $Fe_2Hf_{0.83}Ta_{0.17}$ ribbons, Scr. Mater. 232 (2023) 115482.

Abstract

In this work, the magnetocaloric effect and negative thermal expansion in melt-spun $Fe_2Hf_{0.83}Ta_{0.17}$ Laves phase alloys were studied. Compared to arc-melted alloys, which undergo a first-order magnetoelastic transition from the ferromagnetic to the antiferromagnetic phase, melt-spun alloys exhibit a second-order transition. For $Fe_2Hf_{0.83}Ta_{0.17}$ ribbons, we observed a large volumetric coefficient of negative thermal expansion of -19×10^{-6} K^{-1} over a wide temperature range of 197–297 K and a moderate adiabatic temperature change of 0.7 K at 290 K for a magnetic field change of 1.5 T. The magnetic field dependence of the transition temperature ($dT_t/d\mu_0H$ = 4.4 K/T) for the melt-spun alloy is about half of that for the arc-melted alloy (8.6 K/T). The origin of the second-order phase transition of the melt-spun alloy is attributed to the partially suppressed frustration effect, which is due to the atomic disorder introduced by the rapid solidification.

5.1 Introduction

The magnetocaloric effect (MCE) is the caloric response to an external magnetic field, characterised in terms of the adiabatic temperature change (ΔT_{ad}) and the isothermal entropy change (ΔS_m) as performance indices [1, 2]. Due to its potentially higher energy efficiency and environmental friendliness compared to vapor compression refrigeration, MCE-based cooling has received considerable attention [3, 4]. $Fe_2Hf_{1-x}Ta_x$ Laves phase materials, as one of the promising MCE candidate systems, has attracted particular interest by the itinerant-electron metamagnetic transition from the ferromagnetic (FM) to the antiferromagnetic (AFM) and then to the paramagnetic (PM) state with increasing temperature at x = 0.16–0.22 [5, 6]. These compounds crystallize in the hexagonal C14 structure with Fe atoms at two different sites, the 2*a* site and the 6*h* site, and Hf/Ta atoms at the 4*f* site [7, 8]. The sharp FM-to-AFM transition is attributed to the fact that the magnetic moments of Fe at the 2*a* site are frustrated in the AFM state because they lie in the middle between two antiferromagnetically coupled planes [8]. Due to the relatively low heat capacity and frustration effect, a large adiabatic temperature change (3.5 K) was observed for a magnetic field change of 2 T [6], which is comparable to the values for the two well-known MCE materials $La(Fe_{0.88}Si_{0.12})_{13}H_y$ [9] and $Mn_xFe_{2-x}P_{1-y}Si_y$ [10]. Accompanied by the magnetoelastic transition, a large negative thermal expansion effect is observed where the volume of the AFM phase is about 1% smaller than that of the FM phase [8].

The common fabrication method for $Fe_2(Hf,Ta)$ compounds is arc melting, followed by annealing at 1272 K for one week [11-13] or without further heat treatment [14, 15]. To the best of our knowledge, the melt-spinning technique has not been used to produce $Fe_2(Hf,Ta)$ alloys. However, this technique has been shown to improve magnetocaloric properties in the synthesize of various crystalline magnetocaloric materials such as $Mn_{0.66}Fe_{1.29}P_{1-x}Si_x$ [16], $La(Fe_{0.88}Co_{0.12})_{13}Si_x$ [17], $Gd_5(SiGeSn)_4$ [18] and $Ni_{50.3}Mn_{35.5}In_{14.4}$ [19] compared to bulk alloys. The high cooling rate during the solidification process promotes a more homogeneous element

distribution, reducing the amount of impurity phase and the annealing time [17, 20, 21]. Therefore, we have in this study investigated the MCE and the negative expansion effect in a melt-spun $Fe_2Hf_{0.93}Ta_{0.17}$ alloy and compared it to the arc-melted alloy with the same composition. We found that melt-spinning technique can be an effective method to tune the magnetic field dependence of the transition temperature and to broaden the temperature range for negative thermal expansion applications in Fe_2(Hf,Ta) Laves phase compounds.

5.2 Experimental methods

Polycrystalline $Fe_2Hf_{0.93}Ta_{0.17}$ compounds were prepared from high-purity elements (Fe 99.98%, Hf 99.7%, Ta 99.9%) by arc melting. To avoid excess Fe atoms occupying the Hf/Ta site, the iron concentration was kept about 0.5% lower than the stoichiometric amount [22, 23]. Samples with a total mass of 5 g were melted four or five times, and the button-shaped alloys were flipped over after each melting. The sample without heat treatment is referred to as 'arc-melted Ta0.17'. The sample annealed at 1273 K for one week and then quenched into water is noted as 'annealed Ta0.17'. The sample prepared by melt spinning is noted as 'melt-spun Ta0.17'. Since there is not much difference in the magnetic properties between the arc-melted and the annealed Ta0.17 alloys, the arc-melted sample without heat treatment is used for comparison with the melt-spun sample.

X-ray diffraction (XRD) data were collected with a Panalytical X-Pert PRO using Cu-K_α radiation and an Anton Paar TTK 450 temperature chamber. Lattice constants were analysed by Rietveld refinement using the Fullprof software [24]. The magnetic properties at low temperatures (4–370 K) were measured using a superconducting quantum interference device (SQUID) magnetometer model MPMS-XL, equipped with the reciprocating sample option. The ferromagnetic transition temperature T_C was determined from the temperature derivative of the magnetisation at a magnetic field of 1 T. The ΔS_m was calculated from *M-T* curves in different magnetic fields using the Maxwell relations. The ΔT_{ad} was derived from the

calorimetric measurements based on a home-made in-field DSC machine, details can be found in Refs. [25-27]. The microstructure was analysed by Scanning Electron Microscopy (SEM) using a FEI Quanta FEG 450 equipped with energy dispersive X-ray spectroscopy (EDS). Transmission ^{57}Fe Mössbauer spectra were recorded at different temperatures ranging from 4.2 to 300 K using conventional constant-acceleration or sinusoidal velocity spectrometers with a ^{57}Co(Rh) source. The velocity calibration was performed using an α-Fe foil at room temperature. The source and the absorbing samples were kept at the same temperature during cryogenic measurements. The Mössbauer spectra were fitted with the programme Mosswinn 4.0 [28].

5.3 Results and discussion

Fig. 5.1(a) and (b) show the refined XRD patterns of the arc-melted and melt-spun Ta0.17 alloys at room temperature. They crystallize in the same hexagonal C14 Laves phase structure (space group: $P6_3/mmc$). The refined pattern of the annealed sample is given in Fig. S5.1(a). The refined lattice parameters are summarized in Table S5.1. Comparing the XRD patterns of the arc-melted and melt-spun alloys, there is a distinct difference in the relative peak intensity of the three highest peaks, which can be attributed to the different occupation sites of Hf atoms. For the arc-melted Ta0.17, the Fe atoms are refined to locate at the 2*a* and the 6*h* sites and the Hf/Ta atoms at the 4*f* site. However, the pattern of the melt-spun sample can be fitted better by assuming that part of the Hf atoms are positioned at the 2*a* site ($\chi^2 = 5.13$) than by assuming that all the Hf atoms are at the 4*f* site ($\chi^2 = 7.43$), as shown in Fig. S5.1(b). This explains the larger volume of the melt-spun alloy (171.209 Å^3) compared to that (170.013 Å^3) of the arc-melted alloy due to the larger atomic size of the Hf atom (159 pm) than the Fe atom (126 pm). The occupation of part of the Hf atoms at the 2*a* site may be caused by the rapid solidification process of the melt-spinning technique. The homogeneity of arc-melted and melt-spun Ta0.17 is compared in SEM images with corresponding line scans (see Fig. 5.1(c-f)). The SEM images show that the two alloys generally exhibit a single-phase microstructure, although the line scans reveal

a compositional variation in about 5 at.%. The somewhat smaller compositional variation in the linear scan of the melt-spun alloy indicates a relatively better homogeneity of the melt-spun alloy compared to the arc-melted alloy.

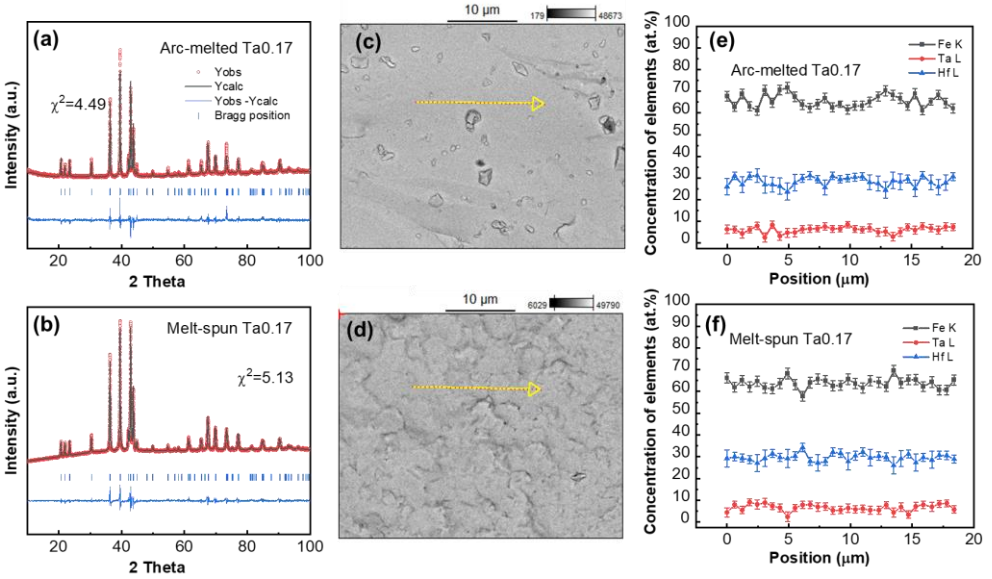

Fig. 5.1. Rietveld refinement results of the XRD patterns of (a) arc-melted Ta0.17 and (b) melt-spun Ta0.17. SEM images for (c) arc-melted Ta0.17 and (d) melt-spun Ta0.17. Line scan through the yellow line in (c-d) for (e) arc-melted Ta0.17 and (f) melt-spun Ta0.17.

The magnetic properties of arc-melted, annealed and melt-spun samples were investigated by measuring the *M*-*T* curves in an applied magnetic field of 1 T and the *M*-$\mu_0 H$ curves at 5 K. For arc-melted and annealed Ta0.17 alloys, a change in magnetization (T_t = 240 K for the arc-melted alloy and T_t = 231 K for the annealed alloy) corresponds to a magnetic transition with about 2 K thermal hysteresis. The transition is indicated by a weak *S*-shape for the Arrott-plot in Fig. S5.2(a) as a first-order transition from the low-temperature FM phase to the high-temperature AFM phase. For the melt-spun alloy, a transition without thermal hysteresis is suggested as a second-order transition (T_t = 286 K) by the absence of a negative slope for the

Arrott-plot in Fig. S5.2(b). The saturation magnetizations of annealed Ta0.17 and melt-spun Ta0.17 are both 52.6 Am^2/kg, while that of arc-melted Ta0.17 is 51.6 Am^2/kg. Compared to the arc-melted alloy, the melt-spun alloy exhibits a 46 K higher transition temperature and a slightly higher magnetic anisotropy, which can be attributed to the internal stress introduced during the melt-spinning process [29].

Fig. 5.2(c) and (d) show the Mössbauer spectra of arc-melted and melt-spun Ta0.17 at 4.2 K and 300 K, respectively. The fitting of the spectra is based on the crystal structure analysis, where Fe has two distinct sites, the 2*a* and 6*h* sites, with an atom ratio of 1: 3. At 400 K, a typical paramagnetic doublet phase is seen for both alloys (Fig. S5.3). The fitted Mössbauer data are summarized in Table 5.1. The similar values of the isomer shift and the quadrupole splitting of both alloys indicate a similar chemical environment for the 2*a* and the 6*h* sites. At 4.2 K, four sextets with the same area are assigned to one 2*a* site and three 6*h* sites due to the different reorientation of the spin directions with respect to the principle axis of the electric field gradient [12]. From Table 5.1, the hyperfine fields of the 2*a* site and the average 6*h* site for the melt-spun alloy are slightly larger than those of the arc-melted alloy, which is consistent with the slightly higher saturation magnetization of the melt-spun alloy. This can be related to the larger unit-cell volume for the melt-spun Ta0.17 alloy than the arc-melted Ta0.17 alloy [11]. At 300 K, the arc-melted Ta0.17 alloy is in the AFM state (with no magnetic moment at the 2*a* site and a small hyperfine field at the 6*h* site), while the melt-spun Ta0.17 alloy shows a coexistence of a relaxation phase and the AFM phase.

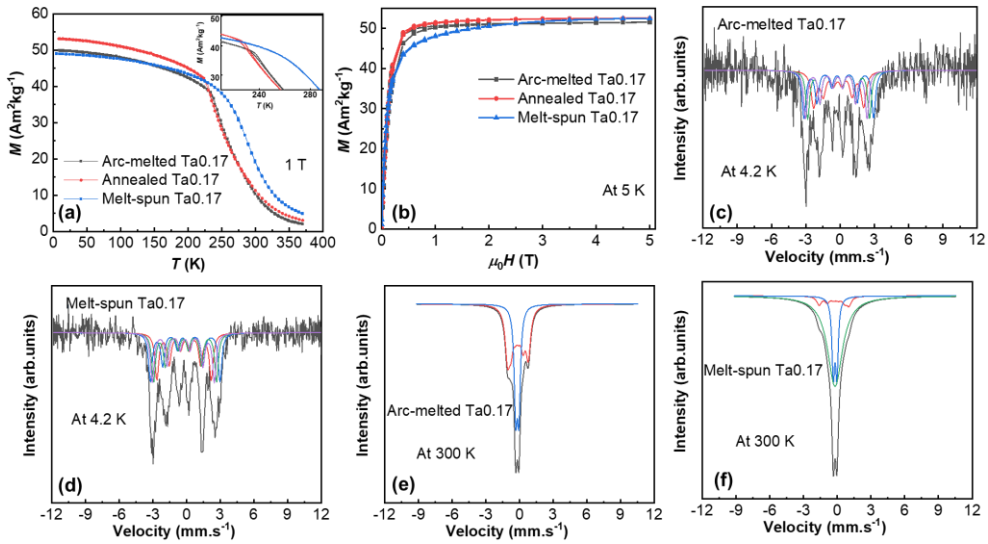

Fig. 5.2. (a) *M-T* curves in a magnetic field of 1 T. (b) *M-*$\mu_0 H$ curves at 5 K. Mössbauer spectra at 4.2 K for (c) arc-melted Ta0.17 and (d) melt-spun Ta0.17. Mössbauer spectra at 300 K for (e) arc-melted Ta0.17 and (e) melt-spun Ta0.17.

Table 5.1. Mössbauer fitted parameters of the arc-melted and melt-spun Ta0.17 alloys, obtained at different temperatures. Experimental uncertainties: Isomer shift: I.S. ± 0.03 mm s^{-1}; Quadrupole splitting: Q.S. ± 0.03 mm s^{-1}; Line width: Γ ± 0.05 mm s^{-1}; Hyperfine field: ± 0.2 T; Spectral contribution: ± 3%.

Sample	T (K)	IS (mm s^{-1})	QS (mm s^{-1})	Hyperfine field (T)	Γ (mm s^{-1})	Phase
Arc-melted Ta0.17	400	-0.34	0.36	--	0.35	100% (PM)
	4.2	-0.16	0.09	13.6	0.53	25.03% (2*a*)
		-0.18	0.16	19.0	0.39	24.99% (6*h*)
		-0.16	0.07	16.8	0.39	24.99% (6*h*)
		-0.26	-0.12	16.8	0.39	24.99% (6*h*)
	300	-0.17	0.08	5.77	0.50	58.92% (6*h*)
		-0.19	0.29	--	0.33	41.08% (2*a*)
Melt-spun Ta0.17	400	-0.33	0.37	--	0.42	100% (PM)
	4.2	-0.17	-0.07	15.1	0.41	25.17% (2*a*)
		-0.21	0.21	19.3	0.39	24.94% (6*h*)
		-0.19	0.14	17.4	0.39	24.94% (6*h*)
		-0.20	-0.14	17.2	0.39	24.94% (6*h*)
	300	-0.20	-0.17	8.3	0.51	8.42% (6*h*)
		-0.19	0.32	--	0.29	21.05% (2*a*)
		-0.20	--	--	1.61	70.54% (R)

To investigate and compare the evolution of the crystal structure during the magnetic transition, X-ray powder diffraction measurements at different temperatures with a step of 20 K were performed for the arc-melted and melt-spun Ta0.17 alloys. Structure refinement shows that the hexagonal C14 Laves phase structure is maintained over the entire temperature range. A phase coexistence is observed between 217 K–257 K, further confirming the first-order phase transition in the arc-melted Ta0.17 alloy. The absence of a phase coexistence in melt-spun

Ta0.17 alloy confirms the presence of a second-order phase transition. The refined unit-cell volume and lattice parameters for the two alloys are given in Fig. 5.3(c-f). The arc-melted alloy shows a sharp decrease in unit-cell volume ($\Delta V/V$ = -0.4%) between 237–277 K with a negative coefficient of thermal expansion $\alpha_v \approx -100\times10^{-6}$ K^{-1}, comparable to other Fe_2(Hf,Ta) compounds with a first-order transition [5, 7]. The critical change in the thermal expansion curve of the unit-cell volume at 317 K is assigned to the Néel temperature [7], which is consistent with the AFM phase at room temperature in the Mössbauer spectra. On the other hand, the melt-spun alloy exhibits a broad FM-AFM transition accompanied by a lower negative thermal expansion α_v = -19 $\times10^{-6}$ K^{-1} within the temperature range of 197–297 K. According to the XRD refinement, this broad FM-AFM transition may be caused by the introduced Hf at the 2*a* site, which to some extent destroys the Kagome layers formed by the Fe atoms occupying the 2*a* site. Therefore, melt spinning can be an effective method to extend the temperature range for the applications of negative thermal expansion in Fe_2(Hf,Ta) compounds.

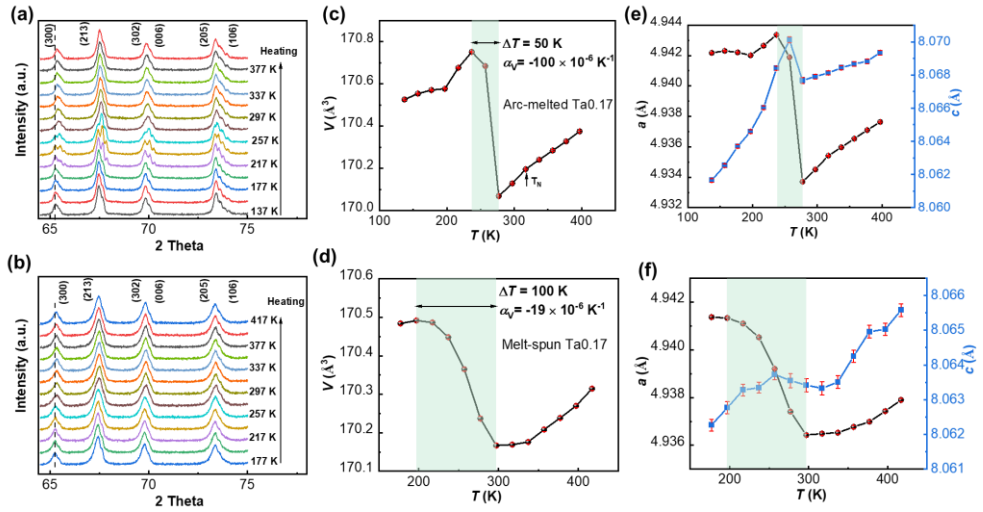

Fig. 5.3. (a, b) XRD patterns as a function of the scattering angle 2 theta, recorded upon heating for a temperature step of 20 K. Temperature dependence of (c, d) unit-cell volume *V* and (e, f) lattice parameters *a* and *c*.

To calculate the magnetic entropy change, a series of *M-T* curves is measured, as shown in Fig. 5.4(a) and (b). The magnetic field shifts the transition to higher temperature because the magnetic field favours the FM state. ΔS_m is calculated based on Maxwell relations from the *M-T* curves. An asymmetric shape of ΔS_m is observed with increasing temperature in the arc-melted alloy, while a symmetric shape is present for the melt-spun alloy. Both alloys show the same maximum magnetic entropy change of about 1.0 J/kgK for a magnetic field change of 2 T in Fig. 5.4(c) and (d). However, the magnetic field dependence of the transition temperature $m = dT_t/d\mu_0 H$ is different: 4.4 K/T for the melt-spun alloy and 8.6 K/T for the arc-melted alloy. For the arc-melted Ta0.17 alloy, the value of *m* is in good agreement with 7.2 K/T for $Fe_2Hf_{0.825}Ta_{0.175}$ [30] or 7.7 K/T for $Fe_2Hf_{0.85}Ta_{0.15}$ [22], which is larger than 4.6 K/T for $Mn_2Sb_{0.08}Cr_{0.02}$ [31], but comparable to 9.0 K/T for $Fe_{48}Rh_{52}$ [32] with an order-order magnetic transition. Although a small *m* is required for a maximum adiabatic temperature change at a complete transition, a large *m* contributes to the completion of phase transition in a limited magnetic field [33, 34]. For different magnetic applications, *m* can be tuned by melt-spinning with a suitable solidification rate.

For the melt-spun Ta0.17 alloy, ΔT_{ad} is extracted from DSC measurements at a home-made in-field DSC [25-27]. As shown in Fig. 5.4(f), the value of ΔT_{ad} is 0.7 K at 289 K in a magnetic field change of 1.5 T and 0.5 K at 288 K in a magnetic field change of 1 T. The value of ΔT_{ad} of the melt-spun Ta0.17 alloy is smaller than that of the arc-melted $Hf_{0.84}Ta_{0.16}Fe_2$ alloy (3.4 K at the magnetic field change of 1.5 T) [6], which is due to the wide magnetic transition for the melt-spun Ta0.17 alloy. The coefficient of refrigerant performance (*CRP*) reflects the MCE performance and can be determined by the following relation: $CRP = \frac{|\Delta S_m|\Delta T_{rev}}{\int_0^{\mu_0 H} M(T_C,H) d\mu_0 H}$ [35], where ΔT_{rev} is the reversible adiabatic temperature change. Considering $|\Delta S_m|$ = 0.5 J/kgK and ΔT_{rev} = 0.5 K (taken from in-field DSC measurements) at a magnetic field change of 1 T, the calculated value for *CRP* in melt-spun Ta0.17 alloy is 0.01, which is smaller

than for commercial Gd (0.17) [36], but comparable to other second-order phase transition materials such as $Ni_{33}Co_{17}Mn_{30}Ti_{20}$ (0.01) [37].

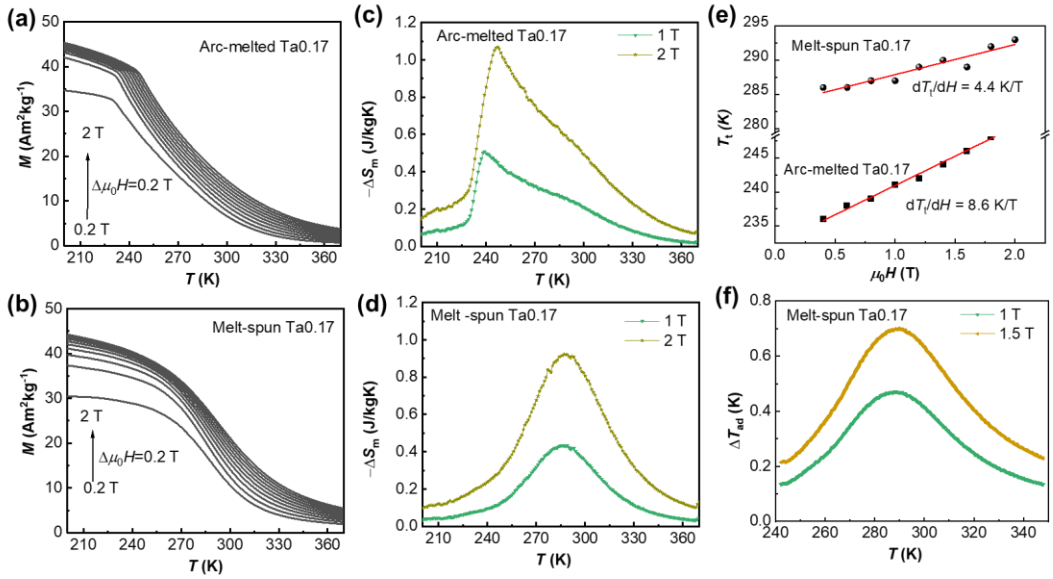

Fig. 5.4. *M-T* curves upon heating in different applied magnetic fields for (a) arc-melted Ta0.17 and (b) melt-spun Ta0.17. $-\Delta S_m$ calculated from the heating curves for (c) arc-melted Ta0.17 and (d) melt-spun Ta0.17. (e) T_t as a function of magnetic field. (f) ΔT_{ad} derived from in-field DSC.

5.4 Conclusions

In summary, we have compared the magnetoelastic transition, the microstructure and the magnetocaloric effect in arc-melted and melt-spun $Fe_2Hf_{0.83}Ta_{0.17}$ compounds. A first-order magnetoelastic phase transition from the FM to the AFM phase is observed in the arc-melted alloy, while a second-order phase transition is observed in the melt-spun alloy. The same magnetic entropy change of about 1 J/kgK for a magnetic field change of 2 T is obtained for the arc-melted alloy at 247 K and for the melt-spun alloy at 287 K. A thermal hysteresis of 2 K and a phase coexistence in the temperature range 217–257 K is found in the arc-melted alloy. In contrast, the melt-spun alloy

undergoes a typical second-order phase transition accompanied by a negative thermal expansion effect with $\alpha_v = -19\times10^{-6}$ K^{-1} over a wide temperature range of 197–297 K.

References

[1] E. Brück, O. Tegus, D.T. Cam Thanh, N.T. Trung, K.H.J. Buschow, A review on Mn based materials for magnetic refrigeration: Structure and properties, Int. J. Refrig. 31 (2008) 763-770.

[2] T. Gottschall, K.P. Skokov, M. Fries, A. Taubel, I. Radulov, F. Scheibel, D. Benke, S. Riegg, O. Gutfleisch, Making a Cool Choice: The Materials Library of Magnetic Refrigeration, Adv. Energy Mater. 9 (2019) 1901322.

[3] O. Gutfleisch, M.A. Willard, E. Bruck, C.H. Chen, S.G. Sankar, J.P. Liu, Magnetic materials and devices for the 21st century: stronger, lighter, and more energy efficient, Adv. Mater. 23 (2011) 821-42.

[4] V.K. Pecharsky, J. Cui, D.D. Johnson, (Magneto)caloric refrigeration: is there light at the end of the tunnel?, Philos. Trans. R. Soc. A 374 (2016) 20150305.

[5] L.F. Li, P. Tong, Y.M. Zou, W. Tong, W.B. Jiang, Y. Jiang, X.K. Zhang, J.C. Lin, M. Wang, C. Yang, X.B. Zhu, W.H. Song, Y.P. Sun, Good comprehensive performance of Laves phase $Hf_{1-x}Ta_xFe_2$ as negative thermal expansion materials, Acta Mater. 161 (2018) 258-265.

[6] Z. Song, Z. Li, B. Yang, H. Yan, C. Esling, X. Zhao, L. Zuo, Large Low-Field Reversible Magnetocaloric Effect in Itinerant-Electron $Hf_{1-x}TaxFe_2$ Alloys, Materials 14 (2021) 1-11.

[7] B. Li, X.H. Luo, H. Wang, W.J. Ren, S. Yano, C.W. Wang, J.S. Gardner, K.D. Liss, P. Miao, S.H. Lee, T. Kamiyama, R.Q. Wu, Y. Kawakita, Z.D. Zhang, Colossal negative thermal expansion induced by magnetic phase competition on frustrated lattices in Laves phase compound (Hf,Ta)Fe_2, Phys. Rev. B 93 (2016) 224405.

[8] L.V.B. Diop, O. Isnard, E. Suard, D. Benea, Neutron diffraction study of the itinerant-electron metamagnetic $Hf_{0.825}Ta_{0.175}Fe_2$ compound, Solid State Commun. 229 (2016) 16-21.

[9] A. Fujita, S. Fujieda, Y. Hasegawa, K. Fukamichi, Itinerant-electron metamagnetic transition and large magnetocaloric effects in $La(Fe_xSi_{1-x})_{13}$ compounds and their hydrides, Phys. Rev. B 67 (2003) 104416.

[10] N.H. Dung, Z.Q. Ou, L. Caron, L. Zhang, D.T.C. Thanh, G.A. de Wijs, R.A. de Groot, K.H.J. Buschow, E. Brück, Mixed magnetism for refrigeration and energy conversion, Adv. Energy Mater. 1 (2011) 1215-1219.

[11] L.V.B. Diop, D. Benea, S. Mankovsky, O. Isnard, Cross over between ferro and antiferromagnetic order in Fe itinerant electron magnetism: An experimental and theoretical study of the model $(Hf,Ta)Fe_2$ Laves phases, J. Alloys Compd. 643 (2015) 239-246.

[12] Y.J. Huang, S.Z. Li, Z.D. Han, W.X. Wang, Z.Y. Jiang, S.L. Huang, J. Lin, Y.F. Hsia, Mössbauer study of the spin reorientation in pseudobinary alloy $Hf_{0.82}Ta_{0.18}Fe_2$, J. Alloys Compd. 427 (2007) 37-41.

[13] Z. Han, D. Wang, S. Huang, Z. Su, S. Tang, Y. Du, Low-field magnetic entropy changes in $Hf_{1-x}Ta_xFe_2$, J. Alloys Compd. 377 (2004) 75-77.

[14] S.Y. Dong, X.Z. Yang, J.Y. Chen, Q. Shao, B. Qian, Z.D. Han, C.L. Zhang, X.F. Jiang, Large low-field magnetic entropy changes in as-cast $Hf_{0.83-x}Zr_xTa_{0.17}Fe_2$ compounds, Physica B 466-467 (2015) 86-89.

[15] J. Dong, M. Zhang, J. Liu, P. Zhang, A. Yan, Magnetic properties and magnetocaloric effect of Hf–Ta–Fe–(Co) alloys, Physica B 476 (2015) 171-174.

[16] Z.Q. Ou, L. Zhang, N.H. Dung, L. van Eijck, A.M. Mulders, M. Avdeev, N.H. van Dijk, E. Brück, Neutron diffraction study on the magnetic structure of Fe_2P-based $Mn_{0.66}Fe_{1.29}P_{1-x}Si_x$ melt-spun ribbons, J. Magn. Magn. Mater. 340 (2013) 80-85.

[17] X.B. Liu, X.D. Liu, Z. Altounian, G.H. Tu, Phase formation and structure in rapidly quenched alloys $La(Fe_{0.88}Co_{0.12})_{13-x}Si_x$ alloys, J. Alloys Compd. 397 (2005) 120-125.

[18] T. Zhang, Y. Chen, Y. Tang, The magnetocaloric effect and hysteresis properties of melt-spun $Gd_5Si_{1.8}Ge_{1.8}Sn_{0.4}$ alloy, Journal of Physics D 40 (2007) 5778-5784.

[19] B. Hernando, J.L. Sánchez Llamazares, J.D. Santos, V.M. Prida, D. Baldomir, D. Serantes, R. Varga, J. González, Magnetocaloric effect in melt spun $Ni_{50.3}Mn_{35.5}Sn_{14.4}$ ribbons, Appl. Phys. Lett. 92 (2008) 132507.

[20] A. Yan, K.H. Müller, O. Gutfleisch, Structure and magnetic entropy change of melt-spun $LaFe_{11.57}Si_{1.43}$ ribbons, J. Appl. Phys. 97 (2005) 036102.

[21] Z.Q. Ou, L. Zhang, N.H. Dung, L. Caron, E. Brück, Structure, magnetism and magnetocalorics of Fe-rich $(Mn,Fe)_{1.95}P_{1-x}Si_x$ melt-spun ribbons, J. Alloys Compd. 710 (2017) 446-451.

[22] Y. Nishihara, Magnetic phase transitions in itinerant electron magnets $Hf_{1-x}Ta_xFe_2$, J. Phys. Soc. Jpn. 52 (1983) 3630-3636.

[23] H. Wada, N. Shimamura, M. Shiga, Thermal and transport properties of $Hf_{1-x}Ta_xFe_2$, Phys Rev B 48 (1993) 10221-10226.

[24] B.H. Toby, R factors in Rietveld analysis: How good is good enough?, Powder Diffr. 21 (2012) 67-70.

[25] G. Porcari, M. Buzzi, F. Cugini, R. Pellicelli, C. Pernechele, L. Caron, E. Bruck, M. Solzi, Direct magnetocaloric characterization and simulation of thermomagnetic cycles, Rev. Sci. Instrum. 84 (2013) 073907.

[26] G. Porcari, F. Cugini, S. Fabbrici, C. Pernechele, F. Albertini, M. Buzzi, M. Mangia, M. Solzi, Convergence of direct and indirect methods in the magnetocaloric study of first order transformations: The case of Ni-Co-Mn-Ga Heusler alloys, Phys. Rev. B 86 (2012) 104432.

[27] G. Porcari, S. Fabbrici, C. Pernechele, F. Albertini, M. Buzzi, A. Paoluzi, J. Kamarad, Z.-Arnold, M. Solzi, Reverse magnetostructural transformation and adiabatic temperature change in Co- and In-substituted Ni-Mn-Ga alloys, Phys. Rev. B 85 (2012) 024414.

[28] Z. Klencsar, Mössbauer spectrum analysis by evolution algorithm, Nucl. Instrum. Meth. B 129 (1997) 527-533.

[29] J.A. García, J. Carrizo, L. Elbaile, D. Lago-Cachón, M. Rivas, D. Castrillo, A.R. Pierna, Magnetic anisotropy and magnetostriction in nanocrystalline Fe–Al

alloys obtained by melt spinning technique, J. Magn. Magn. Mater. 372 (2014) 27-32.

[30] L.V.B. Diop, M. Amara, O. Isnard, Large magnetovolume effects due to transition from the ferromagnetic to antiferromagnetic state in $Hf_{0.825}Ta_{0.175}Fe_2$ intermetallic compound, J.-Phys. Condens. 25 (2013) 416007.

[31] Q. Shen, I. Batashev, H. Ojiyed, F. Zhang, N. van Dijk, E. Brück, Nonlinear influence of excess Mn on the magnetoelastic transition in $(Mn,Cr)_2Sb$, J. Alloys Compd. 903 (2022) 164011.

[32] A.M. Aliev, A.B. Batdalov, L.N. Khanov, A.P. Kamantsev, V.V. Koledov, A.V. Mashirov, V.G. Shavrov, R.M. Grechishkin, A.R. Kaul, V. Sampath, Reversible magnetocaloric effect in materials with first order phase transitions in cyclic magnetic fields: $Fe_{48}Rh_{52}$ and $Sm_{0.6}Sr_{0.4}MnO_3$, Appl. Phys. Lett. 109 (2016) 202407.

[33] J. Liu, T. Gottschall, K.P. Skokov, J.D. Moore, O. Gutfleisch, Giant magnetocaloric effect driven by structural transitions, Nat. Mater. 11 (2012) 620-6.

[34] K.G. Sandeman, Magnetocaloric materials: The search for new systems, Scr. Mater. 67 (2012) 566-571.

[35] E. Brück, H. Yibole, L. Zhang, A universal metric for ferroic energy materials, Philos. Trans. R. Soc. A 374 (2016) 20150303.

[36] M.E. Wood, W.H. Potter, General analysis of magnetic refrigeration and its optimization using a new concept: maximization of refrigerant capacity, Cryogenics 125 (1985) 667-683.

[37] F. Zhang, K. Westra, Q. Shen, I. Batashev, A. Kiecana, N. van Dijk, E. Brück, The second-order magnetic phase transition and magnetocaloric effect in all-d-metal NiCoMnTi-based Heusler alloys, J. Alloys Compd. 906 (2022) 164337.

Supplementary Material for Chapter 5

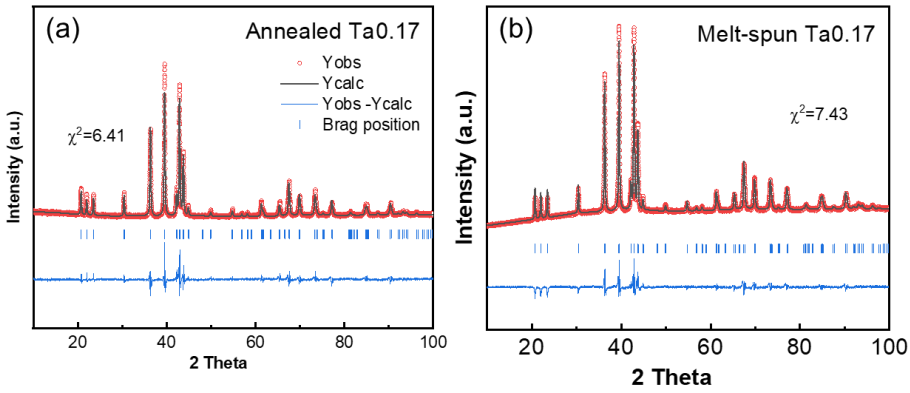

Fig. S5.1. (a) Rietveld refinement results of the XRD patterns of (a) annealed Ta0.17 and (b) melt-spun Ta0.17 assuming that all the Hf atoms are located at the 4*f* site.

Table S5.1. Rietveld refinement of the XRD data for the arc-melted, annealed and melt-spun Ta0.17 alloys. $Fe_2Hf_{0.83}Ta_{0.17}$ has a hexagonal $P6_3/mmc$ space group with four formula units per unit cell. The Fe atoms are located in two different crystallographic positions at the *2a* (0, 0, 0) and *6h* (x, $2x$, 1/4) sites. The Hf/Ta atoms randomly occupy the 4*f* (1/3, 2/3, z) site except that some Hf atoms occupy the 2*a* site because of rapid solidification. Listed are the lattice parameters a and c, the internal coordinates for the 6*h* (x) and 4*f* (z) sites, the occupations of the 2*a* and the 4*f* sites with Hf atoms and of the *2a* site with Fe atoms, and the quality of the fit (R_p/R_{wp} and χ^2).

	Arc-melted Ta0.17	Annealed Ta0.17	Melt-spun Ta0.17
a (Å)	4.94363(7)	4.94201(7)	4.94683(5)
c (Å)	8.07994(13)	8.07816(14)	8.07870(10)
V (Å^3)	171.013(4)	170.864(5)	171.209(3)
x	0.16788(60)	0.16863(56)	0.16788(60)
z	0.56437(14)	0.56182(13)	0.56437(14)
Occ(Hf-4*f*)	0.133	0.135	0.121 (0.017 at 2*a*)
Occ(Fe-2*a*)	0.083	0.084	0.043
R_p/R_{wp}	3.72/5.22	3.35/4.96	2.93/4.07
χ^2	4.49	6.41	5.23

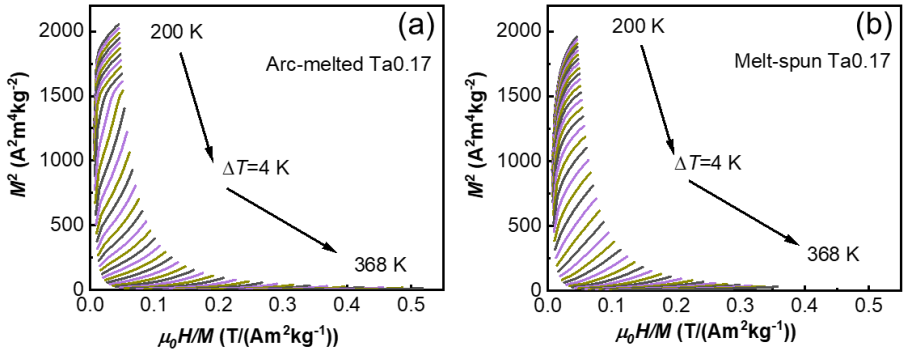

Fig. S5.2. Arrott plots for (a) arc-melted Ta0.17 and (b) melt-spun Ta0.17.

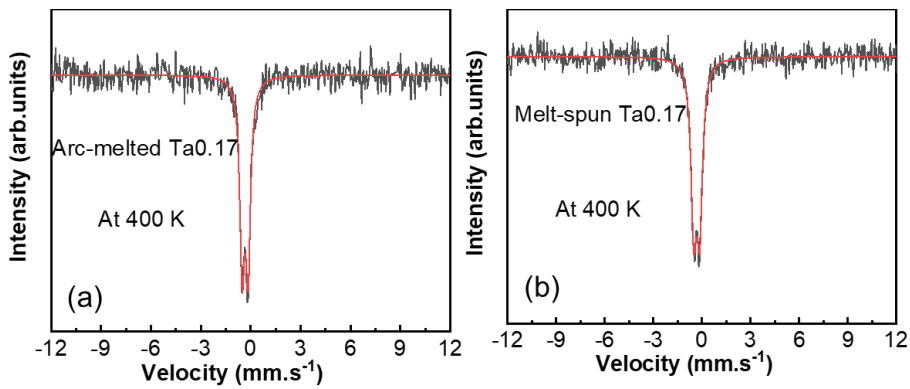

Fig. S5.3. Mössbauer spectra at 400 K for (a) arc-melted Ta0.17 and (b) melt-spun Ta0.17.

Chapter 6 Exploring the negative thermal expansion and magnetocaloric effect in Fe_2(Hf,Ti) Laves phase materials

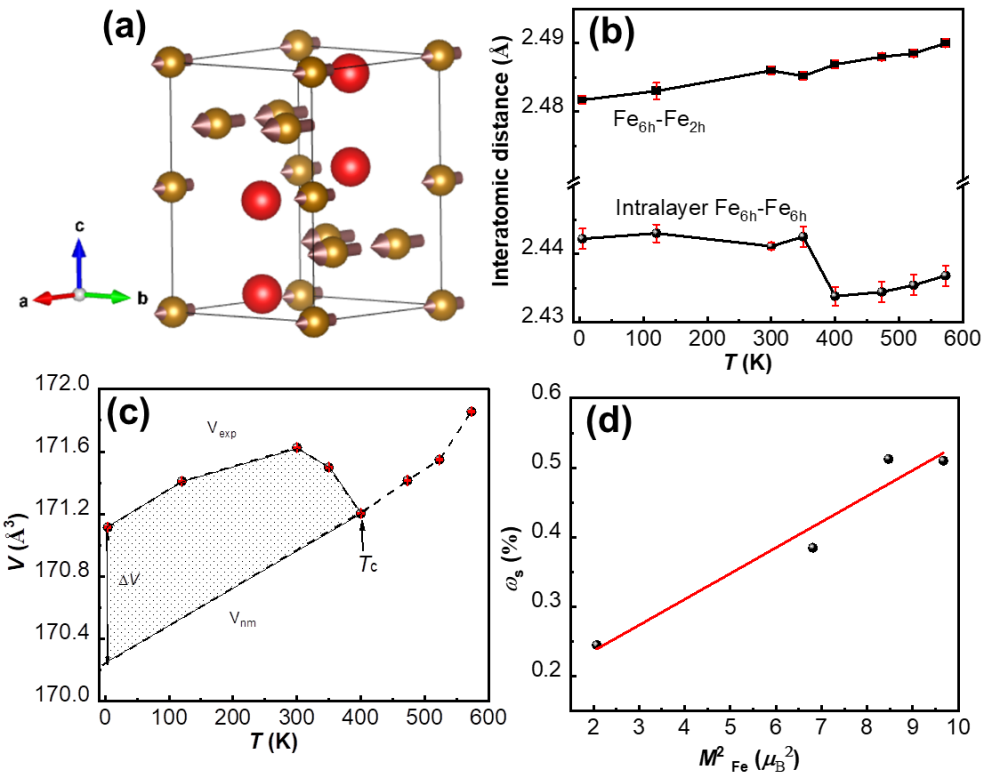

This chapter is based on:

Q. Shen, F. Zhang, I. Dugulan, N. van Dijk, E. Brück, Exploring the negative thermal expansion and magnetocaloric effect in Fe_2(Hf,Ti) Laves phase materials, Acta Mater. 257 (2023) 119149.

Abstract

The transition-metal based Laves phase materials represent an extended family of alloys with rich and fascinating physical properties. In this work, we have investigated the negative thermal expansion and magnetocaloric effect in arc-melted and melt-spun $Fe_2Hf_{1-x}Ti_x$ (x = 0.15, 0.27, 0.30, 0.33, 0.36, 0.40) alloys. For x = 0.30 –0.40, two hexagonal phases with different compositions share the same $P6_3/mmc$ lattice symmetry, but have slightly different lattice parameters. The saturation magnetization and Curie temperature both follow a decreasing trend with the average unit-cell volume. For $Fe_2Hf_{0.6}Ti_{0.4}$ melt spinning improves the saturation magnetization from 48.7 to 59.6 Am^2/kg and the magnetic entropy change from 0.46 to 0.54 J/kgK at a magnetic field change of 2 T. These enhanced values are attributed to an improved homogeneity caused by a suppression of phase segregation during rapid solidification. We have utilized neutron powder diffraction and Mössbauer spectroscopy to illustrate the correlation between the magnetic order and the negative thermal expansion in single-phase $Fe_2Hf_{0.85}Ti_{0.15}$. The magnetic moments of Fe align below 400 K in the *a-b* plane and a moment change for the Fe atoms is responsible for the large volumetric coefficient of thermal expansion of -25×10^{-6} K^{-1} over a wide temperature range of 300–400 K.

6.1 Introduction

The magnetocaloric effect (MCE) is the caloric response of the lattice on the application or removal of a magnetic field and can be characterized by the magnetic entropy change and the adiabatic temperature change [1, 2]. In terms of the energy efficiency and environmental safety of MCE-based magnetic refrigeration, the exploration of new MCE materials and the understanding of the mechanism controlling the magnetic phase transition have attracted much attention in recent decades [3, 4]. Many magnetocaloric materials undergoing a magnetostructural or a magnetoelastic transition have been studied, such as Mn-Fe-P-Si [5, 6], $La(Fe,Si)_{13}$ [7, 8], Ni-Mn-based Heusler alloys [9, 10], MnCoGe [11], Fe_2(Hf,Ta) [12-14] and Mn_2Sb [15-17]. Due to the strong spin-lattice coupling, some of the magnetocaloric materials, such as La-Fe-Si-Co [18], MnCoGe [19], and Fe-based Laves phase materials [20, 21], are also considered as potential candidates for negative thermal expansion (NTE) materials, which are in high demand in modern industry for the adjustment of the thermal expansion in materials [22, 23]. Among these magnetic Fe-based Laves phase materials combine a spontaneous magnetization with a magnetoelastic lattice volume contribution based on two different Fe atomic sites, which combine the advantages of a high thermal conductivity and good mechanical properties for NTE materials and magnetocaloric applications [20] [14].

MCE materials with a large magnetic entropy change generally show a large change in magnetic moment. It is well known that itinerant electron systems with a large magnetic moment have a larger unit-cell volume. Therefore, a steep change in magnetization for itinerant electron system is generally linked to a steep change in volume, except for magnetic materials that rather change *c/a* ratios, which may yet occur without volume change. An interesting example is the Fe_2(Hf,Ta) Laves phase, which shows a sharp magnetization jump at the ferromagnetic-to-antiferromagnetic phase transition, accompanied by a negative thermal expansion effect [24]. This sharp transition is due to a frustration effect, in which the magnetic moment of the Fe atom at the 2*a* site of the hexagonal $P6_3/mmc$ structure (space group 194) disappears below

the transition temperature [25]. This leads to a large adiabatic temperature change of about 3.4 K in the presence of a relatively low change in applied magnetic field of 1.5 T [14]. The tuneable transition temperature, large adiabatic temperature change and small thermal hysteresis make these compounds attractive for magnetocaloric applications [13, 14]. On the other hand, the linear NTE coefficient of $-16.3\times10^{-6}\,K^{-1}$ over a broad temperature window of 105 K (222–327 K) is attributed to the asynchronous ferromagnetic ordering of the Fe moments at the 6*h* and 2*a* sites revealed by Electron Spin Resonance [20]. A similar magnetoelastic transition has also been observed in Fe-based $Fe_2(Sc,Ti)$ [21], $Fe_2(Hf,Ti)$ [26] and $Fe_2(Hf,Nb)$ [27] Laves phase materials. So far however, there have only been a limited number of systematic reports on the mechanism responsible for the magnetoelastic coupling in Fe-based Laves phase materials.

In this work, Mössbauer spectroscopy, neutron powder diffraction and DFT calculations are employed to investigate the correlation between the negative thermal expansion and the magnetic behaviour in $Fe_2(Hf,Ti)$ compounds. In addition, we propose a materials fabrication method to enhance the magnetocaloric effect in $Fe_2(Hf,Ti)$ Laves phase materials by suppressing phase segregation using melt-spinning technique.

6.2 Experimental methods

Polycrystalline $Fe_2Hf_{1-x}Ti_x$ (x = 0.15, 0.27, 0.30, 0.33, 0.36, 0.40) compounds were prepared from high-purity elements (Fe 99.98%, Hf 99.95%, Ti 99.99%) by arc melting. Samples with a total mass of 5 g were melted four or five times, and the button-shaped alloys were flipped over after each melting. Four different heat treatments were tried for x = 0.36: (a) annealing at 1173 K for 24 h and quenching; (b) annealing at 1273 K for 134 h and quenching; (c) annealing at 1323 K for 24 h and quenching; (d) annealing at 1373 K for 24 h and quenching. All these heat treatments resulted in comparable lattice parameters, saturation magnetizations and transition temperatures (see Fig. S6.1 in Supplementary Material). Accordingly, only

as-cast samples are reported for most compositions (with some exceptions noted in the results reported below). For $Fe_2Hf_{1-x}Ti_x$ (x = 0.36, 0.40) compounds, the melt-spinning technique is used to improve homogeneity. The crucible of melt-spinning device is a commercial quartz tube with a melting point of 1883 K. The melting point of $Fe_2Hf_{1-x}Ti_x$ is estimated to be about 1673 K. The melt-spun ribbons were produced under argon atmosphere at different surface speeds of the copper wheel. By comparing the melt-spun ribbons with different heat treatments (see Fig. S6.2 in Supplementary Material), those without a heat treatment are characterized for the discussion.

X-ray diffraction (XRD) data were collected with a Panalytical X-Pert PRO using Cu-K_α radiation and an Anton Paar TTK 450 temperature chamber. The lattice structure was analysed by Rietveld refinement using Fullprof [28]. The magnetic properties at low temperature (4–370 K) were measured using a superconducting quantum interference device (SQUID) magnetometer model MPMS-XL, equipped with the reciprocating sample option. Magnetisation measurements at high-temperature (315–650 K) were carried out using a vibrating sample magnetometer (VSM) model LakeShore 7307 equipped with a high-temperature furnace (model 73034). The ferromagnetic transition temperature T_C is determined from the minimum in the temperature derivative of the magnetization as a function of temperature at an applied magnetic field of 1 T. The magnetic entropy change was calculated from the *M-T* curves obtained at different magnetic fields using the Maxwell relations. Differential scanning calorimetry (DSC) measurements were performed in a commercial TA-Q2000 DSC calorimeter (at a sweep rate of 10 K/min). The microstructure was analysed by scanning electron microscopy (SEM) using a FEI Quanta FEG 450 equipped with energy dispersive X-ray spectroscopy (EDS). Transmission ^{57}Fe Mössbauer spectra were collected at different temperatures in the range from 4.2 to 300 K with conventional constant-acceleration or sinusoidal velocity spectrometers using a ^{57}Co(Rh) source. The velocity calibration was performed using an α-Fe foil at room temperature. The source and the absorbing

samples were kept at the same temperature during the cryogenic measurements. The Mössbauer spectra were fitted using the Mosswinn 4.0 program [29]. Powder neutron diffraction (ND) data at different temperatures were collected at a wavelength of 1.6672 Å using the ND apparatus PEARL [30] at the research reactor of Delft University of Technology. The crystal structures and the atomic occupancies were refined using the Rietveld refinement method implemented in the Fullprof software package [31-33].

Density functional theory (DFT) modelling was performed with the Vienna ab initio simulation package (VASP) [34, 35]. Exchange interactions were taken into account by using the generalized gradient approximation (GGA) by Perdew, Burke, and Ernzerhof (PBE) [36]. For all calculations, the projector augmented-wave (PAW) [37, 38] pseudopotentials were used with the valence electron configuration 5*p*5*d*6*s* for Hf, 3*s*3*p*3*d*4s for Ti and 3*d*4*s* for Fe. All calculations were performed for a $1\times1\times2$ supercell. The structural degrees of freedom were fully relaxed on a gamma centred *k*-grid of $11\times11\times3$. The *k*-space integrations were performed using the second order Methfessel-Paxton method [39] with a smearing width of 0.05 eV. The lattice parameters and atomic positions were optimized with the criteria that the atomic force is weaker than 0.1 meV/Å and an energy convergence of 1 μeV. The kinetic energy cutoff was set at 400 eV.

6.3 Results and discussion

Fig. 6.1(a) shows the XRD patterns for arc-melted $Fe_2Hf_{1-x}Ti_x$ (x = 0.15, 0.27, 0.30, 0.33, 0.36, 0.40), denoted as TiX alloys (where X corresponds to the Ti fraction x). With increasing Ti substitution, the peaks become broader, which is seen in the enlarged region in Fig. 6.1(b) and the increased full width at half-maximum (FWHM) in Fig. 6.2(a). All samples crystallize in the hexagonal $MgZn_2$-type structure with $P6_3/mmc$ symmetry (space group 194), where the Fe atoms occupy the *2a* and *6h* sites and the Hf/Ti atoms occupy the *4f* site. According to the Rietveld refinement results in Fig. 6.1(c) the patterns for the Ti0.15 and Ti0.27 samples can be fitted best as

single-phase hexagonal. The other four samples, for example the Ti0.36 sample in Fig. 6.1(d), can be fitted best by a two-phase model. These two phases share the same space group 194, but with slightly different lattice parameters. The refined lattice parameters are given in Fig. 6.2(d-f). The fraction of the Ti-rich phase P1 increases with increasing Ti content. The average unit-cell volume, based on the fraction of the two phases P1 and P2, decreases linearly with Ti content.

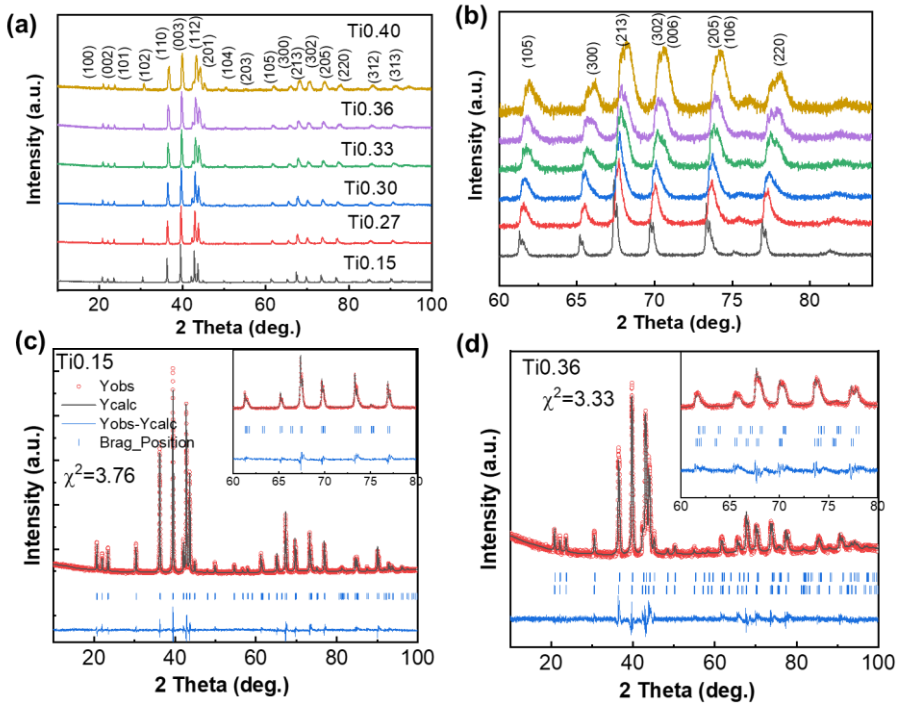

Fig. 6.1. (a) XRD patterns of arc-melted $Fe_2Hf_{1-x}Ti_x$(x = 0.15, 0.27, 0.30, 0.33, 0.36). (b) Zoomed-in region between 60–90° from (a). (c, d) Rietveld refinement results of the arc-melted Ti0.15 and Ti0.36 samples with the zoomed-in region of 60–80° as the inset graphs.

To confirm the presence of phase segregation, the backscattered electron SEM images of the arc-melted Ti0.36 sample are shown in Fig. 6.2(b). The dark region refers to the Ti-rich phase, corresponding to P1. The chemical compositions of the matrix and Ti-rich phase are determined by EDS and are found to be $Fe_{65.9}Hf_{25.5}Ti_{8.6}$

and $Fe_{66.3}Hf_{19.7}Ti_{14.0}$, respectively. It is found that this phase segregation is difficult to avoid by different heat treatments (see Fig. S6.1 in Supplementary Material). It is worthwhile to note that in $Hf_{0.6}Ti_{0.4}Fe_2$ [26] a similar XRD peak broadening is attributed to a phase coexistence of AFM and FM states, where the homogeneity is supported by SEM mapping at the scale of 100 μm. A variation in chemical composition at a smaller length scale or in other areas of the samples cannot be excluded [40]. From the inset in Fig. 6.2(c), the annealed Ti0.36 sample (annealed at 1273 K for 134 hours) exhibits significant compositional fluctuations, as indicated from the line-scan profile across the Ti-rich boundaries. The chemical composition of the matrix and the Ti-rich phases are $Fe_{65.4}Hf_{27.0}Ti_{7.6}$ and $Fe_{65.3}Hf_{18.3}Ti_{16.3}$, respectively.

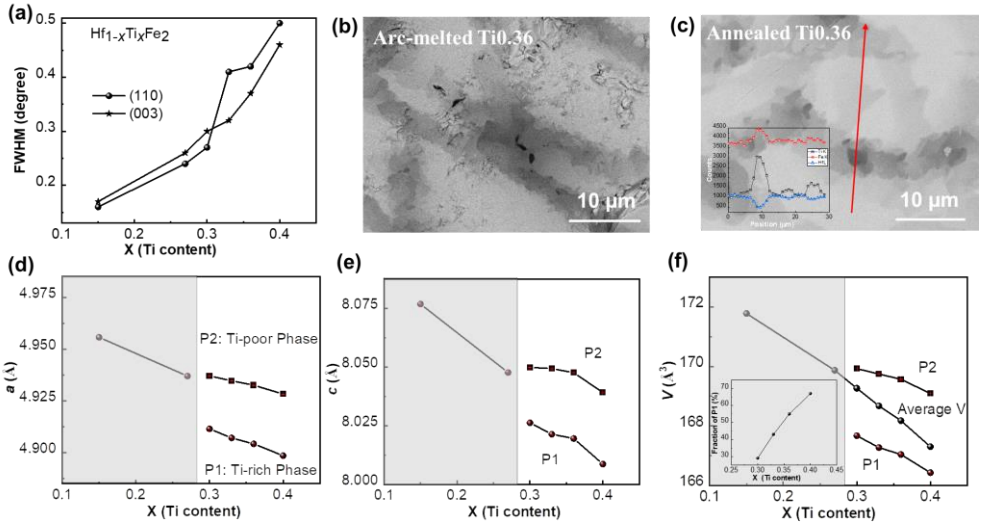

Fig. 6.2. (a) FWHM of (110) and (003) peaks for arc-melted $Fe_2Hf_{1-x}Ti_x$ (x = 0.15, 0.27, 0.30, 0.33, 0.36, 0.40). Backscattered electron SEM images of (b) arc-melted Ti0.36 sample without any heat treatment and (c) arc-melted Ti0.36 sample annealed at 1273 K for 134 hours. (d, e, f) Ti-content dependence of the lattice parameters a and c and the unit-cell volume V. The inset in (f) is the fraction of the Ti-rich P1 phase as a function of the Ti content.

The *M-T* curves in Fig. 6.3(a) show that the magnetization decreases continuously with increasing temperature for the arc-melted Ti0.15 sample. With decreasing temperature it follows the same trajectory without any thermal hysteresis, which suggests a second-order phase transition from the ferromagnetic to the paramagnetic phase. Fig. 6.3(b) and (c) show the *M-T* curves for $Fe_2Hf_{1-x}Ti_x$ (x = 0.15, 0.27, 0.30, 0.33, 0.36, 0.40) compounds in a magnetic field of 0.01 and 1 T, respectively. T_C initially decreases linearly with the average unit-cell volume and then stabilizes around 310 K, as seen in Fig. 6.3(e). Substitution of Hf by Ti decreases the atomic spacing of the Fe atoms and leads to a suppression of the FM order, so that T_C can be tuned between 310 and 390 K by changing the Ti content. A series of *M-H* curves was measured at 5 K, as shown in Fig. 6.3(d). All samples reach a magnetic saturation at the highest field of 5 T. A significant decrease in saturation magnetization is observed for the Ti0.40 sample due to the lower saturation magnetization from the dominant Ti-rich phase (67%).

We employed spin-polarized DFT calculations for the formation energy, lattice parameters and magnetic moment, as shown in Fig. 6.3(g-i). Two magnetic configurations: (*i*) ferromagnetic (FM) structure, with the Fe moments at the 2*a* and 6*h* sites oriented in the *a-b* plane and (*ii*) antiferromagnetic (AFM) structure, with at the 6*h* site ferromagnetically aligned intralayer Fe magnetic moments and antiferromagnetically aligned interlayer Fe magnetic moments, and with unordered Fe magnetic moments at the 2*a* site [13], are considered in our DFT calculations (see Fig. S6.3 in Supplementary Material). Comparing the formation energy of the two magnetic configurations, the FM structure is the more favourable one. As the Ti content increases, the energy difference decreases (in Fe_2Ti the energy difference is merely 6 meV/atom) because the FM is destabilized by the decrease in lattice parameters due to the smaller atomic size of Ti compared to Hf [41]. The total magnetic moment also decreases with increasing Ti content. It is worth noting that the magnetic moment of Fe at the 2*a* site is more sensitive to the Ti content than that of Fe at the 6*h* site. This stronger instability of the Fe magnetic moment at 2*a* site is

also reported in $Ti_{0.70}Sc_{0.30}Fe_2$, as observed by neutron diffraction [42]. The lattice parameter decreases linearly with increasing Ti content. The magnitude of the calculated lattice parameter and magnetic moment are in agreement with the values obtained from XRD and SQUID (single-phase samples), as shown in Fig. 6.3(h) and Fig. 6.3(i). The spin-polarized density of states (DOS) for $Fe_2Hf_{1-x}Ti_x$ (x = 0.125, 0.25, 0.375) is shown in Fig. S6.4. For an increasing Ti substitution the lattice shrinks and the Fermi energy moves towards a lower energy, resulting in a lower magnetization and a lower T_C. The substitution of the Ti atom for the Hf atom brings a peak in the DOS close to the Fermi level, which results in a significant impact on the magnetic interactions.

Phase segregation has also been reported in other Fe-based Laves phase materials such as $Fe_2(Hf,Nb)$ [27, 40], where the cause of phase segregation is attributed to the positive mixing energy calculated by DFT. However, this is ruled out for $Fe_2(Hf,Ti)$, since the formation energy for both the AFM and FM state is about -9 eV according to the DFT calculation in Fig. 6.3(g). For $Fe_2(Hf,Ti)$, the large difference in atom size (7.5%) between Hf (159 pm) and Ti (147 pm) could be responsible for the phase segregation in high-Ti content samples, since a similar phase segregation was observed in the perovskite oxides $Gd_{1-x}Sr_xFeO_{3-\delta}$ [43], which was caused by the large size mismatch of 10% for Gd and Sr ions. Phase segregation is a way to relieve local stresses due to a size mismatch.

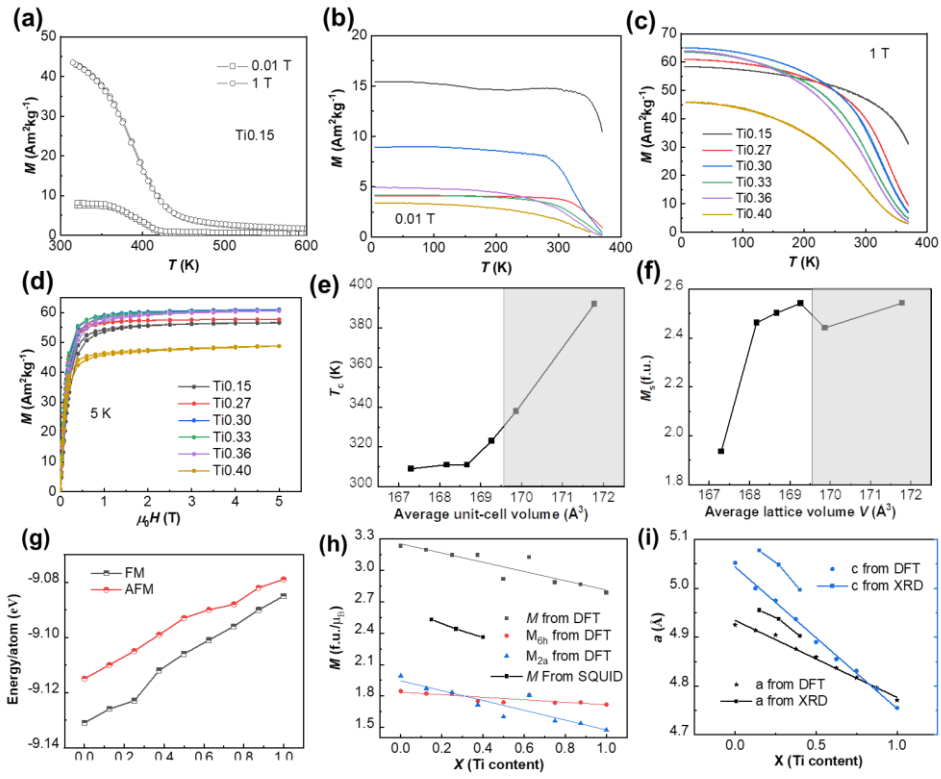

Fig. 6.3. (a) *M-T* curves for the Ti0.15 sample. (b) *M-T* curves of $Fe_2Hf_{1-x}Ti_x$ for heating in a magnetic field of 0.01 T and (c) *M-T* curves of $Fe_2Hf_{1-x}Ti_x$ for heating in a magnetic field of 1 T. (d) *M-H* curves for $Fe_2Hf_{1-x}Ti_x$ at a temperature of 5 K. (e) T_C as a function of the average unit-cell volume of $Fe_2Hf_{1-x}Ti_x$. (f) M_s as a function of average unit-cell volume of $Fe_2Hf_{1-x}Ti_x$. DFT calculation results for the $Fe_2Hf_{1-x}Ti_x$ alloys with: (g) formation energy for the ferromagnetic (FM) and antiferromagnetic (AFM) phase, (h) calculated magnetic moment, and (i) calculated lattice parameters *a* and *c* as a function of the Ti content. For the single-phase samples (arc-melted Ti0.15, Ti0.27 and melt-spun Ti0.40), the experimental magnetic moment and lattice parameters are also given for comparison in (h) and (i), respectively.

Rapid solidification technology, such as melt spinning, is found to suppress phase segregation in $Fe_2Hf_{1-x}Ti_x$ samples with a high-Ti content (x = 0.30, 0.33, 0.36, 0.40). Fig. 6.4(a) shows the homogeneous microstructure for the melt-spun Ti0.36

sample on the wheel side prepared with a wheel surface speed of 17 m/s. In melt spinning, the free side has a lower cooling rate than the wheel side [44]. Therefore, for the Ti0.36 (17 m/s) sample on the free side, the Ti-rich phase can be seen at the grain boundaries, while it is not observed in Ti0.36 (22 m/s) sample. From Fig. 4(b-c) the ribbons are found to be well crystalline with a grain size of about 1-3 µm. Line scanning across the grain boundaries shows that the Ti0.36 (22 m/s) sample is more homogeneous than the Ti0.36 (17 m/s) sample and thus the magnetic transition is sharper than for the latter (see Fig. S6.5(a) in Supplementary Material). Compared to the arc-melting technique, the improved homogeneity in melt-spun samples can be attributed to the fact that the high solidification rate of the melt-spinning process suppresses phase segregation. Therefore, a wheel speed of 30 m/s is used for the melt-spun Ti0.40 sample.

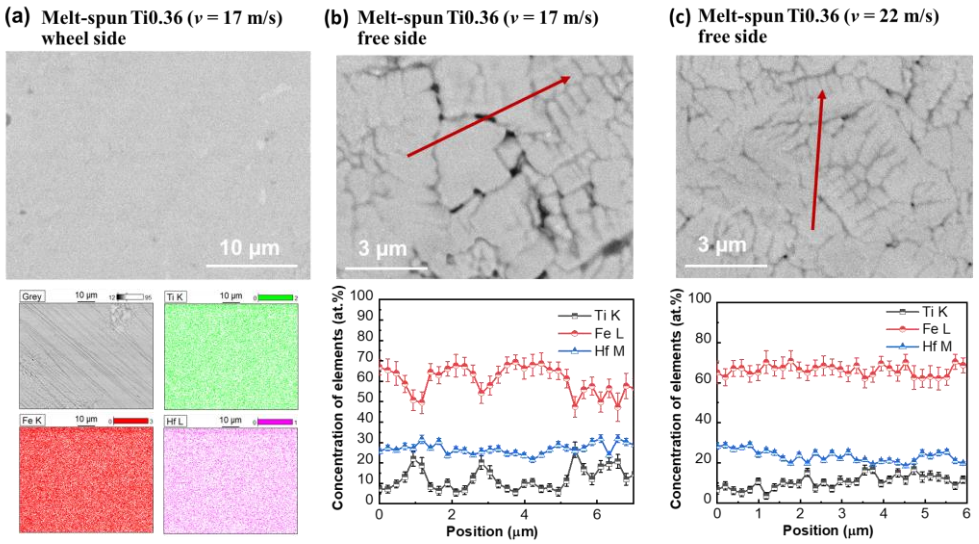

Fig. 6.4. (a) Backscattered electron SEM images and mapping for the melt-spun Ti0.36 (17 m/s) sample (wheel side). Backscattered electron SEM images and line-scanning profile along the red line (b) for the melt-spun Ti0.36 (17 m/s) sample and (c) for the melt-spun Ti0.36 (22 m/s) sample (free side).

The XRD pattern of the melt-spun Ti0.40 (30 m/s) sample shows a single hexagonal $MgZn_2$-type phase (see Fig. S6.6 in Supplementary Material). Fig. 6.5(a) and 6.5(b) show the *M-T* and *M-H* curves for the arc-melted and melt-spun (30 m/s) Ti0.40 samples. The T_C (283 K) of the melt-spun Ti0.40 sample is lower than that of the arc-melted sample (309 K). This can be explained by the fact that the Ti in the melt-spun sample is more homogeneously distributed than in the arc-melted sample, so in the latter only part of the Ti plays a role in reducing T_C. The increased amount of ferromagnetic contribution at high temperature in melt-spun sample can be ascribed to the anti-site disorder of Fe atoms introduced by the melt-spinning process, which is also observed in $(La,Ce)(Fe,Si)_{13}$ [44] and melt-spun $Fe_2(Hf,Ta)$ [45]. On the other hand, M_s increases by 22% from 48.7 Am^2/kg in the arc-melted sample to 59.6 Am^2/kg in the melt-spun sample due to the more homogeneous microstructure. The magnetic entropy change ΔS_m shown in Fig. 6.5(e) and 6.5(f) is calculated from the isofield magnetization curves in Fig. 6.5(c) and (d) using the Maxwell relation: $\Delta S_m(\Delta H, T) = \int_{H_0}^{H} \left(\frac{\partial M(T,H)}{\partial T}\right)_H \mathrm{d}\mu_0 H$, where we choose $\mu_0 H_0$ = 0 T. For the arc-melted Ti0.40 sample, $|\Delta S_m|$ broadens asymmetrically towards the low-temperature region as the magnetic field is increased, whereas the shape of $|\Delta S_m|$ becomes symmetric for the melt-spun sample. The magnetic entropy change $|\Delta S_m|$ under a magnetic field change of 2 T for arc-melted and melt-spun Ti0.40 sample is 0.46 J/kgK at 306 K and 0.54 J/kg K at 280 K, respectively. The melt-spun Ti0.40 sample generates a 20% higher magnetic entropy change. The value of $|\Delta S_m|$ for arc-melted Ti0.15 and Ti0.27 samples is calculated to be 1.1 and 1.0 J/kgK, respectively (see Fig. S6.7(b) and (e) in Supplementary Material). The Arrott-plots of the arc-melted Ti0.15 and Ti0.27 samples in Fig. S6.7(c) and (f) (Supplementary Material) prove that the phase transitions are of second-order, which is consistent with the broad exothermic and endothermic peaks in the DSC curves (see Fig. S6.8 in Supplementary Material). The $|\Delta S_m|$ of $Fe_2Hf_{1-x}Ti_x$ for a magnetic field change of 2 T is comparable to other Fe-based Laves phase materials with a SOMT, with 0.4 J/kgK in $Sc_{0.35}Ti_{0.65}Fe_{1.95}$ [46], but it is smaller than Fe-based Laves phase materials with a

FOMT, such as 1.4 J/kgK in $Sc_{0.35}Ti_{0.65}Fe_{1.95}$ [46] and 2.3 J/kgK in $Fe_2Hf_{0.86}Ta_{0.14}$ [13].

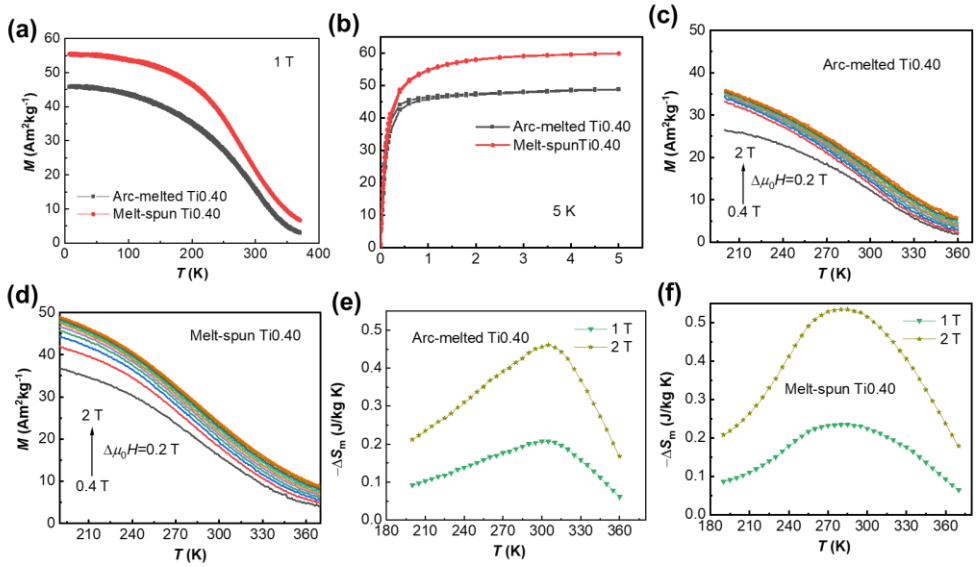

Fig. 6.5. (a) *M-T* curves of arc-melted and melt-spun Ti0.40 samples in a magnetic field of 1 T. (b) *M-H* curves of arc-melted and melt-spun Ti0.40 samples at 5 K. *M-T* curves upon heating in different applied magnetic fields for (c) arc-melted Ti0.40 and (d) melt-spun Ti0.40 samples. Magnetic entropy change $-\Delta S_m$ calculated from the heating curves for (e) arc-melted Ti0.40 and for (f) melt-spun Ti0.40 samples.

To analyse the nature of the magnetoelastic transition in this system, powder neutron diffraction (ND) and Mössbauer spectroscopy were used to study the single-phase arc-melted Ti0.15 sample. To eliminate possible strains due to thermal gradients during arc-melting, the sample was quenched into water after annealing at 1273 K for 32 hours. A detailed Rietveld analysis was performed to refine the crystal structure and magnetic structure from the neutron diffraction patterns at different temperatures. The diffraction patterns recorded at 573 K (PM phase) and 4 K (FM phase) are shown in Fig. 6.6(a) and (b). The diffraction pattern measured at 573 K is characteristic for the nuclear Bragg scattering (PM phase) and was fitted to the $MgZn_2$-type phase with $P6_3/mmc$ symmetry. The ND pattern obtained at 4 K shows

no additional reflections compared to the paramagnetic diffraction pattern. The analysis of the magnetic reflections indicates that the corresponding magnetic structure is defined by the propagation vector **k** = (0,0,0), which means that the magnetic unit cell coincides with the crystallographic one [13]. The arc-melted Ti0.15 sample shows a ferromagnetic ordering of Fe moments below 400 K, which is in good agreement with the T_C (392 K) from SQUID measurements. The FM ordering only increases the intensity at the nuclear peaks. The magnetic contributions are most pronounced at the (100), (101) and (002) peaks. The magnetic Fe moments were independently refined for the 2*a* and 6*h* sites. The best fit corresponds to magnetic moments that lie within the basal plane of the hexagonal lattice. The corresponding FM spin configuration is shown in Fig. 6.6(c). A summary of the crystallographic parameters and the refined Fe moments at different temperatures is shown in Table 6.1. The total moment of 3.14 μ_B/f.u. (calculated by 3/2 $M_{Fe(6h)}$ + 1/2 $M_{Fe(2a)}$) obtained from ND at 4 K agrees well with the 3.19 μ_B/f.u. calculated by DFT.

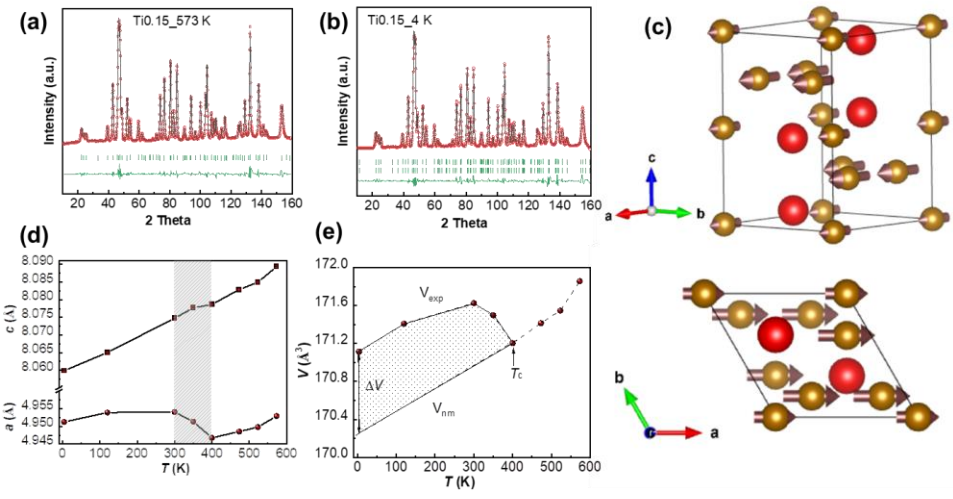

Fig. 6.6. Neutron diffraction **(**ND) patterns for the arc-melted Ti0.15 sample (a) at 573 K and (b) at 4 K. The top row of marked Bragg peak positions is from the nuclear contribution. The second row in (b) corresponds to the magnetic contribution. (c) Refined magnetic moment configuration. Temperature dependence of refined

parameters: (d) lattice constants *a* and *c* and (e) experimental and non-magnetic unit-cell volume (V_{exp} and V_{nm}) from ND as a function of temperature for the arc-melted Ti0.15 sample. V_{nm} is calculated by the extrapolation of the high temperature data for the non-magnetic PM phase by ignoring the expected low-temperature levelling of the thermal expansion. The hatched zone in (d) indicates the NTE window.

Table 6.1. Fitted neutron diffraction parameters of the Ti0.15 sample obtained at different temperatures. The lattice structure corresponds to the $P6_3/mmc$ symmetry (space group 194) with the Fe atoms at the *2a* site with position (0, 0, 0) and the *6h* site with position (x, $2x$, 1/4) and the Hf/Ti atoms at the *4f* site with position (1/3, 2/3, z).

T (K)	*Phase*	$x_{(6h)}$	$z_{(4f)}$	c/a	$M_{Fe(6h)}$ (μ_B/f.u.)	$M_{Fe(2a)}$ (μ_B/f.u.)	χ^2
573	PM	0.16932 (19)	0.56275 (15)	1.62801 (4)	–	–	11.0
523	PM	0.16930 (19)	0.56309 (15)	1.63339 (3)	–	–	13.9
473	PM	0.16933 (19)	0.56277 (15)	1.62992 (4)	–	–	11.9
400	PM	0.16933 (22)	0.56258 (18)	1.63312 (3)	–	–	21.5
350	FM	0.16886 (23)	0.56285 (18)	1.63142 (4)	0.70	0.73	25.3
300	FM	0.16907 (19)	0.56230 (15)	1.63338 (3)	1.16	1.38	13.6
120	FM	0.16894 (16)	0.56253 (13)	1.63326 (3)	1.20	1.58	21.1
4	FM	0.16890 (16)	0.56236 (16)	1.62785 (4)	1.39	1.61	18.3

The temperature dependence of the lattice constants *a* and *c*, and the unit-cell volume *V* are displayed in Fig. 6(d,e). The lattice constant *c* increases continuously, while *a* only increases slowly from 4 to 300 K and, then decreases from 300 to 400 K and finally increases again from 400 to 573 K. As a result, *V* decreases abnormally from 300 to 400 K. The drop in lattice constant *a* is about 0.15%, about half that of $Hf_{0.86}Ta_{0.14}Fe_2$ [13]. The unit-cell volume of the FM phase is larger than that of the PM phase, and the spontaneous volume magnetostriction accompanying the second-order magnetic phase transition is estimated to be about $\Delta V/V = 0.25\%$. The negative thermal expansion observed from 300 K (171.63 $Å^3$) to 400 K (171.20 $Å^3$) leads to a negative thermal expansion coefficient $\alpha_v = (1/V)\times(\Delta V/\Delta T) = -25 \times 10^{-6}\ K^{-1}$ over a temperature range of 100 K, in agreement with [26]. This negative thermal expansion coefficient is comparable to commercial NTE materials such as ZrW_2O_8 ($\alpha_v = -27.3\times10^{-6}\ K^{-1}$, 0–300 K) [47] and $PbTiO_3$ ($\alpha_v = -19.9 \times 10^{-6}\ K^{-1}$, 298–763 K) [48] and other Fe-based Laves phase materials such as $Hf_{0.80}Nb_{0.20}Fe_2$ ($\alpha_v = -15\times10^{-6}\ K^{-1}$, 150–240 K) [27], and $Hf_{0.80}Ta_{0.20}Fe_2$ ($\alpha_v = -57.6\times10^{-6}\ K^{-1}$, 250–340 K) [20].

The Mössbauer spectra of arc-melted Ti0.15 and melt-spun Ti0.40 samples are shown in Fig. 6.7(a-f). The area ratio of the components corresponding to the Fe(6*h*) and Fe(2*a*) sites was set to 3:1 [40, 49]. Table 6.2 summarizes the fitted parameters for the Mössbauer spectra at different temperatures. The small linewidth (0.4 mm/s) for all sites (except for the relaxing phase) indicates a good quality of fit for the spectra. The similar isomer shift and quadrupole splitting for Fe at the 2*a* and 6*h* sites indicates that both sites have a similar electronic state [50]. For the arc-melted Ti0.15 sample, the spectrum exhibits a paramagnetic feature at 400 K, which is consistent with the neutron diffraction results. The spectra at 4.2, 120 and 300 K contain two magnetic sub-spectra, attributed to the Fe(6*h*) and Fe(2*a*) sites. The hyperfine fields for the Ti0.15 sample at 4 K are 19.6 T and 17.2 T at the 6*h* and 2*a* sites, respectively. Using a proportionality factor of 14.2 T/μ_B [51] yields magnetic moments for the Fe(6*h*) site and the Fe(2*a*) site of 1.4 μ_B and 1.2 μ_B, respectively. This is in reasonable agreement with the ND results (see Table 6.1). At 350 K, the spectrum consists of a

sextet magnetic sub-spectrum and a quadrupole doublet, which is considered to be the relaxing phase, with a coexistence of the ferromagnetic and the paramagnetic phase (45%) [52]. This coexistence of FM and PM phases is consistent with the ND data at 350 K.

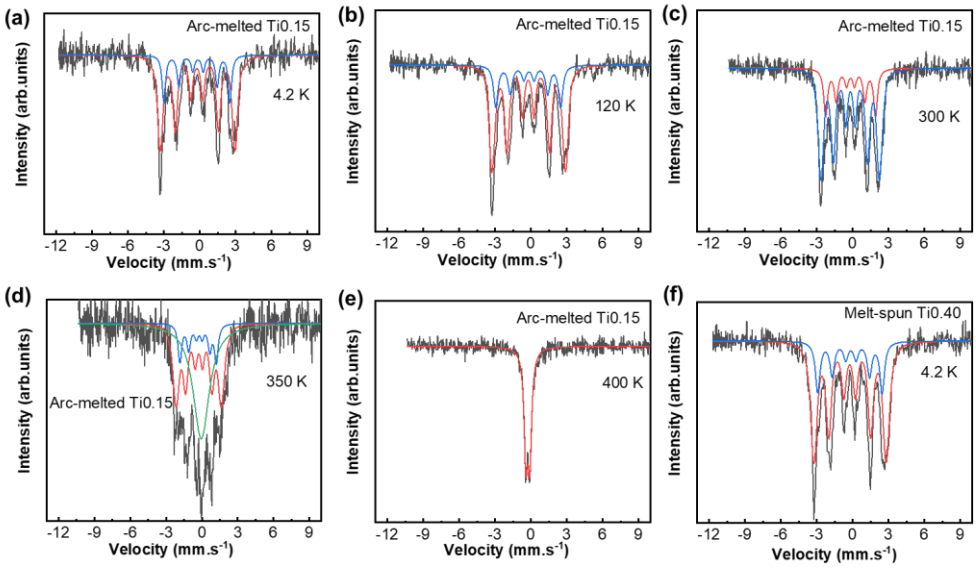

Fig. 6.7. Mössbauer spectra of the arc-melted Ti0.15 sample at (a) 4.2 K, (b) 120 K, (c) 300 K, (d) 350 K, (e) 400 K. (f) Mössbauer spectra of the melt-spun Ti0.40 sample at 4.2 K. The black line represents the experimental spectrum.

Table 6.2. Fitted Mössbauer parameters of the selected $(Hf,Ti)Fe_2$ samples, obtained at different temperatures. Experimental uncertainties: Isomer shift: I.S. ± 0.03 mm s^{-1}; Quadrupole splitting: Q.S. ± 0.03 mm s^{-1}; Line width: Γ ± 0.05 mm s^{-1}; Hyperfine field: ± 0.2 T; Spectral contribution: ± 3%. FM: ferromagnetic phase; PM: paramagnetic phase.

Sample	*T* (K)	*IS* (mm s^{-1})	*QS* (mm s^{-1})	*Hyperfine field* (T)	*Γ* (mm s^{-1})	*Phase*
Melt-spun Ti0.40	4.2 K	-0.23	0.03	18.9	0.46	FM (6*h*)
		-0.19	-0.08	16.7	0.46	FM (2*a*)
Arc-melted Ti0.15	4.2 K	-0.21	0.06	19.6	0.38	FM (6*h*)
		-0.19	-0.09	17.2	0.33	FM (2*a*)
	120 K	-0.20	0.04	19.1	0.36	FM (6*h*)
		-0.19	-0.07	16.9	0.43	FM (2*a*)
	300 K	-0.21	-0.01	15.3	0.41	FM (6*h*)
		-0.19	-0.04	13.1	0.43	FM (2*a*)
	350 K	-0.27	-0.01	12.0	0.43	FM (6*h*)
		-0.27	-0.09	9.5	0.38	FM (2*a*)
		-0.05	–	–	1.65	PM
	400 K	-0.26	0.34	–	0.37	PM

The temperature dependence of the hyperfine field at the 2*a* and 6*h* sites is shown in Fig. 6.8(a). It is clear that the compound exhibits a ferromagnetic-to-paramagnetic transition between 350 and 400 K, which is consistent with the neutron diffraction results in Fig. 6.8(b). The magnetic hyperfine fields of Fe atoms at the 2*a* and 6*h* sites decrease simultaneously with increasing temperature, which is different from $Fe_2Hf_{0.8}Ta_{0.2}$ [49] and $Fe_2Hf_{0.9}Nb_{0.1}$ [40]. For $Hf_{0.8}Ta_{0.2}Fe_2$, the hyperfine field of Fe at the 2*a* site decreases to zero at the critical temperature of the first-order FM-AFM transition and the hyperfine field of Fe at the 6*h* site decreases to zero at the Curie temperature. The wide NTE window for $(Hf,Ta)Fe_2$ is attributed to the asynchronous FM ordering of Fe moments at 6*h* and 2*a* sites revealed by electron spin resonance [20]. As in the case in $Fe_2(Hf,Ti)$, the simultaneous decrease of the hyperfine field of Fe at the 2*a* and 6*h* sites indicates a second-order transition. Fig. 6.8(c) and (d) show the interatomic distances of Fe atoms derived from ND. The interlayer spacing of Fe_{6h}-Fe_{6h}, Fe_{6h}-Fe_{2a} and Fe_{6h}-Hf/Ti_{4f} increases linearly with

increasing temperature, while a sharp decrease of 0.36% in the intralayer spacing of Fe_{6h}-Fe_{6h} is observed within the NTE temperature range. This phenomenon could originate from the fact that the shortest Fe_{6h}-Fe_{6h} distance controls the magnetic interactions in $Fe_2(Hf,Ti)$. A similar trend is also reported for the temperature dependence of magnetism in $Sc_{0.4}Ti_{0.6}Fe_2$ [21] and the pressure-dependent magnetism in $Mn_3Ga_{0.95}N_{0.94}$ [53].

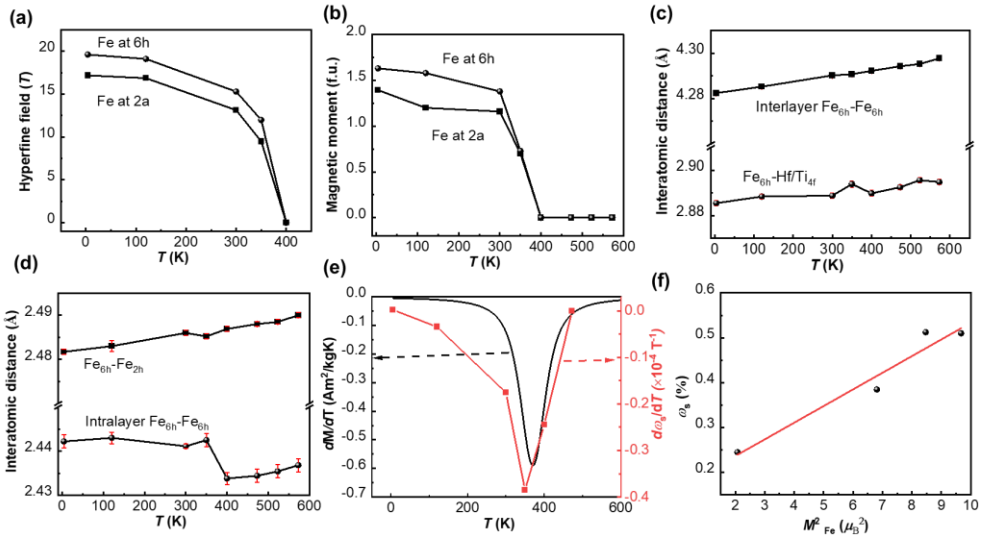

Fig. 6.8. (a) Temperature dependence of the hyperfine field of the arc-melted Ti0.15 sample, derived from Mössbauer spectroscopy. (b) Temperature dependence of magnetic moment at the 2*a* and 6*h* site of the arc-melted Ti0.15 sample derived from ND (Table 1). (c-d) Interatomic distance as a function of temperature. (e) $d\omega_s/dT$ and dM/dT (at a magnetic field of 1 T) as a function of temperature. (f) ω_s as a function of the square of the Fe magnetic moment.

To reveal the relation between negative thermal expansion and the magnetic order, the spontaneous volume magnetostriction is calculated by subtracting the thermal expansion of the nonmagnetic phase from the experimental one. The magnitude of the spontaneous volume magnetostriction can be defined as $\omega_s = \frac{V_{exp}-V_{nm}}{V_{nm}} \times 100\%$, where V_{exp} and V_{nm} (shown in Fig. 6.6(e)) are the unit-cell

volumes of experimental and the non-magnetic phases, respectively [21, 54]. Fig. 6.8(e) shows $d\omega_s/dT$ and dM/dT as a function of temperature. Both $d\omega_s/dT$ and dM/dT show the same trend, indicating a strong coupling between magnetism and lattice in this system. A sharp magnetic transition indicates a strong contribution of the spontaneous magnetostriction to the thermal contraction, which contributes to the occurrence of the NTE, as also reported in Mn_3Ge [55] and $Fe_2Zr_{0.7}Nb_{0.3}$ [56]. Based on the ND results, the shortest in-plane Fe_{6h}-Fe_{6h} distance controls the magnetic interactions of $Fe_2(Hf,Ti)$, so the rate at which the in-plane Fe magnetic moments decrease with increasing temperature governs the negative thermal expansion.

A linear correlation between the square of the Fe magnetic moment and ω_s is found in Fig. 6.8(f). The magnetic-lattice coupling can be quantitatively described by: $\omega_s(T) = kCM(T)^2$ [57], where k and C are the compressibility and the magneto-volume coupling constant, and M is the magnetic moment. The constant kC for the $Fe_2Hf_{0.85}Ti_{0.15}$ sample can be obtained from the slope of the curve in Fig. 6.8(f). For $Fe_2Hf_{0.85}Ti_{0.15}$, the constant kC at 4.2 K is calculated to be 1.48×10^{-10} cm^2/A^2. This value is of the same order of magnitude as those for $Fe_2Hf_{0.83}Ta_{0.17}$ (1.32×10^{-10} cm^2/A^2) [41] and $La(Fe_{0.86}Al_{0.24})_{13}$ (1.79×10^{-10} cm^2/A^2) [58], which are potential MCE materials with a strong magnetoelastic coupling. Short-range disorder, either caused by phase segregation in the $Fe_2(Hf,Ti)$ system ascribed to the large difference in Hf and Ti atoms sizes or due to rapid solidification, may account for the second-order phase transition in this magnetoelastic material.

6.4 Conclusions

In summary, we have studied the crystal structure, microstructure, and magnetic properties of arc-melted and melt-spun $Fe_2Hf_{1-x}Ti_x$ (x = 0.15, 0.27, 0.30, 0.33, 0.36, 0.40) alloys, which are derived from two isostructural $HfFe_2$ and $TiFe_2$ Laves phase materials. Surprisingly, a phase segregation is found in samples with x = 0.30–0.40, which we attribute to the 7.5% size difference between Hf and Ti. The high cooling rates achieved by melt spinning at a wheel speed of 30 m/s yield homogeneous alloys.

The magnetic transition temperature decreases linearly with the average unit-cell volume. The saturation magnetization suppressed by phase segregation can be recovered from 48.7 Am^2/kg to 59.6 Am^2/kg by melt spinning and thus the magnetocaloric effect can be enhanced from 0.46 to 0.54 J/kg K under a magnetic field change of 2 T due to the improved homogeneity. ND results reveal that the magnetic moments lie within the *a-b* plane and the reduction in magnetic moment of the Fe atoms with temperature is consistent with the abnormal decrease in the lattice parameter *a* with increasing temperature. We observed a negative thermal expansion ($-25\times10^{-6}\ K^{-1}$) for the single-phase $Fe_2Hf_{0.85}Ti_{0.15}$ compound over a wide temperature range of 300–400 K. The relation between the negative thermal expansion and the magnetism is discussed by quantitatively analysing the correlation between the spontaneous magnetostriction and magnetic moment of the Fe atoms. Our results provide a significant insight into the magnetoelastic coupling in these magnetocaloric materials and also provide an experimental route to solve common fabrication problems in Fe-based Laves phase materials.

References

[1] O. Tegus, E. Brück, K. H. J. Buschow & F. R. de Boer, Transition-metal-based magnetic refrigerants for room-temperature applications, Nature 415 (2002) 150-151.

[2] X. Moya, S. Kar-Narayan, N.D. Mathur, Caloric materials near ferroic phase transitions, Nat. Mater. 13 (2014) 439-50.

[3] E. Brück, Developments in magnetocaloric refrigeration, J. Phys. D: Appl. Phys. 38 (2005) R381-R391.

[4] K.G. Sandeman, Magnetocaloric materials: The search for new systems, Scr. Mater. 67 (2012) 566-571.

[5] N.H. Dung, Z.Q. Ou, L. Caron, L. Zhang, D.T.C. Thanh, G.A. de Wijs, R.A. de Groot, K.H.J. Buschow, E. Brück, Mixed magnetism for refrigeration and energy conversion, Adv. Energy Mater. 1 (2011) 1215-1219.

[6] F. Guillou, G. Porcari, H. Yibole, N. van Dijk, E. Bruck, Taming the first-order transition in giant magnetocaloric materials, Adv. Mater. 26 (2014) 2671-2675.

[7] F. Hu, B. Shen, J. Sun, Z. Cheng, G. Rao, X. Zhang, Influence of negative lattice expansion and metamagnetic transition on magnetic entropy change in the compound $LaFe_{11.4}Si_{1.6}$, Appl. Phys. Lett. 78 (2001) 3675-3677.

[8] J. Liu, J.D. Moore, K.P. Skokov, M. Krautz, K. Löwe, A. Barcza, M. Katter, O. Gutfleisch, Exploring $La(Fe,Si)_{13}$-based magnetic refrigerants towards application, Scr. Mater. 67 (2012) 584-589.

[9] J. Liu, T. Gottschall, K.P. Skokov, J.D. Moore, O. Gutfleisch, Giant magnetocaloric effect driven by structural transitions, Nat. Mater. 11 (2012) 620-626.

[10] T. Krenke, M. Acet, E.F. Wassermann, X. Moya, L. Mañosa, A. Planes, Martensitic transitions and the nature of ferromagnetism in the austenitic and martensitic states of Ni-Mn-Sn alloys, Phys. Rev. B 72 (2005) 014412.

[11] N.T. Trung, L. Zhang, L. Caron, K.H.J. Buschow, E. Brück, Giant magnetocaloric effects by tailoring the phase transitions, Appl. Phys. Lett. 96 (2010) 172504.

[12] L.V.B. Diop, J. Kastil, O. Isnard, Z. Arnold, J. Kamarad, Magnetic and magnetocaloric properties of itinerant-electron system $Hf_{1-x}Ta_xFe_2$ (x = 0.125 and 0.175), J. Alloys Compd. 627 (2015) 446-450.

[13] L.V.B. Diop, O. Isnard, M. Amara, F. Gay, J.P. Itié, Giant negative thermal expansion across the first-order magnetoelastic transition in $Hf_{0.86}Ta_{0.14}Fe_2$, J. Alloys Compd. 845 (2020) 156310.

[14] Z. Song, Z. Li, B. Yang, H. Yan, C. Esling, X. Zhao, L. Zuo, Large low-field reversible magnetocaloric effect in itinerant-electron $Hf_{1-x}Ta_xFe_2$ alloys, Materials 14 (2021) 1-11.

[15] L. Caron, X.F. Miao, J.C.P. Klaasse, S. Gama, E. Brück, Tuning the giant inverse magnetocaloric effect in $Mn_{2-x}Cr_xSb$ compounds, Appl. Phys. Lett. 103 (2013) 112404.

[16] Z. Zhang, Y. Zhang, X. Luo, S. Ma, H. Zeng, G. Yu, X. Zheng, C. Chen, Y. Hu, F. Xu, S.U. Rehman, Z. Zhong, Self-organized Bi-rich grain boundary precipitates for realizing steep magnetic-field-driven metamagnetic transition in Bi-doped Mn_2Sb, Acta Mater. 200 (2020) 835-847.

[17] Q. Shen, I. Batashev, F. Zhang, H. Ojiyed, N. van Dijk, E. Brück, The antiferromagnetic to ferrimagnetic phase transition in $Mn_2Sb_{1-x}Bi_x$ compounds, J. Alloys Compd. 866 (2021).

[18] R. Huang, Y. Liu, W. Fan, J. Tan, F. Xiao, L. Qian, L. Li, Giant negative thermal expansion in $NaZn_{13}$-type $La(Fe,Si,Co)_{13}$ compounds, J Am. Chem. Soc. 135 (2013) 11469-11472.

[19] Y.Y. Zhao, F.X. Hu, L.F. Bao, J. Wang, H. Wu, Q.Z. Huang, R.R. Wu, Y. Liu, F.R. Shen, H. Kuang, M. Zhang, W.L. Zuo, X.Q. Zheng, J.R. Sun, B.G. Shen, Giant negative thermal expansion in bonded MnCoGe-based compounds with Ni_2In-type hexagonal structure, J. Am. Chem. Soc. 137 (2015) 1746-1749.

[20] L.F. Li, P. Tong, Y.M. Zou, W. Tong, W.B. Jiang, Y. Jiang, X.K. Zhang, J.C. Lin, M. Wang, C. Yang, X.B. Zhu, W.H. Song, Y.P. Sun, Good comprehensive performance of Laves phase $Hf_{1-x}Ta_xFe_2$ as negative thermal expansion materials, Acta Mater. 161 (2018) 258-265.

[21] Y. Song, Q. Sun, M. Xu, J. Zhang, Y. Hao, Y. Qiao, S. Zhang, Q. Huang, X. Xing, J. Chen, Negative thermal expansion in $(Sc,Ti)Fe_2$ induced by an unconventional magnetovolume effect, Mater. Horiz. 7 (2020) 275-281.

[22] F. Hu, F. Shen, J. Hao, Y. Liu, J. Wang, J. Sun, B. Shen, Negative thermal expansion in the materials with giant magnetocaloric effect, Front Chem. 6 (2018) 438.

[23] Y. Song, N. Shi, S. Deng, X. Xing, J. Chen, Negative thermal expansion in magnetic materials, Prog. Mater. Sci. 121 (2021) 11835.

[24] B. Li, X.H. Luo, H. Wang, W.J. Ren, S. Yano, C.W. Wang, J.S. Gardner, K.D. Liss, P. Miao, S.H. Lee, T. Kamiyama, R.Q. Wu, Y. Kawakita, Z.D. Zhang, Colossal negative thermal expansion induced by magnetic phase competition on frustrated lattices in Laves phase compound (Hf,Ta)Fe_2, Phys. Rev. B 93 (2016) 224405.

[25] H.R. Rechenberg, L. Morellon, P.A. Algarabel, M.R. Ibarra, Magnetic moment at highly frustrated sites of antiferromagnetic Laves phase structures, Phys. Rev. B 71 (2005) 104412.

[26] Y. Qiao, Y. Song, K. Lin, X. Liu, A. Franz, Y. Ren, J. Deng, R. Huang, L. Li, J. Chen, X. Xing, Negative thermal expansion in (Hf,Ti)Fe_2 induced by the ferromagnetic and antiferromagnetic phase coexistence, Inorg. Chem. 58 (2019) 5380-5383.

[27] H. Yibole, A.K. Pathak, Y. Mudryk, F. Guillou, N. Zarkevich, S. Gupta, V. Balema, V.K. Pecharsky, Manipulating the stability of crystallographic and magnetic sub-lattices: A first-order magnetoelastic transformation in transition metal based Laves phase, Acta Mater. 154 (2018) 365-374.

[28] B.H. Toby, R factors in Rietveld analysis: How good is good enough?, Powder Diffr. 21 (2012) 67-70.

[29] Z. Klencsar, Mossbauer spectrum analysis by evolution algorithm, Nucl. Instr. Meth. Phys. Res. B 129 (1997) 527-533.

[30] L. van Eijck, L.D. Cussen, G.J. Sykora, E.M. Schooneveld, N.J. Rhodes, A.A. van Well, C. Pappas, Design and performance of a novel neutron powder diffractometer: PEARL at TU Delft, J. Appl. Crystallogr. 49 (2016) 1398-1401.

[31] H.M. Rietveld, Line profiles of neutron powder-diffraction peaks for structure refinement, Acta cryst. 22 (1967) 151-152.

[32] T.M. Sabine, Powder neutron diffraction-refinement of the total pattern, J. Appl. Cryst. 10 (1977) 277-280.

[33] J. Rodriguez-Carvajal, Recent advances in magnetic structure determination by neutron powder diffraction, Physica B 192 (1993) 55-69.

[34] G. Kresse, J. Hafner, Ab initio molecular dynamics for liquid metals, Phys. Rev. B Condens Matter 47 (1993) 558-561.

[35] G. Kresse, J. Furthmiiller, Efficiency of ab-initio total energy calculations for metals and semiconductors using a plane-wave basis set, Comput. Mater. Sci. 6 (1996) 15-50.

[36] J.P. Perdew, K. Burke, M. Ernzerhof, Generalized gradient approximation made simple, Phys. Rev. Lett. 77 (1996) 3865-3868.

[37] P.E. Blochl, Projector augmented-wave method, Phys. Rev. B: Condens Matter 50 (1994) 17953-17979.

[38] G. Kresse, D. Joubert, From ultrasoft pseudopotentials to the projector augmented-wave method, Phys. Rev. B 59 (1999) 1758-1775.

[39] M. Methfessel, A.T. Paxton, High-precision sampling for Brillouin-zone integration in metals, Phys. Rev. B: Condens Matter 40 (1989) 3616-3621.

[40] Y. Song, J. Chen, X. Liu, C. Wang, Q. Gao, Q. Li, L. Hu, J. Zhang, S. Zhang, X. Xing, Structure, magnetism, and tunable negative thermal expansion in $(Hf,Nb)Fe_2$ alloys, Chem. Mater. 29 (2017) 7078-7082.

[41] Y. Huang, Z. Han, Z. Jiang, S. Li, Y. Hsia, Microscopic magnetic properties of itinerant-electron system $Hf_{0.8}Ta_{0.2}(Fe_{1-x}Co_x)_2$ (x = 0-0.09): A Mössbauer study, Physica B: Condensed Matter 388 (2007) 354-358.

[42] M. Saoudia, J. Deportes, B. Ouladdiaf, Magnetic ground state of $Ti_{1-x}Sc_xFe_2$ system, J. Magn. Magn. Mater. 231 (2001) 265-272.

[43] J. Blasco, J. Stankiewicz, J. García, Phase segregation in the $Gd_{1-x}SrxFeO_{3-\delta}$ series, J. Solid State Chem. 179 (2006) 898-908.

[44] J. Yang, Y. Shao, Z. Feng, J. Liu, The effect of cooling rate on the phase formation and magnetocaloric properties in $La_{0.6}Ce_{0.4}Fe_{11.0}Si_{2.0}$ alloys, J. Magn. Magn. Mater. 452 (2018) 473-476.

[45] Q. Shen, F. Zhang, I. Dugulan, N. van Dijk, E. Brück, Magnetoelastic transition and negative thermal expansion of $Fe_2Hf_{0.83}Ta_{0.17}$ ribbons, Scr. Mater. 232 (2023).

[46] L. Sun, H. Yibole, O. Tegus, F. Guillou, $Sc_{0.28}Ti_{0.72}Fe_{2-x}T_x$ Alloys with T = Mn or Co, Crystals 10 (2020) 410.

[47] T.A. Mary, J.S.O. Evans, T.Vogt, A.W. Sleight, Negative thermal expansion from 0.3 to 1050 Kelvin in ZrW_2O_8, Science 272 (1996) 92-94.

[48] J. Chen, X. Xing, R. Yu, G. Liu, Thermal Expansion Properties of Lanthanum-Substituted Lead Titanate Ceramics, J. Am. Ceram. Soc. 88 (2005) 1356-1358.

[49] N.N. Delyagin, A.L. Erzinkyan, V.P. Parfenova, I.N. Rozantsev, G.K. Ryasny, Ferromagnetic-to-antiferromagnetic transition in $(Hf_{1-x}Ti_x)Fe_2$ intermetallic compounds induced by geometrical frustration of the Fe(2*a*) sites, J. Magn. Magn. Mater. 320 (2008) 1853-1857.

[50] Y.J. Huang, S.Z. Li, Z.D. Han, W.X. Wang, Z.Y. Jiang, S.L. Huang, J. Lin, Y.F. Hsia, Mössbauer study of the spin reorientation in pseudobinary alloy $Hf_{0.82}Ta_{0.18}Fe_2$, J. Alloys Compd. 427 (2007) 37-41.

[51] O. Eriksson, A. Svane, Isomer shifts and hyperfine fields in iron compounds, J. Phys.: Condens. Matter l (1989) 1589-1599.

[52] D. Huang, T. Ma, D.E. Brown, S.H. Lapidus, Y. Ren, J. Gao, Nanoscale phase separation and large refrigerant capacity in magnetocaloric material $LaFe_{11.5}Si_{1.5}$, Chem. Mater. 33 (2021) 2837-2846.

[53] K. Shi, Y. Sun, J. Yan, S. Deng, L. Wang, H. Wu, P. Hu, H. Lu, M.I. Malik, Q. Huang, C. Wang, Baromagnetic effect in antiperovskite $Mn_3Ga_{0.95}N_{0.94}$ by neutron powder diffraction analysis, Adv. Mater. 28 (2016) 3761-3767.

[54] Q. Li, K. Lin, Z. Liu, L. Hu, Y. Cao, J. Chen, X. Xing, Chemical diversity for tailoring negative thermal expansion, Chem. Rev. 122 (2022) 8438-8486.

[55] Y. Song, J. Chen, X. Liu, C. Wang, Q. Gao, Q. Li, L. Hu, J. Zhang, S. Zhang, X. Xing, Structure, Magnetism, and Tunable Negative Thermal Expansion in (Hf,Nb)Fe_2 Alloys, Chem. Mater. 29 (2017) 7078-7082.

[56] Y. Song, Y. Qiao, Q. Huang, C. Wang, X. Liu, Q. Li, J. Chen, X. Xing, Opposite Thermal Expansion in Isostructural Noncollinear Antiferromagnetic Compounds of Mn_3A (*A* = Ge and Sn), Chem. Mater. 30 (2018) 6236-6241.

[57] A. Fujita, K. Fukamichi, J.T. Wang, Y. Kawazoe, Large magnetovolume effects and band structure of itinerant-electron metamagnetic $La(Fe_xSi_{1-x})_{13}$ compounds, Phys. Rev. B 68 (2003).

[58] T.T. Palstra, G.J. Nieuwenhuys, J.A. Mydosh, K.H. Buschow, Mictomagnetic, ferromagnetic, and antiferromagnetic transitions in $La(Fe_xAl_{1-x})_{13}$ intermetallic compounds, Phys Rev B Condens Matter 31 (1985) 4622-4632.

Supplementary Material for Chapter 6

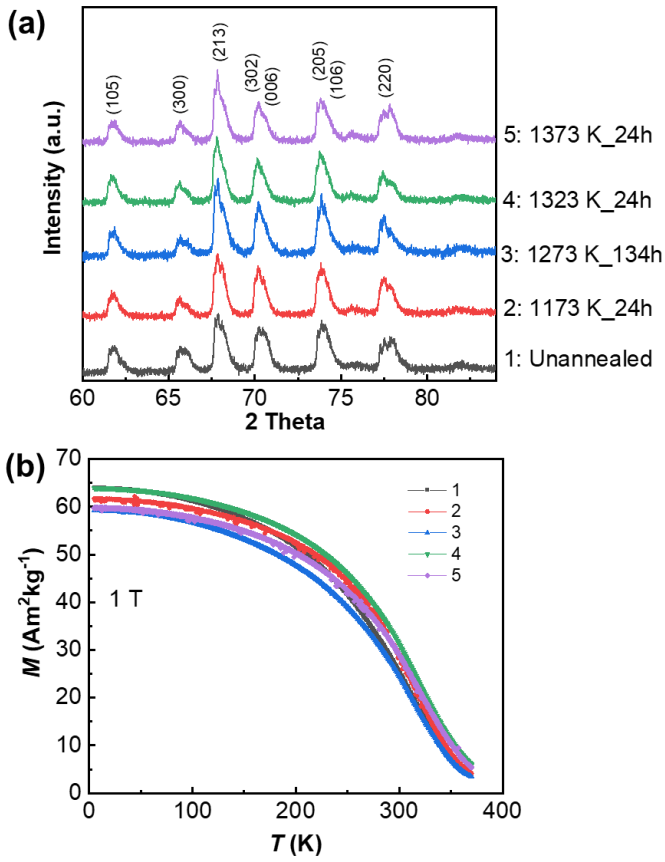

Fig. S6.1. (a) XRD patterns of the Ti0.36 compound with the indicated heat treatments. (b) *M*-*T* curves of the Ti0.36 compound with the heat treatments indicated in (a).

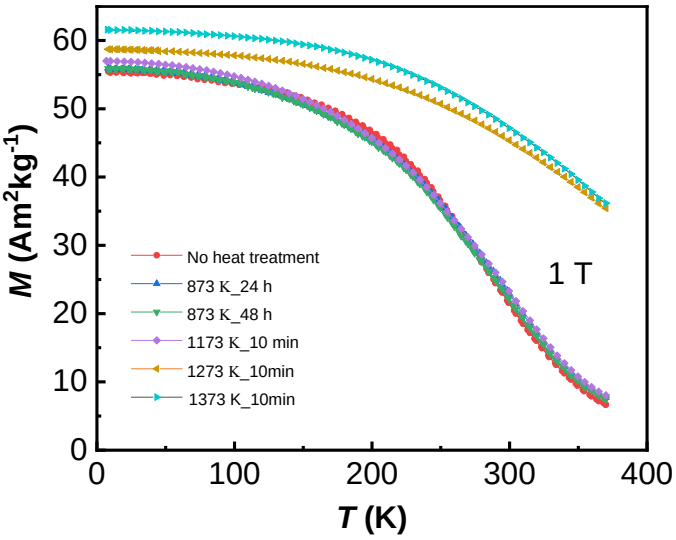

Fig. S6.2. *M-T* curves of the Ti0.40 compound with the indicated heat treatments.

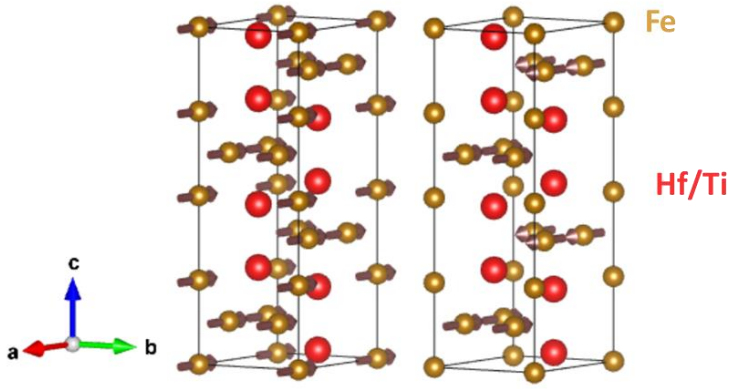

Fig. S6.3. (a) FM (left) and AFM (right) magnetic structures used for the DFT calculations.

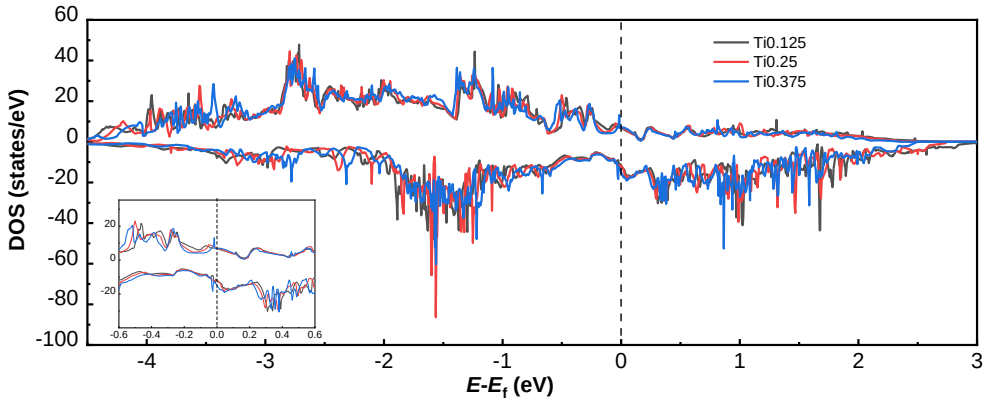

Fig. S6.4. (a) Calculated electron density of states (DOS) for $Fe_2Hf_{1-x}Ti_x$ (x = 0.125, 0.25, 0.375). The Fermi energies of $Fe_2Hf_{1-x}Ti_x$ (x = 0.125, 0.25, 0.375) are: 5.38, 5.32, 5.23 eV.

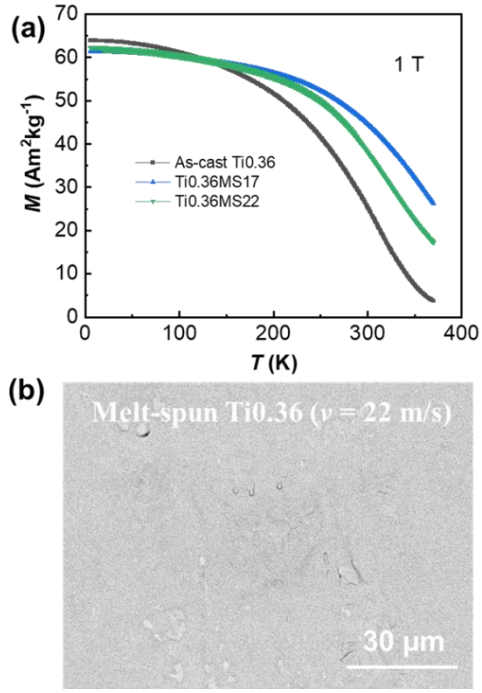

Fig. S6.5. (a) *M-T* curves of the arc-melted Ti0.36 sample and the melt-spun Ti0.36 samples produced at a wheel speed of 17 and 22 m/s. (b) Back-scattered SEM image of the melt-spun Ti0.36 sample with a wheel speed of 22 m/s.

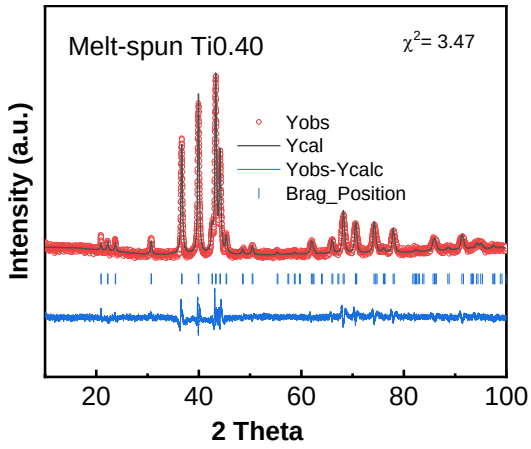

Fig. S6.6. (a) Rietveld refinement results for the melt-spun Ti0.40 sample.

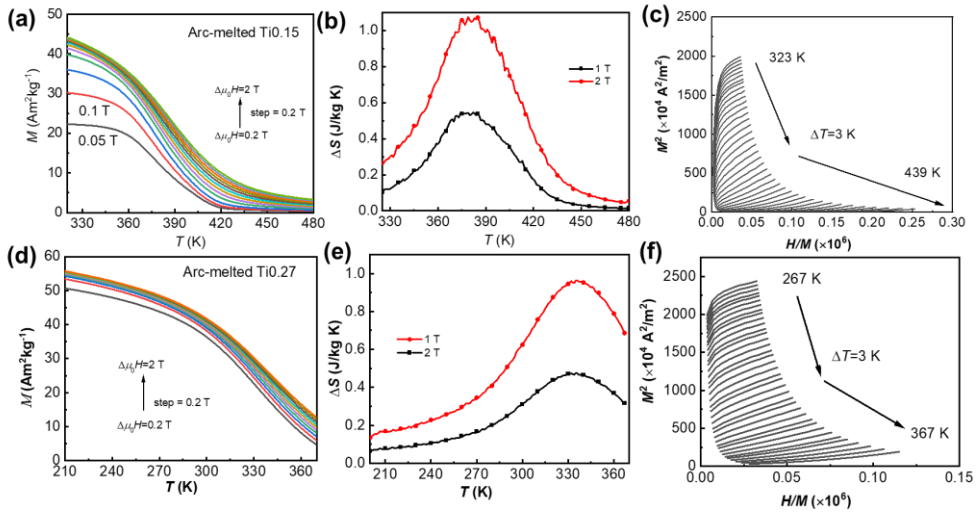

Fig. S6.7. (a, d) *M-T* curves of the arc-melted Ti0.15 and Ti0.27 samples. (b, e) Magnetic entropy change under a magnetic field change of 1 and 2 T. (c, f) Arrott plots from the magnetisaton data in (a) and (d).

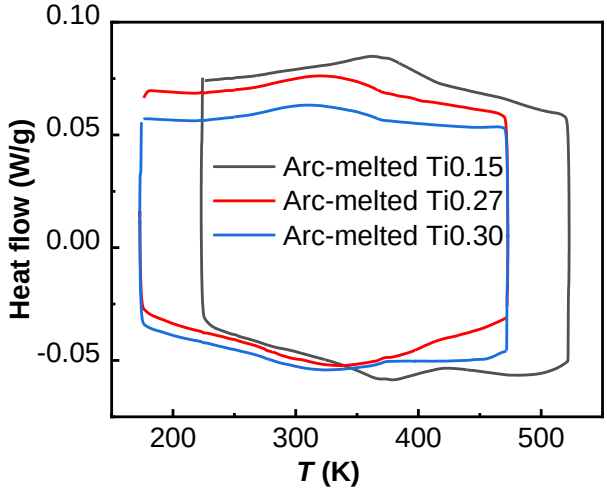

Fig. S6.8. DSC curves of selected arc-melted $Fe_2(Hf,Ti)$ samples.

Summary

Magnetic refrigeration is based on the magnetocaloric effect (MCE) and has attracted considerable attention due to its potentially higher energy efficiency, environmental friendliness and quietness compared to conventional vapour compression refrigeration. Boosting giant MCE materials with a magnetoelastic transition into commercial applications requires not only insights into the coupling between its magnetism and the lattice, but also the correlation between macroscopic performance and microstructure. In this thesis, the fundamental physical properties, including crystal structure, microstructure, magnetic structure, negative thermal expansion behaviour and the magnetocaloric effect, are studied in Mn_2Sb-based intermetallic compounds with an antiferromagnetic-to-ferrimagnetic transition and Fe_2Hf-based Laves phase compounds with a ferromagnetic-to-antiferromagnetic transition.

The influence of excess Mn on the microstructure, magnetoelastic transition and MCE of $(Mn,Cr)_2Sb$ compounds has been investigated in **Chapter 3**. The fraction of the (Mn,Cr)Sb secondary phase strongly reduces with increasing excess Mn, while the magnetoelastic transition temperature initially increases and then decreases with excess Mn. By Electron Probe Micro Analysis (EPMA) we find that with increasing excess Mn a higher Cr content is found in the (Mn,Cr)Sb secondary phase in comparison to the matrix. This competition for Cr leads to the nonlinear influence of excess Mn on the magnetic transition temperature. However, we observed that T_t scales linearly with the *c/a* lattice parameter ratio for a wide temperature range of 170–350 K. A large magnetic entropy change of 4.6 J/kg K is obtained for a magnetic field change of 2 T. A composition diagram for the *c/a* ratio is established to give guidance in the design of $(Mn,Cr)_2Sb$ alloys with a desired transition temperature for magnetocaloric applications.

For $(Mn,Cr)_2Sb$ alloys, the magnetoelastic transition results from an exchange inversion triggered by normal thermal contraction. The phase transition is shifted to higher temperatures when the lattice constant *c* is reduced by introducing smaller

atoms, which decreases the distance of adjacent Mn-II atoms. Interestingly, the magnetoelastic transition is also achieved by the bigger atom substitution of Bi for Sb in $Mn_2Sb_{1-x}Bi_x$. **Chapter 4** reveals the structure, the magnetoelastic transition and the MCE of $Mn_2Sb_{1-x}Bi_x$ (x = 0, 0.02, 0.04, 0.05, 0.07, 0.09, 0.15, 0.20). It is observed that Bi substitution for Sb causes an increase in the lattice parameters, a large magnetization jump identified as the AFM-FIM transition and an impressive magnetic field dependence of the transition temperature of $dT_t/d\mu_0H$ = -5.4 K/T. The transition temperature and magnetization jump both increase with increasing Bi concentration up to a value of x = 0.07, which is found to be the solubility limit of Bi. The exchange inversion in $Mn_2Sb_{1-x}Bi_x$ is caused by the substitution with a larger atom and ascribed to the enhanced coefficient of thermal expansion along the *c* axis, the stacking direction of the Mn-I and Mn-II layers.

The AFM-FIM magnetoelastic transition in Mn_2Sb-based alloys gives a sharp magnetization change, leading to an inverse MCE. In contrast, a conventional MCE is reported in itinerant-electron Fe_2Hf-based Laves-phase alloys exhibiting a FM-AFM magnetoelastic transition. The magnetism of 3*d* magnetic elements mainly depends on the intrinsic properties of various magnetic interactions, while extrinsic properties such as sample fabrication methods also play a role in the microstructure and thus further influence the magnetism. In **Chapter 5**, we have compared the magnetoelastic transition, the microstructure and the magnetocaloric effect in arc-melted and melt-spun $Fe_2Hf_{0.83}Ta_{0.17}$ compounds. A first-order magnetoelastic phase transition from the FM to the AFM phase is observed in the arc-melted alloy, while a second-order phase transition is observed in the melt-spun alloy. The same magnetic entropy change of about 1 J/kgK for a magnetic field change of 2 T is obtained for the arc-melted alloy at 247 K and for the melt-spun alloy at 287 K. A thermal hysteresis of 2 K and a phase coexistence in the temperature range from 217 to 257 K are found in the arc-melted alloy. In contrast, the melt-spun alloy undergoes a typical second-order phase transition accompanied by a negative thermal expansion effect with $\alpha_v = -19\times10^{-6}$ K^{-1} over a wide temperature range from 197 to 297 K.

Similar to $Fe_2(Hf,Ta)$, other Fe-based Laves phases such as $Fe_2(Hf,Nb)$, $Fe_2(Sc,Ti)$ and $Fe_2(Hf,Ti)$ also show a magnetoelastic transition accompanied by a negative thermal expansion effect. We employed Mössbauer spectroscopy, neutron powder diffraction and density functional theory (DFT) calculations in **Chapter 6** to study the correlation between the negative thermal expansion and magnetism in arc-melted and melt-spun $Fe_2Hf_{1-x}Ti_x$ (x = 0.15, 0.27, 0.30, 0.33, 0.36, 0.40) alloys, which are derived from two isostructural $HfFe_2$ and $TiFe_2$ Laves phase materials. Surprisingly, a phase segregation is found in samples with x = 0.30–0.40, which we attribute to the 7.5% size mismatch between Hf and Ti. The high cooling rates achieved by melt-spinning at a wheel speed of 30 m/s yield homogeneous alloys. The magnetic transition temperature decreases linearly with the average unit-cell volume. The saturation magnetization is reduced due to phase segregation, but it can be recovered by melt spinning from 48.7 Am^2/kg to 59.6 Am^2/kg and due to an improved homogeneity the magnetocaloric effect can be enhanced from 0.46 to 0.54 J/kg K under a magnetic field change of 2 T. We observed a negative thermal expansion ($-25\times10^{-6}\ K^{-1}$) for the single-phase $Fe_2Hf_{0.85}Ti_{0.15}$ alloy over a wide temperature range from 300 to 400 K. Neutron diffraction (ND) reveals that the magnetic moments lie within the *a*-*b* plane and that the reduction in magnetic moment of the Fe atoms with temperature is consistent with the abnormal decrease in the lattice parameter *a* with increasing temperature. The negative thermal expansion is therefore caused by the spontaneous magnetostriction, which exceeds the thermal expansion in the vicinity of the transition temperature. Our results do not only provide important insight into the magnetoelastic coupling in magnetocaloric systems from the point of view of fundamental physical properties, but also provide an experimental route to solve common fabrication problems in Fe-based Laves phase materials.

Samenvatting

Magnetisch koelen is gebaseerd op het magnetocalorische effect (MCE) en heeft een aanzienlijke aandacht gekregen vanwege de potentieel hogere energie efficiëntie, de goede milieuvriendelijkheid en de geluidarme toepassing in vergelijking met de conventionele gascompressie keeling. Het verbeteren van materialen met een enorm MCE en een magnetoelastische overgang voor commerciële toepassingen vereist niet alleen inzicht in de koppeling tussen het magnetisme en het rooster, maar ook inzicht in de correlatie tussen het macroscopische functioneren en de microstructuur. In dit proefschrift zijn de fundamentele fysische eigenschappen bestudeerd, waaronder de kristalstructuur, microstructuur, magnetische structuur, negatieve thermische uitzetting en het magnetocalorische effect, van Mn_2Sb gebaseerde intermetallische verbindingen met een antiferromagnetische-naar-ferrimagnetische (AFM-FIM) overgang en Fe_2Hf gebaseerde Laves fase verbindingen met een ferromagnetische-naar-antiferromagnetische (FM-AFM) overgang.

De invloed van een overdaad aan Mn op de microstructuur, de magnetoelastische overgang en het MCE in $(Mn,Cr)_2Sb$ verbindingen is onderzocht in **Hoofdstuk 3**. De fractie van de secundaire (Mn,Cr)Sb fase neemt sterk af voor een toename in de overdaad aan Mn, terwijl de magnetoelastische overgangstemperatuur aanvankelijk toeneemt en vervolgens weer afneemt voor een hogere overdaad aan Mn. Met behulp van elektrontest microanalyse (EPMA) vinden we dat met een toename in overdaad aan Mn een hogere Cr concentratie wordt gevonden in de secundaire (Mn,Cr)Sb fase in vergelijking tot de matrix fase. De competitie voor Cr leidt tot de niet-lineaire invloed van een overdaad aan Mn op de magnetische overgangstemperatuur. We zien echter dat T_t lineair schaalt met de c/a verhouding in roosterparameters binnen een breed temperatuurbereik van 170 tot 350 K. Een verandering in magnetische entropie van 4.6 J/kgK is gevonden voor een verandering in magnetisch veld van 2 T. Een diagram voor de c/a verhouding als functie van de samenstelling is geconstrueerd om richting te geven aan het ontwerp van $(Mn,Cr)_2Sb$

legeringen met een gewenste overgangstemperatuur voor magnetocalorische toepassingen.

Voor $(Mn,Cr)_2Sb$ legeringen volgt de magnetoelastische overgang uit een exchange inversie die getriggerd wordt door de reguliere thermische uitzetting. De faseovergang verschuift naar hogere temperaturen wanneer de roosterparameter *c* afneemt door de introductie van kleinere atomen, wat leidt tot een afname in de afstand tussen naburige Mn-II atomen. Het is interessant dat de magnetoelastische overgang ook bereikt wordt door de substitutie van een groter atoom, zoals Bi voor Sb, in $Mn_2Sb_{1-x}Bi_x$. **Hoofdstuk 4** beschrijft de structuur, de magnetoelastische overgang an het MCE van $Mn_2Sb_{1-x}Bi_x$ (x = 0, 0.02, 0.04, 0.05, 0.07, 0.09, 0.15, 0.20). Er is gevonden dat Bi substitutie van Sb een toename veroorzaakt in de roosterparameters, tot een grote sprong in de magnetisatie leidt die overeenkomt met de AFM-FIM overgang en een indrukwekkende magnetische veldafhankelijkheid van de overgangstemperatuur geeft van $dT_t/d\mu_0H$ = -5.4 K/T. De overgangstemperatuur en de sprong in de magnetisatie nemen beiden toe voor een toenemende Bi concentratie tot een waarde van x = 0.07, welke overeenkomt met de oploslimiet van Bi. De exchange inversie in $Mn_2Sb_{1-x}Bi_x$ wordt veroorzaakt door de substitutie met een groter atoom and kan worden toegeschreven aan de versterkte thermische uitzettingscoëfficiënt langs de *c* as, de richting waarin de Mn-I en Mn-II lagen gestapeld zijn.

De AFM-FIM magnetoelastische overgang in Mn_2Sb gebaseerde legeringen geeft aanleiding tot een scherpe verandering in de magnetisatie, welke tot een inverse MCE leidt. Echter, de Fe_2Hf gebaseerde Laves fase legeringen met itinerante elektronen vertonen een FM-AFM magnetoelastische overgang met een conventioneel MCE. Het magnetisme van magnetische 3*d* elementen hangt hoofdzakelijk af van de intrinsieke eigenschappen van verschillende magnetische interacties, terwijl extrinsieke eigenschappen zoals de samplepreparatie methodes ook een rol spelen in de microstructuur en dus het magnetische beïnvloeden. In **Hoofdstuk 5** hebben we de magnetoelastische overgang, de microstructuur en het

magnetocalorische effect vergeleken voor $Fe_2Hf_{0.83}Ta_{0.17}$ verbindingen die geproduceerd zijn middels boogsmelten en middels melt spinning. Een eerste-orde magnetoelastische faseovergang van de FM naar de AFM fase is waargenomen in de legering die geproduceerd is middels boogsmelten, terwijl een tweede-orde faseovergang is waargenomen in de legering die geproduceerd is middels melt spinning. Dezelfde magnetische entropieverandering van ongeveer 1 J/kgK is gevonden in een veldverandering van 2 T bij een temperatuur van 247 K voor de legering gemaakt middels boogsmelten en bij een temperatuur van 287 K voor de legering gemaakt middels melt spinning. Een thermische hysterese van 2 K en een fase co-existentie in het temperatuurgebied van 217 tot 257 K is gevonden voor de legering die gemaakt is middels boogsmelten. Echter, de legering die gemaakt is middels melt spinning ondergaat een typische tweede-orde faseovergang die samengaat met een negatief thermische uitzettingseffect met $\alpha_v = -19\times10^{-6}$ K^{-1} over een groot temperatuurbereik van 197 tot 297 K.

Vergelijkbaar met $Fe_2(Hf,Ta)$ vertonen andere Fe gebaseerde Laves fasen zoals $Fe_2(Hf,Nb)$, $Fe_2(Sc,Ti)$ en $Fe_2(Hf,Ti)$ ook een magnetoelastische overgang die samengaat met een negatief thermische uitzettingseffect. We hebben Mössbauer spectroscopie, neutronen poederdiffractie en density functional theory (DFT) berekeningen gebruikt in **Hoofdstuk 6** om de wisselwerking tussen de negatieve thermische uitzetting en het magnetisme te onderzoeken in $Fe_2Hf_{1-x}Ti_x$ (x = 0.15, 0.27, 0.30, 0.33, 0.36, 0.40) legeringen die geproduceerd zijn middels boogsmelten en middels melt spinning, welke zijn gevormd uit de twee iso-structurele verbindingen $HfFe_2$ and $TiFe_2$. Er is een verrassende faseschеiding gevonden in de samples met x = 0.30–0.40, welke is toegeschreven aan het 7.5% verschil in grootte tussen Hf en Ti. De hoge koelsnelheden die bereikbaar zijn met melt spinning bij een wielsnelheid van 30 m/s leiden tot homogene legeringen. De magnetische overgangstemperatuur neemt lineair af met het gemiddelde volume van de eenheidscel. De verzadigingsmagnetisatie neemt af als gevolg van de faseschеiding, maar het kan worden hersteld door melt spining, wat leidt tot een toename van 48.7 tot 59.6 Am^2/kg en middels een verbetering van de homogeniteit is het magnetocalorisch effect

verhoogd van 0.46 tot 0.54 J/kgK voor een verandering in magnetisch veld van 2 T. We vinden een negatieve thermische uitzetting ($-25\times10^{-6}\,K^{-1}$) voor een zuivere enkele-fase $Fe_2Hf_{0.85}Ti_{0.15}$ legering in een breed temperatuurgebied van 300 tot 400 K. Neutronendiffrcatie (ND) laat zien dat de magnetische momenten in het *a*-*b* vlak liggen en dat de afname in het magnetische moment van de Fe atomen met de temperatuur overeenkomt met de abnormale afname van roosterparameter *a* voor toenemende temperatuur. De negatieve thermische uitzetting wordt daarom veroorzaakt door de spontane magnetostrictie, welke in de buurt van de overgangstemperatuur groter is dan de thermische uitzetting. Onze resultaten geven niet alleen belangrijk inzicht in de magnetoelastische koppeling in magnetocalorische systemen vanuit het perspectief van fundamentele fysische eigenschappen, maar geven ook een experimentele route om veelvoorkomende problemen bij het productieproces op te lossen in Fe gebaseerde Laves fase materialen.

总结

相较于传统的气体压缩制冷，基于磁热效应的磁致冷因其更高的潜在能源效率，环境友好性和低噪音而受到研究者的广泛关注。为了加速具有磁弹相变的巨磁热材料进入商业市场的进程，我们需要深入研究磁性与晶格的耦合关系，同时探索宏观性质和微观表现之间的关联。在本论文中，我们选择了两种金属间化合物—Mn_2Sb 基合金和 Fe_2Hf 基 Laves 合金，随着温度升高它们分别表现出反铁磁-亚铁磁相变和铁磁-反铁磁相变的有序-有序的磁结构相变。本文系统研究了它们的晶体结构、微观结构、磁结构、负膨胀效应和磁热效应等基础物理性质。通过这些研究，希望为推动金属间化合物的磁致冷应用提供理论基础。

第三章重点研究了过量 Mn 对$(Mn,Cr)_2Sb$ 合金的微观结构，磁弹相变和磁热效应的影响。研究结果显示，随着过量 Mn 含量的增加，基体中的第二相 (Mn,Cr)Sb 含量明显减少，而磁弹相变温度则先增加后减小。通过电子扫描探针技术发现，随着过量 Mn 含量的增加，Cr 在第二相中的含量比在基体的更高，因此第二相对 Cr 的竞争导致过量 Mn 对磁相变温度产生非线性影响。分析发现在温度区间 170－350 K 内，磁性相变温度与 c/a 值呈线性关系。Cr2Mn8 在 2 T 磁场下的磁熵变为 4.6 J/kg K。考虑到磁致冷的实际应用温度范围，我们建立了 c/a 值与成分之间的相图。

在$(Mn,Cr)_2Sb$ 合金中，其磁弹相变源于正常的热收缩或者热膨胀引起的磁性交换翻转效应。小原子取代合金中的 Mn 或者 Sb 会导致晶格参数 c 减小，相邻的 Mn-II 原子间距减小，进而增强反铁磁作用，使得该磁弹相变的相变温度向高温移动。有趣的是，在 $Mn_2(Sb,Bi)$合金中，通过更大的原子 Bi 取代 Sb，同样能够诱发该相变。本文的第四章研究了 $Mn_2Sb_{1-x}Bi_x$ (x = 0, 0.02, 0.04, 0.05, 0.07, 0.09, 0.15, 0.20)的晶体结构，磁弹相变和磁热效应。实验结果表明，Bi 取代 Sb 原子会导致晶格参数的增大，以及反铁磁-亚铁磁相变过程中磁化率的显著变化。计算得到相变温度与磁场的依赖性参数为－5.4 K/T。相变温度和相变过程中的磁化率变化值随着 Bi 含量增加而增加，但在 x = 0.07

时达到上限，即 Bi 原子在 Mn_2Sb 合金中的固溶上限。该合金发生交换翻转效应是由于较大的原子 Bi 取代 Sb，导致 c 轴（Mn-I 和 Mn-II 的堆叠方向）方向的热膨胀系数增大，使得热膨胀足以诱发反铁磁-亚铁磁相变。

Mn_2Sb 基合金的反铁磁-亚铁磁相变带来了一个陡峭的磁化率变化，从而产生负磁热效应。相比之下，Fe_2Hf 基 Laves 合金，由于其巡游电子转变，呈现出铁磁-反铁磁相变，导致传统的正磁热效应。3d 磁性原子的磁性主要受不同磁性相互作用的本征性质影响。然而一些非本征性质，如样品制备方法，也会影响微观结构，从而对磁性产生影响。本文第五章对两种不同方法制备的 $Fe_2Hf_{0.83}Ta_{0.17}$ 合金，即电弧熔炼和甩带制备的样品进行了比较，研究了它们的磁弹相变，微观结构和磁热效应。电弧熔炼制备的合金表现出铁磁-反铁磁的一级相变特点，而甩带样品则展现出二级相变特点。在 2T 的磁场作用下，同样的磁熵变 1 J/kgK 在电弧样品（247 K）和甩带样品（287 K）中分别获得。电弧样品中观察到 2 K 的热滞后现象，并在 217 K－257 K 发现相共存。相反，甩带样品在 197 K-297 K 呈现典型的二级相变，伴随着负膨胀效应，其热膨胀系数为 $\alpha_v = -19\times10^{-6}\,K^{-1}$。

与 $Fe_2(Hf,Ta)$ 类似的其他的铁基 Laves 相，例如 $Fe_2(Hf,Nb)$、$Fe_2(Sc,Ti)$ 和 $Fe_2(Hf,Ti)$ 也展现出伴随负热膨胀效应的磁弹相变。在第六章中，通过两种等结构化的 Laves 合金 Fe_2Hf 和 Fe_2Ti 引入 $Fe_2Hf_{1-x}Ti_x$（x = 0.15, 0.27, 0.30, 0.33, 0.36, 0.40）合金，利用穆斯堡尔谱，中子粉末衍射和密度泛函理论（DFT）计算，研究了电弧熔炼和甩带制备的这些合金的负膨胀效应和磁性之间的关系。在电弧熔炼制备的合金中，当 x = 0.3－0.4 时，我们发现相分离现象，归因于 Hf 和 Ti 原子之间的 7.5%的尺寸差异。然而我们也发现甩带速率为 30 m/s 的高冷却速率有助于获得均匀的样品。在电弧熔炼制备的样品中，随着参杂的 Ti 含量增多，平均晶胞体积减小，磁性相变温度呈线性减小。相分离导致饱和磁化率减小（48.7 Am^2/kg），但该磁化率可以通过甩带恢复到 59.6 Am^2/kg，并且样品均匀性的提高使得甩带样品在 2T 磁场下的磁热效应从 0.46 提高到 0.54 J/kg K。电弧熔炼制备的单相合金 $Fe_2Hf_{0.85}Ti_{0.15}$ 在 300－400 K 温度范围内展现出负膨胀效应（$-25\times10^{-6}K^{-1}$）。中子粉末衍射揭示了

磁矩在 a-b 平面，并且随着温度的升高，Fe 原子的磁矩随温度减小与晶格参数 a 的异常减小规律一致。因此，该材料的负膨胀效应归因于—在相变温度区间内，自发的磁致伸缩效应超过了热膨胀效应。我们的研究结果不仅为磁热材料中的磁弹耦合现象提供了重要线索，而且提出了一种有望解决 Fe 基 Laves 相材料相分离问题的实验方案。

Acknowledgements

Time has truly flown by, and it is hard to believe that four years have already passed since I first arrived in the Netherlands at August 1st in 2019. Looking back, I feel fortunate to have experienced half year of a normal life before the onset of Covid-19. The subsequent year brought limited experiments and online courses, followed by another year of restricted meetings and gatherings. However, I am overjoyed that this year has brought us back to a sense of normalcy, where experiments can be easily scheduled, and we can reconnect with each other once more. Throughout my PhD journey, I have had the privilege of meeting and collaborating with countless remarkable individuals. As I take this moment to reflect on this significant period in my life, I want to extend my heartfelt gratitude to each and every one of you for your invaluable help and support.

I want to begin by expressing my deepest gratitude to **Ekkes Brück**, for your exceptional guidance and support as my daily supervisor during my PhD journey. From our very first online interview, your friendliness and easy-going nature left a lasting impression on me, and without a second thought, I accepted the offer to work with you on the same day. At the outset of my PhD, I must admit that I have a shortage of confidence when it came to academic discussion. However, the opportunity offered by you to be a teacher assistant for the master course 'Physics of energy materials,' which you and Stefan taught, gave me valuable insights into teaching and supervising from a new perspective. Additionally, participating in the Teaching 360° courses from graduate school further fueled my courage to seek more discussion meetings with you. Throughout my PhD, you have consistently been open and approachable, readily offering your guidance and support. Your invaluable suggestions and encouragement to explore new avenues have played a pivotal role in my growth as an independent researcher. Your optimistic outlook on challenges has had a profound impact on me, and I deeply admire your extensive knowledge and ability to explain complex concepts in an accessible manner. Not only are you a trailblazer in the field of magnetocaloric refrigeration, but you are also an exceptional

teacher. I am also grateful beyond words for your support in enabling me to attend various international conferences and summer schools. These experiences have been instrumental in building my professional network and enhancing my academic development. One particular memory I will forever cherish is when you came to my aid and assisted in repairing the arc-melting furnace and single-crystal furnace at the University of Amsterdam. Your willingness to lend a helping hand exemplifies your dedication and care for your students. I cannot thank you enough for the opportunities you have provided and the impact you have had on my personal and professional growth.

I am immensely grateful and want to extend my heartfelt thanks to my another daily supervisor, **Niels van Dijk**. Initially, I hesitated to seek your guidance due to my major in material science, but I am glad I eventually mustered the courage to approach you. Our extended discussions about the initial summary of my work have been incredibly beneficial. Your commitment to rigorous scientific principles and your logical way of thinking are truly admirable. You have a keen eye for pointing out the flaws in my work, which has significantly improved the quality of my research. I appreciate that you are always open to any research question I may have, and thanks to your approachability, I have gradually overcome my fear of asking seemingly "stupid" questions. Importantly, your encouragement and initial support when I faced challenges have profoundly influenced my attitude towards obstacles, benefiting not only my PhD journey but also shaping my approach to future challenges. I've also thoroughly enjoyed our casual conversations about science during cake time and Faculty activities. Your stories and introduction of fascinating scientific phenomena have sparked a deeper interest in science within me. Thank you, Niels, for being an exceptional promotor and for your support throughout my academic journey.

I would like to extend my sincere gratitude to the individuals with whom I closely collaborated during my research journey. Firstly, I am grateful to **Anne de Visser** for your generosity in allowing me to utilize the single-crystal furnace in your group. Your selfless help and support during my experiments in you lab is invaluable

for me. And I am deeply grateful for the invaluable feedbacks throughout my PhD thesis, which has contributed to the refinement of my thesis. **Yingkai Huang**, I want to express my sincere appreciation for your patience and guidance in teaching me how to use the single-crystal furnace. Your dedication to ensuring my understanding and proficiency to the furnace, even during challenging times of ill health, has been truly remarkable, and I am grateful for the knowledge and skills I gained under your guidance. **Iulian Dugulan**, I want to express my sincere appreciation for conducting the Mossbauer experiments for me and engaging in enlightening discussions. Your collaboration has significantly enriched my research and understanding of the subject matter, and I am grateful for the perspectives and ideas you brought to our work together. I must also acknowledge **Ivan Batashev**, my officemate. Your willingness to lend a helping hand in theoretical calculations and your generous sharing of PhD experiences have been instrumental in shaping the success of my research.

I also would like to express my sincere gratitude to the students I have supervised: **Floris, Calvin, Floor, Fenna, Huib**. Working with each of you to explore new MCE materials has been an absolute joy and a rewarding experience. Your dedication and hard work throughout the research progress and the remarkable progress you made upon graduation filled me with pride and excitement for your future endeavours. I am truly grateful for the opportunity to collaborate with you and I cherish the memories of our time together. Each of you has left a lasting impact on my approach to teaching and research, and I am confident that your future accomplishments will continue to inspire those around you.

I would like to express my deep gratitude to my wonderful colleagues, without whom my journey during my PhD would not have been as enriching and enjoyable. **Anton**, you have been an incredible support throughout my experiments. Your willingness to introduce me to other students in the building who needed assistance demonstrated your kind heart. Thank you for being considerate of my sensitive eyes and helping me block out the strong sunshine. **Robert**, our language practice sessions in Dutch were the highlight of my PhD days. Discussing culture and

life in my limited Dutch with you made the process of learning a new language enjoyable. Talking with you always put me at ease, and I am grateful for the customs you shared about the country we lived in. **Bert**, thank you for organizing those memorable activities, from Christmas night to football games and the Amsterdam reunion party. I still remember your warm words of encouragement when I faced criticism for the noise caused by the arc-melting device. **Kees**, your SEM training and selfless help during measurements were invaluable to me. I appreciate your support whenever I encountered problems or difficulties during SEM measurements. **Xiaohui**, thank you for your assistance with the XRD measurements in your building. **Xinmin**, I am grateful for your friendly gesture of taking me to a Dutch supermarket on my first day here. Your help and nice introduction to a new environment at the beginning of my PhD were greatly appreciated. And thank you for introducing me to the reading club. I enjoyed every discussion about all kinds of books we had together. **Bowei**, discovering that we came from the same city in China and even the same high school was a delightful surprise. Talking with you always made me feel at ease and connected. **Fengqi**, our discussions about the future and small talks meant a lot to me. Your perseverance and hard work are truly admirable. **Xuefei Miao**, thank you for your valuable assistance with XRD refinement. **Hamutu**, working together on our project and discussing both research and life with you was a pleasure. I enjoyed our fruitful interactions. **Anika**, your easy-going nature and shared interests made our interactions relaxing and enjoyable. Thank you for inviting me to your house for dinner; I still remember the delicious cakes you made! **Defang**, being your officemate for a year was a joy, and I cherished our shared travels and small talks. **Yueer**, I admire your warm and friendly personality, which delights me and everyone around you. **Ziying**, our time together at the 2023 NWO conference was delightful. **Yifan**, I am grateful for your invitation to the Christmas dinner and your impressive cooking skills. **Zhaolong**, I appreciate greatly your introduction to your lab at the beginning of my PhD. **Chaofan**, I enjoyed a lot our leisurely walk after dinner and I sincerely hope you are relishing your PhD life. **Ilse and Nicole**, thank you for the highly efficient administration support for my PhD life. I also want to extend my thanks to

Jan Leen Kloosterman, Anna Smith, Lars Bannenberg, Jouke Heringa, Ben Harrison, Michael Maschek, Kees Goubitz, Michael Steenvoorden, Stephan Eijt, Wim Bouwman, Henk Schut, Michel Thijs, Shengnan, Zhu Cheng, Xuehang, Runze, Hanggai, Diego, Justin, Zamran, Chao Ma, Bing Xu, Qi Jia, Justin, Rui Guo, Jiawei Lai, Yibole, and Marc van de Berg for the good moments and enjoyable interactions we shared. Thank you all for being a part of my journey and for making it a truly memorable and rewarding experience.

I would like to extend my heartfelt gratitude to several individuals who have played significant roles in my academic and personal growth. First and foremost, I want to express my deepest appreciation to my Master supervisor, **Jian Liu**. You have been the guiding light on my scientific journey, opening a window of knowledge and revealing to me the beauty of science. The platform you provided in the MCE group and your patient guidance have made significant impacts in shaping my academic path. I am forever grateful for the opportunities and support you provide for me during my Master's studies. To **Kun Wang** and **Jianping Guo**, I am delighted to have reunited with both of you in Europe since my Master's graduation. I extend my best wishes to you as you have embarked on new journeys in Germany and Denmark. May your endeavors be filled with success and fulfillment. Dear **Hans**, I also want to express my deepest gratitude for the incredible support and guidance you have provided as my Dutch coach. We started an online meeting on November 13, 2021 when COVID-19 posed challenges to our gatherings. The warm and welcoming atmosphere made by you and **Mathilde** has been a source of comfort and relaxation for me. The Dutch practice sessions when I spent at your house every Saturday evening have gradually been one of the most enjoyable and enriching experiences of my week. Reading books and engaging in conversations exclusively in Dutch have not only improved my language skills but also made me feel truly at home in this country. Your generosity and hospitality have left an indelible mark on my heart. (Beste Hans, ik wil je hartelijk bedanken voor de geweldige steun als mijn Nederlandse coach. We begonnen online te vergaderen op 13 november 2021. De warme en vriendelijke sfeer die door jij en Mathilde creëerden, bracht me veel troost

en ontspanning. De Nederlandse oefensessies die ik elke zaterdagavond bij jullie thuis doorbracht, werden een van de leukste en meest leerzame momenten van mijn week. Door in het Nederlands boeken te lezen en gesprekken te converseren, verbeterde niet alleen mijn taalvaardigheid, maar voel ik me ook echt thuis in dit land. Jullie vrijgevigheid en gastvrijheid hebben een blijvende indruk op mijn hart achtergelaten.)

I want to take a moment to express my gratitude to my friends for being a significant part of my life during my time in Delft and throughout my PhD journey. **Qi An**, meeting you again in Delft after high school and having you as my neighbor has been nothing short of amazing. Your friendship is a cherished gift, and I am grateful for the times we've spent together. **Lili Ma**, the days we visited museums during the challenging times of Covid hold a special place in my heart. Your company during those trips brought so much joy and meaning to my life. **Li Zou**, the weekends filled with cooking, badminton matches, and shopping are some of the fondest memories I hold. **Huanhuan**, I will always treasure the walk we had after dinner during the complete lockdown. Your optimistic and honest character inspires me a lot. **Dong Hu**, thank you for introducing me into your Dutch learning group and sharing your experience in Dutch learning. **Yujuan**, our dinners together, books reading and bouldering together have been delightful experiences that I cherish deeply. Your friendship has added so much joy to my spare life. **Zejia**, I truly appreciate our thoughts sharing about love. Your insights and perspectives have been thought-provoking and enriching. To **Koos**, I want to express my deep appreciation for the engaging discussions about life. Your diverse viewpoints on profound topics have made our conversations meaningful and enlightening. Our exchanges have broadened my understanding and enriched my perspective. To my badminton friends, **Guotai Li, Zhangyue Wei, Zou Li, Yunlong Guo, Li Wang, Fuqi Liang, Yimu Guo, and Tingkai Guo**, thank you for making the first two years of my PhD journey memorable. To my adventurous friends, **Zhaochong, Yujuan, Dongbin, Hong, Weichen, Ruitao Niu, Joan, Peiqing**, **Ziyu**, **Qinghe Gao, Sihao**, **Ting Wang and Pan Fang** the days we spent climbing real mountains in Belgium and exploring

bouldering and top rope have been incredible. A special thank goes to **Zhaochong, Dongbin and Hong** for opening the door of climbing for me. Your guidance, encouragement and expertise have played a role in helping me find happiness in this new hobby. To **Ying Lu, Zhuolin, Jiani Sun, Wenxuan Wang, Min Yang, Longjian, Yishui, Chenyang, Yinqi Wu, Zimu Wei, Jin Yan, Wangchao Yuan, Haozhou Li, Fei Sun, Qiaofeng Li, Yangming Fu and Cehao,** you are all good friends who have made a significant impact on my PhD life. The happy times we spent together will always hold a special place in my heart. To all the friends whose names may not be listed here, please know that your friendship and presence are cherished. I believe that memories of our time together will remain fresh and will be revisited in moments of nostalgia. Thank you all for your selfless sharing, positive attitudes, and unwavering support. You have influenced me in the most beautiful ways, and I am grateful to have you in my life.

Last but not least, I would like to thank **my parents**, **brother** and **Jian Yang**. To my dearest parents, As I look back on my life and reflect on the beautiful journey I have had, I cannot express enough gratitude for the love and support you have given me. You have given me the greatest gift of all − life and a precious opportunity to experience this world and all its wonders. I owe everything I am today to your unwavering love and care. As I grew older, I began to understand the immense sacrifices you made to raise me and my brother. Thank you for providing me with a happy and loving childhood, which has become the solid foundation upon which my adult life is built. (亲爱的父母：当我回顾我的博士生涯以及我的人生，语言无法让我充分表达我对你们给我的爱和支持的感激之情。是你们给予了我生命，才让我有机会去成长和体验这个世界，我今天所有的收获都离不开你们不渝的爱和关怀。当我逐渐成长，我才开始明白你们为了抚育我和弟弟所付出的巨大心血。感谢你们尽力为我提供的幸福童年，这是我一生成长快乐的基础。愿我有生之年好好报答你们的恩情！)

To my little brother Qian, having you as my companion and growing up together has been a source of joy and strength. The days we spent watching the sky and counting

stars on summer nights are memories I hold close to my heart. I believe in your potential and know that you will have a bright future. To my dear Jian Yang, your endless support and love during my PhD journey have meant the world to me. I cannot guarantee my PhD journey smooth without your support. I cannot forget your care and patience during my times of sickness and sadness. I feel incredibly lucky and happy to hold your hand now and forever. I have no doubt that our future together will be filled with colorful and joyful moments. To my parents, my brother, and Jian Yang, you are the pillars of my life, and I am eternally grateful for your love, care, and support. Your presence has brought immeasurable happiness and strength to my life, and I will carry your love with me in every step I take in the future.

Qi Shen

Delft, July 2023

List of publications

Publications related to the PhD study (*: corresponding author, #: equal contributors)

[1] **Q. Shen***, F. Zhang, I. Dugulan, N. van Dijk, E. Brück, Exploring the negative thermal expansion and magnetocaloric effect in Fe_2(Hf,Ti) Laves phase materials, Acta Materialia, 257 (2023) 119149.

[2] **Q. Shen***, F. Zhang, I. Dugulan, N. van Dijk, E. Brück, Magnetoelastic transition and negative thermal expansion of $Fe_2Hf_{0.83}Ta_{0.17}$ ribbons, Scripta Materialia, 232 (2023) 115482.

[3] **Q. Shen***, I. Batashev, H. Ojiyed, F. Zhang, N. van Dijk, E. Brück, Nonlinear influence of excess Mn on the magnetoelastic transition in $(Mn,Cr)_2Sb$, Journal of Alloys and Compounds, 903 (2022) 164011.

[4] **Q. Shen***, I. Batashev, F. Zhang, H. Ojiyed, N. van Dijk, E. Brück, The antiferromagnetic to ferrimagnetic phase transition in $Mn_2Sb_{1-x}Bi_x$ compounds, Journal of Alloys and Compounds, 866 (2021) 158963.

[5] F. Zhang*, I. Batashev, **Q. Shen**, Z. Wu, R.I. Smith, G.A. de Wijs, N. van Dijk, E. Brück, Impact of F and S doping on $(Mn,Fe)_2$(P,Si) giant magnetocaloric materials, Acta Materialia, 234 (2022) 118057.

[6] F. Zhang*, C. Taake, B. Huang, X. You, H. Ojiyed, **Q. Shen**, I. Dugulan, L. Caron, N. van Dijk, E. Brück, Magnetocaloric effect in the $(Mn,Fe)_2$(P,Si) system: From bulk to nano, Acta Materialia, 224 (2022) 117532.

[7] F. Zhang*, K. Westra, **Q. Shen**, I. Batashev, A. Kiecana, N. van Dijk, E. Brück, The second-order magnetic phase transition and magnetocaloric effect in all-d-metal NiCoMnTi-based Heusler alloys, Journal of Alloys and Compounds, 906 (2022) 164337.

[8] F. Zhang*, S. Smits, A. Kiecana, I. Batashev, **Q. Shen**, N. van Dijk, E. Brück, Impact of W doping on Fe-rich $(Mn,Fe)_2$(P,Si) based giant magnetocaloric materials, Journal of Alloys and Compounds, 933 (2023) 167802.

[9] Hamutu Ojiyed*****, Maarten Van Den Berg, Ivan Batashev, **Qi Shen**, Niels van Dijk, Ekkes Brück, Study of the room-temperature magnetocaloric properties of $Mn_5(Si,P)B_2$ compounds. Under review.

Publications related to the Master study

[1] **Q. Shen**, W. Sun, Z. Wei, J. Liu*****, Highly undercooled $Pd_{59.3}In_{23.2}Fe_{17.5}$ alloy: Shape memory effect, linear superelasticity and elastocaloric property, Scripta Materialia, 160 (2019) 58-61.

[2] **Q. Shen**, D. Zhao, W. Sun, Y. Li, J. Liu*, The effect of Tb on elastocaloric and mechanical properties of Ni-Mn-In-Tb alloys, Journal of Alloys and Compounds, 696 (2017) 538-542.

[3] **Q. Shen**, D. Zhao, W. Sun, Z. Wei, J. Liu*, Microstructure, martensitic transformation and elastocaloric effect in Pd-In-Fe polycrystalline shape memory alloys, Intermetallics, 100 (2018) 27-31.

[4] Y. Liu#, **Q. Shen**#, Z. Wei, W. Sun, F. Chen, J. Liu*, Enhanced barocaloric effect for Pd–In–Fe shape memory alloys with hydrostatic-pressure training, Journal of Applied Physics, 127 (2020).

[5] Z.Y. Wei, W. Sun, **Q. Shen**, Y. Shen, Y.F. Zhang, E.K. Liu*, J. Liu*, Elastocaloric effect of all-d-metal Heusler NiMnTi(Co) magnetic shape memory alloys by digital image correlation and infrared thermography, Applied Physics Letters, 114 (2019).

[6] Y. Shen, W. Sun, Z.Y. Wei, **Q. Shen**, Y.F. Zhang, J. Liu*, Orientation dependent elastocaloric effect in directionally solidified Ni-Mn-Sn alloys, Scripta Materialia, 163 (2019) 14-18.

Patents

Jian Liu, **Qi Shen**, Wen Sun, Zhiyang Wei, Mingxiao Zhang, Aru Yan. Patent No. 201811164007.1 granted (in Chinese).

Conference presentations:

1. Visual oral presentation: "The Antiferro to Ferrimagnetic Phase Transition in $Mn_2Sb_{1-x}Bi_x$ Compounds" in *the 65th Annual Conference on Magnetism and Magnetic Materials*, Nov. 2020.
2. Visual oral presentation: "The Antiferro to Ferrimagnetic Phase Transition in $Mn_2Sb_{1-x}Bi_x$ Compounds" in *the first Eurotherm seminar on Caloric Heating and Cooling*, Twente in the Netherlands, Jul. 2021.
3. Visual oral presentation: " Nonlinear influence of excess Mn on the magnetoelastic transition in $(Mn,Cr)_2Sb$" in the 15th Joint MMM-INTERMAG Conference, New Orleans in USA, Jan. 2022.
4. Oral presentation: "Nonlinear influence of excess Mn on the magnetoelastic transition in $(Mn,Cr)_2Sb$" in the 23rd international conference on solid compounds of transition elements, Bordeaux in France, June, 2022.
5. Poster: "Magnetocaloric effect in Fe-based Laves phase $(Hf,Ti)Fe_2$", Highly frustrated magnetism, Paris in France, June, 2022
6. Oral presentation: "Exploring the negative thermal expansion and magnetocaloric effect in Fe-based Laves phase $(Hf,Ti)Fe_2$", 4th IEEE international conference on Advances in magnetics, Moena in Italy, Jan, 2023.
7. Poster: "Enhanced magnetism upon melt spinning suppressing phase segregation in $Fe_2(Hf,Ti)$ Laves phase, Veldhoven in the Netherlands, April, 2023.

Curriculum Vitae

Qi Shen was born on July 24, 1994 in Jiujiang city, China. She enrolled in Wuhan University of Technology majoring in Materials and Science in 2012. In 2016 she received a bachelor's degree with the honour of Outstanding Graduate in Wuhan University of Technology.

With the exception from the admission examinations, she decided to pursue a master's degree majoring in Materials Physics and Chemistry under the supervision of Prof. Jian Liu, Ningbo Institute of Materials Technology and Engineering, Chinese Academy of Sciences. The master's project focused on the elastocaloric effect in magnetic Pd-In-Fe shape memory alloys. She received her master's degree in June 2019.
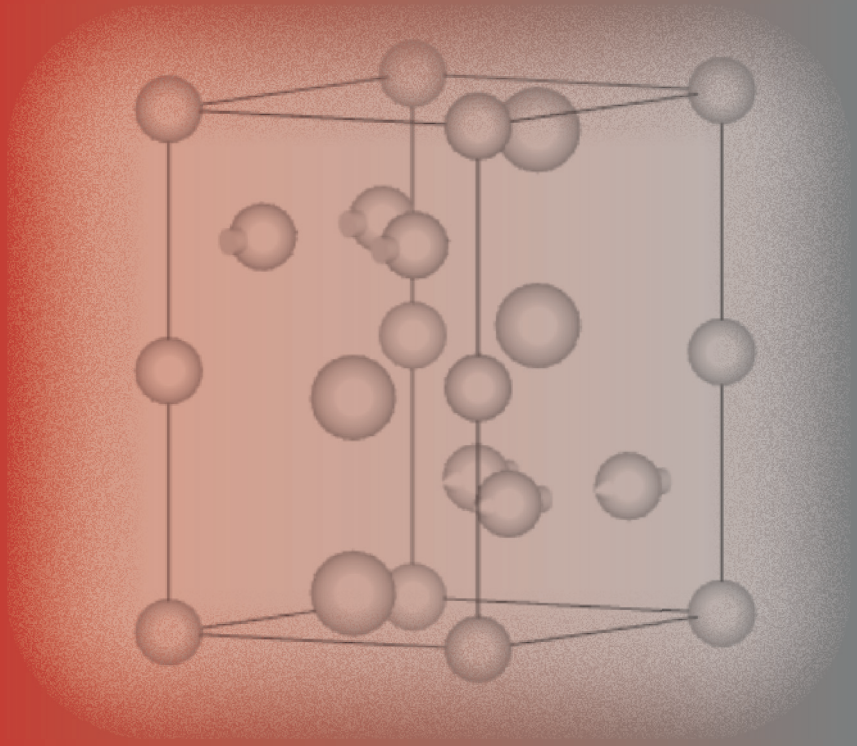
From August 2019, she continued her interest in energy materials and started her PhD under the supervision of Prof.dr. Ekkes Brück and Dr. Niels van Dijk in the group of Fundamental Aspects of Materials and Energy (FAME) at Delft University of Technology in the Netherlands. She used various experimental techniques such as Neutron diffraction, Mössbauer spectroscopy, Scanning electron microscopy to study magnetoelastic transitions in typical giant magnetoelastic materials. The results of this research are presented in this thesis entitled "Tuning Magnetoelastic Transitions in Mn_2Sb-based and Fe_2Hf-based Magnetocaloric Materials".